

Doctoral Thesis

Trajectory Tracking Control of an Omnidirectional
Mobile Robot

September, 2015

Doctoral Program in Integrated Science and Engineering
Graduate School of Science and Engineering
Ritsumeikan University

REN Chao

Doctoral Thesis reviewed
by Ritsumeikan University

Trajectory Tracking Control of an Omnidirectional
Mobile Robot

(全方位移動ロボットの軌道追従制御)

September, 2015

2015 年 9 月

Doctoral Program in Integrated Science and Engineering

Graduate School of Science and Engineering

Ritsumeikan University

立命館大学大学院理工学研究科

総合理工学専攻博士課程後期課程

REN Chao

レン チャオ

Supervisor: Professor MA Shugen

研究指導教員：馬 書根 教授

Abstract

Trajectory Tracking Control of an Omnidirectional Mobile Robot

by

REN Chao

Doctor of Philosophy in Department of Robotics

Ritsumeikan University, Biwako-Kusatsu Campus

Professor MA Shugen, Chair

In the past few decades, omnidirectional mobile robots (OMRs) have received growing attention in the field of wheeled mobile robots because of their high maneuverability. Compared with non-holonomic mobile robots, OMRs, which are holonomic, are able to achieve translational and rotational motions independently and simultaneously. As a result, they are quite useful in tight environments, such as hospitals and warehouses.

In this study, we focus on the trajectory tracking control of an omnidirectional mobile robot based on MY Wheel-II. The omnidirectional wheel mechanisms are divided into two groups: non-switch wheels and switch wheels, depending on whether the contact radius of the wheel to the robot geometric center switches. MY Wheel-II is one kind of switch wheels and the robot prototype is a discontinuous system.

Firstly, a dynamic model is established for our robot prototype, which shows that the robot is an autonomous switched nonlinear system. Since it is quite difficult to design control system for autonomous switched nonlinear systems based on switched system control theory, one current paradigm in literature is to design control systems based on continuous dynamic models of switched nonlinear systems. Therefore, we firstly derive two continuous dynamic models, i.e., average dynamic model and nonlinear parameter-varying dynamic model. Then resolved acceleration control (RAC), is employed to design controllers for our robot prototype based on the two continuous dynamic models, respectively. Simulations are conducted to verify and compare the two control systems.

However, it is shown in the experimental results that the control performances of average dynamic model based RAC are not satisfied. This is due to the modeling errors in the average dynamic model, including 1) unmodeled switching dynamics, 2) unmodeled forces, and 3) parameter uncertainties. Therefore, a trajectory tracking control system design is then proposed by employing a generalized proportional integral (GPI) observer to improve the control performances. The main idea is that the above modeling errors as well as the input-output cross coupling effects are considered as an unknown perturbation input vector. The perturbation input vector is then online estimated by the GPI observer, and compensated in the control signal. The closed-loop stability is analyzed. Finally, both simulations and experiments are conducted to verify and compare the effectiveness of the proposed control design against average dynamic model based RAC.

To further reduce the model information used in the previous GPI observer based control design, a passivity-based model free control (MFC) design is proposed, based on a modified GPI observer. The passivity property is analyzed for our robot prototype based on the average dynamic model. The control design objective is to design a controller such that the passivity property of the robot is preserved in the closed-loop system by using the modified GPI observer. The average contact radius is the only required model information. Moreover, the closed-loop stability is analyzed. Finally, experimental results and discussions are presented to compare the above three control designs.

Contents

Contents	i
List of Figures	iv
List of Tables	viii
Acknowledgements	ix
1 Introduction	1
1.1 Research Background	1
1.1.1 Omnidirectional Wheel Mechanisms	1
1.1.2 Applications	3
1.2 Literature Review	5
1.2.1 Control of OMRs	5
1.2.2 Control of Autonomous Switched Nonlinear System	7
1.2.3 Motivation	8
1.3 Outline of This Thesis	9
2 Kinematic and Dynamic Model of the Robot Prototype	11
2.1 Robot Prototype	12
2.1.1 MY Wheel-II Mechanism	12
2.1.2 Robot Prototype	13
2.1.3 Experimental Setup	13
2.2 Kinematic Model and Dynamic Model	16
2.2.1 Kinematic Model	16
2.2.2 Dynamic Model and Analysis	19

2.3	Summary	25
3	Resolved Acceleration Control (RAC)	27
3.1	Continuous Dynamic Modeling	28
3.1.1	Average Dynamic Model	29
3.1.2	Nonlinear Parameter Varying Dynamic Model	31
3.1.3	Simulation Verification	37
3.2	RAC Design and Verification	44
3.2.1	RAC Design	44
3.2.2	Simulation Verification	45
3.2.3	Experiments of Average Dynamic Model based RAC	53
3.3	Summary	56
4	Generalized Proportional Integral (GPI) Observer based Control	58
4.1	Control System Design	59
4.1.1	Controller Design	60
4.1.2	GPI Observer Design	62
4.1.3	Stability Analysis	64
4.2	Simulation and Experimental Verification	65
4.2.1	Simulations	65
4.2.2	Experiments	69
4.3	Summary	77
5	Passivity based Model Free Control (MFC)	78
5.1	Passivity Analysis	79
5.2	Passivity based MFC	81
5.2.1	Control System Design	81
5.2.2	Stability Analysis	86
5.3	Experiments and Discussions	87
5.3.1	Tracking Performance	87
5.3.2	Robustness	92
5.3.3	Discussions	98
5.4	Summary	99
6	Conclusion and Future Work	101

6.1	Conclusion	101
6.2	Future Work	103
A	Conditions on the Periodic Switching of Contact Radius	113
B	Control Board Design	115
C	Motor Driver Board Design	116
D	Original Experimental Data	117
D.1	Original Data of Average Dynamic Model based RAC	117
D.1.1	Tracking Performance	117
D.1.2	Robustness	119
D.2	Original Data of GPI Observer based Control	119
D.2.1	Tracking Performance	119
D.2.2	Robustness	119
D.3	Original Data of Passivity based MFC	119
D.3.1	Tracking Performance	119
D.3.2	Robustness	119
E	Reference List	120
	Publications	121

List of Figures

1.1	Non-switch wheel mechanisms. (a) Universal wheel [1]. (b) Mecanum wheel [2]. (c) Alternate wheel [3, 4]. (d) Ball wheel [5].	2
1.2	Switch wheel mechanisms. (a) Longitudinal orthogonal-wheel [6]. (b) MY wheel [7]. (c) MY wheel-II [8]. (d) Swedish wheel [9].	3
1.3	(a) KMP omniMove [10]. (b) KMR QUANTEC [11].	4
1.4	Omnidirectional wheelchairs: (a) OMR developed in University at Hagen [12]. (b) OMR developed in Chiba Institute of Technology [13].	5
1.5	Robot prototype [8]: (a) MY wheel-II assembly. (b) A robot prototype with three MY Wheel-II assemblies.	8
2.1	MY wheel-II mechanism: (a) Motion principle. (b) End-view.	12
2.2	(a) MY Wheel-II assembly. (b) Prototype platform.	14
2.3	Schematic of the experimental setup.	15
2.4	Coordinate frames of the omnidirectional mobile robot.	17
2.5	Force analysis.	20
3.1	The real contact radius (solid black line), average contact radius (dotted red line) and spline contact radius (dashed green line).	29
3.2	Switching condition (i): (a) Top view. (b) End view.	32
3.3	Switching condition (ii): (a) Top view. (b) End view.	32
3.4	Example of adaptive spline curve.	34
3.5	Open-loop simulation results: (a) Real contact radius L_i , average contact radius L_a and spline contact radius L_i^{sp} . (b) Variable ϕ_{10} (see (3.4)). (c) Variable ϕ_{20} (see (3.4)). (d) Variable ϕ_{30} (see (3.4)).	38
3.6	Open-loop simulation results: (a) Robot trajectory in the xy-plane. (b) Robot position in x component. (c) Robot position in y component. (d) Robot orientation θ	39

3.7	Open-loop simulation results: (a) Robot velocity in x component. (b) Robot velocity in y component. (c) Robot rotational velocity $\dot{\theta}$	40
3.8	Simulation results of average dynamic model based RAC and NLPV dynamic model based RAC (circle trajectory): (a) Reference trajectory and responses in the xy-plane. (b) Reference trajectory and responses in the orientation direction. (c) Tracking errors. (d) Control input $\mathbf{u}(t)$	47
3.9	Simulation results of average dynamic model based RAC and NLPV dynamic model based RAC (circle trajectory): (a) Reference velocity and responses. (b) Contact radius of NLPV dynamic model based RAC and the adaptive approaching curves.	48
3.10	Simulation results of average dynamic model based RAC and NLPV dynamic model based RAC (square trajectory): (a) Reference trajectory and responses in the xy-plane. (b) Reference trajectory and responses in the orientation direction. (c) Tracking errors. (d) Control input $\mathbf{u}(t)$	50
3.11	Simulation results of average dynamic model based RAC and NLPV dynamic model based RAC (lemniscate trajectory): (a) Reference trajectory and responses in the xy-plane. (b) Reference trajectory and responses in the orientation direction. (c) Tracking errors. (d) Control input $\mathbf{u}(t)$	51
3.12	Simulation and experimental results of average dynamic model based RAC (circle trajectory): (a) Reference trajectory and responses in the xy-plane. (b) Reference trajectory and responses in the orientation direction. (c) Tracking errors. (d) Control input $\mathbf{u}(t)$	52
3.13	Simulation and experimental results of average dynamic model based RAC (circle trajectory): (a) Robot velocity. (b) Measured contact radius in the experiments and the average contact radius L_a in the average dynamic model.	53
3.14	Simulation and experimental results of average dynamic model based RAC (square trajectory): (a) Reference trajectory and responses in the xy-plane. (b) Reference trajectory and responses in the orientation direction. (c) Tracking errors. (d) Control input $\mathbf{u}(t)$	54
3.15	Simulation and experimental results of average dynamic model based RAC (lemniscate trajectory): (a) Reference trajectory and responses in the xy-plane. (b) Reference trajectory and responses in the orientation direction. (c) Tracking errors. (d) Control input $\mathbf{u}(t)$	55
4.1	Block diagram of GPI observer based control system for the mobile robot.	59
4.2	Simulation results of average dynamic model based RAC and GPI observer based control (circle trajectory): (a) Circle trajectory in the xy-plane: reference trajectory and responses. (b) Circle trajectory in the orientation direction: reference trajectory and responses. (c) Tracking errors. (d) Control input $\mathbf{u}(t)$	66
4.3	Simulation results of GPI observer based control (circle trajectory): (a) Real perturbation input vector \mathbf{f} and its estimation by the GPI observer $\hat{\mathbf{f}}(t)$. (b) Real robot velocity and its estimation by the GPI observer.	68

4.4	Simulation results of average dynamic model based RAC and GPI observer based control (circle trajectory): (a) Contact radius of average model based RAC (L_i , $i=1,2,3$). (b) Contact radius of the GPI observer based control (L_i , $i=1,2,3$).	70
4.5	Simulation results of average dynamic model based RAC and GPI observer based control (square trajectory): (a) Robot trajectory in the xy-plane: reference trajectory and responses. (b) Robot trajectory in the orientation direction: reference trajectory and responses. (c) Tracking errors. (d) Control input $\mathbf{u}(t)$	71
4.6	Simulation results of average dynamic model based RAC and GPI observer based control (lemniscate trajectory): (a) Robot trajectory in the xy-plane: reference trajectory and responses. (b) Robot trajectory in the orientation direction: reference trajectory and responses. (c) Tracking errors. (d) Control input $\mathbf{u}(t)$	72
4.7	Experimental results of average dynamic model based RAC and GPI observer based control (circle trajectory): (a) Circle trajectory in the xy-plane: reference trajectory and responses. (b) Circle trajectory in the orientation direction: reference trajectory and responses. (c) Tracking errors. (d) Control input $\mathbf{u}(t)$	73
4.8	Experimental results of GPI observer based control (circle trajectory): (a) Estimation of perturbation input vector by the GPI observer $\hat{\mathbf{f}}(t)$. (b) Measured robot velocity and its estimation by the GPI observer.	74
4.9	Experimental results of average dynamic model based RAC and GPI observer based control (square trajectory): (a) Robot trajectory in the xy-plane: reference trajectory and responses. (b) Robot trajectory in the orientation direction: reference trajectory and responses. (c) Tracking errors. (d) Control input $\mathbf{u}(t)$	75
4.10	Experimental results of average dynamic model based RAC and GPI observer based control (lemniscate trajectory): (a) Robot trajectory in the xy-plane: reference trajectory and responses. (b) Robot trajectory in the orientation direction: reference trajectory and responses. (c) Tracking errors. (d) Control input $\mathbf{u}(t)$	76
5.1	Block diagram of passivity based MFC for the mobile robot.	81
5.2	Experimental results of average dynamic model based RAC, GPI observer based control and passivity based MFC (circle trajectory): (a) Circle trajectory in the xy-plane: reference trajectory and responses. (b) Circle trajectory in the orientation direction: reference trajectory and responses. (c) Tracking errors. (d) Control input $\mathbf{u}(t)$	88
5.3	Experimental results of passivity based MFC (circle trajectory): (a) Estimation of perturbation input vector by the GPI observer $\hat{\mathbf{w}}$. (b) Measured robot velocity and its estimation by the modified GPI observer.	89

5.4	Experimental results of average dynamic model based RAC, GPI observer based control and passivity based MFC (square trajectory): (a) Square trajectory in the xy-plane: reference trajectory and responses. (b) Square trajectory in the orientation direction: reference trajectory and responses. (c) Tracking errors. (d) Control input $\mathbf{u}(t)$	90
5.5	Experimental results of average dynamic model based RAC, GPI observer based control and passivity based MFC (lemniscate trajectory): (a) Lemniscate trajectory in the xy-plane: reference trajectory and responses. (b) Lemniscate trajectory in the orientation direction: reference trajectory and responses. (c) Tracking errors. (d) Control input $\mathbf{u}(t)$	91
5.6	Simulation results of robustness of average dynamic model based RAC: (a) Tracking errors with and without disturbance, respectively. (b) Control input $\mathbf{u}(t)$ with and without disturbance, respectively.	94
5.7	Simulation results of robustness of GPI observer based control: (a) Tracking errors with and without disturbance, respectively. (b) Control input $\mathbf{u}(t)$ with and without disturbance, respectively.	94
5.8	Simulation results of robustness of passivity based MFC: (a) Tracking errors with and without disturbance, respectively. (b) Control input $\mathbf{u}(t)$ with and without disturbance, respectively.	95
5.9	Experimental setup of the robust tests.	96
5.10	Experimental results of robustness of average dynamic model based RAC: (a) Tracking errors with and without disturbance, respectively. (b) Control input $\mathbf{u}(t)$ with and without disturbance, respectively.	96
5.11	Experimental results of robustness of GPI observer based control: (a) Tracking errors with and without disturbance, respectively. (b) Control input $\mathbf{u}(t)$ with and without disturbance, respectively.	97
5.12	Experimental results of robustness of passivity based MFC: (a) Tracking errors with and without disturbance, respectively. (b) Control input $\mathbf{u}(t)$ with and without disturbance, respectively.	97
B.1	Central control board developed in our lab.	115
C.1	Motor driver board developed in our lab.	116

List of Tables

2.1	Specifications of the prototype platform	14
2.2	Nomenclature	21
2.3	Contact modes of the three-wheeled mobile robot	23
3.1	Simulation results with different γ	43
3.2	IAE of average dynamic model based and NLPV dynamic model based RAC	49
3.3	IAE of average dynamic model based RAC	53
4.1	Simulation results: IAE of average dynamic model based RAC and GPI observer based control	67
4.2	Experimental results: IAE of average dynamic model based RAC and GPI observer based control	70
5.1	Experimental results: IAE of average dynamic model based RAC, GPI ob- server based control, and passivity based MFC	87
5.2	Simulation results: comparisons of robustness of the three control methods.	93
5.3	Experimental results: comparisons of robustness of the three control methods.	95
D.1	Tracking performances: IAE of average dynamic model based RAC	117
D.2	Robustness: IAE of average dynamic model based RAC	118
D.3	Tracking performances: IAE of GPI observer based control	118
D.4	Robustness: IAE of GPI observer based control	118
D.5	Tracking performances: IAE of passivity based MFC	119
D.6	Robustness: IAE of passivity based MFC	119

Acknowledgements

I would like to express my sincere most appreciation and thanks to Prof. Shugen Ma, my research supervisor, a professor in Department of Robotics at Ritsumeikan University, for his patient guidance, enthusiastic encouragement, continuous support and useful critiques of this research work. He was available for guidance at all times.

It is my pleasure to thank Prof. Kawamura Sadao and Prof. Hirai Shinichi for their valuable comments about this thesis. In addition, I would like to thank Prof. Hirokazu Maeda, Prof. Makoto Nokata and Prof. Ryuta Ozawa for their valuable suggestions and comments on my academic presentations in research seminars.

I also would like to thank Prof. Marco A. Arteaga Pérez and Dr. Alejandro Gutiérrez-Giles in Department of Control and Robotics, National Autonomous University of Mexico, for their kindly help and very valuable suggestions.

I am grateful to all my colleagues in Ma laboratory, especially, to Dr. Yi Sun, who gave me great help and encouragement during my whole doctoral course, to Mr. Lin Lin, who teach me to learn about the control board design and fabrication in our lab, to Mr. Chuanguo Li, who gave me kindly encouragement and useful suggestions at the beginning of my doctoral course and helped me a lot in the lab life, to Mr. Atsushi Kakogawa, who helped me a lot in the lab and tried his best to find the company for my internship, to Mr. Dingxin Ge and Mrs. Yongchen Tang, who helped me a lot in daily life and gave me many useful suggestions, to Yang Yang for his assistance in redesigning the prototype robot and many useful discussions, to Mr. Takahiro Matsuno and Mr. Xuan Zhou, who helped me to prepare the experiments, to Mr. Yang Tian for his great suggestions and useful help in developing the motor control and driver board, to Mr. Wenbin Tang for his help in the mathematics, to Mr. Huang Yan for his useful suggestions at the beginning of my doctoral course. It is studying with them that makes a colorful and fruitful campus life.

My grateful thanks are also extended to staffs at the workshop of Ritsumeikan University for their kindly help in fabricating the robot prototype in this thesis.

Finally, I wish to thank my parents for their support and encouragement throughout my study.

Curriculum Vitæ

REN Chao

Education

1993-1998	Elementary School of Haoshan (Shiqiao Town, Yiyuan City, Shandong Province, China) Elementary School Student
1998-2002	Junior High School of Shiqiao (Shiqiao Town, Yiyuan City, Shandong Province, China) Secondary School Student
2002-2005	NO.1 Middle School of Yiyuan (Yiyuan City, Shandong Province, China) Upper Secondary School Student
2005-2009	Shandong Jianzhu University (Jinan, Shandong Province, China) Bachelor Degree of Electrical Engineering and Automation
2009-2011	Harbin Institute of Technology (Harbin, Heilongjiang Province, China) Master Degree of Control Science and Engineering
2011-2015	Ritsumeikan University, BKC (Kusatsu, Shiga, Japan) Doctoral Candidate, Robotics

Personal

Born	May 1, 1986, Shandong, China.
Research Interests	Robust Control, Motion Control, Robot Control.

Chapter 1

Introduction

1.1 Research Background

High mobility of wheeled mobile robots is essential to enlarge their applications. However, the conventional wheeled mobile robots have nonholonomic constraints, which reduce their mobility and make the control and motion planning difficult. Omnidirectional Mobile Robots (OMRs), which are holonomic, provide such high mobility that conventional wheeled mobile robots cannot achieve. OMRs have the ability to move simultaneously and independently in both translational and rotational motion. Therefore, they are especially useful in environments congested with static and dynamic obstacles and narrow aisles, such as hospitals, warehouses, residential homes, and sheltered workshops for disabled people. In addition, OMRs are also frequently used as mobile bases for mobile robot manipulators due to their high mobility.

1.1.1 Omnidirectional Wheel Mechanisms

In literature, a variety of omnidirectional wheel mechanisms have been proposed over the past few decades. Several mechanisms have been designed based on the “universal wheel” concept, which is an assembly providing a combination of constrained and unconstrained motion when turning the wheel shaft [1]. The initial universal wheel design was used to

achieve omnidirectional motions without changing the direction of the wheels, but one problem of this wheel type is that it suffers from successive shocks when the individual rollers make contact with ground. Mecanum wheel [2] and Alternate wheel [3, 4], were then proposed to remedy the gap between the rollers and to provide a more smoother motion on hard surfaces.

Some mechanisms were designed based on the “orthogonal-wheels” concept, to reduce the successive shocks and to provide a smooth motion on hard surfaces. Pin and Killough [6] presented the “orthogonal-wheels” concept and proposed two major wheel assemblies: Longitudinal orthogonal-wheel assembly and Lateral orthogonal-wheel assembly. In our previous works, we proposed two novel omnidirectional wheel mechanisms, referred to as MY wheel [7] and MY wheel-II [8], which are based on sliced ball structure and can be considered as a natural extension of Longitudinal orthogonal-wheel assembly. Moreover, Swedish wheel [9] is also similar to the “orthogonal-wheels” concept.

The third group of omnidirectional mechanisms were designed based on “ball wheel” concept, to realize smooth motion and to improve step-climbing ability. Wada and Asada [14, 15] proposed a variable footprint mechanism based on a ball wheel structure and applied it to wheel chairs, but the wheel mechanism was a bit complex. Ishida *et al.* [16] also proposed a ball wheel drive mechanism for holonomic omnidirectional vehicle to improve the step climbing ability of OMRs. Tadakuma *et al.* [5] proposed an “Omni-ball” mechanism to realize high step-climbing capability.

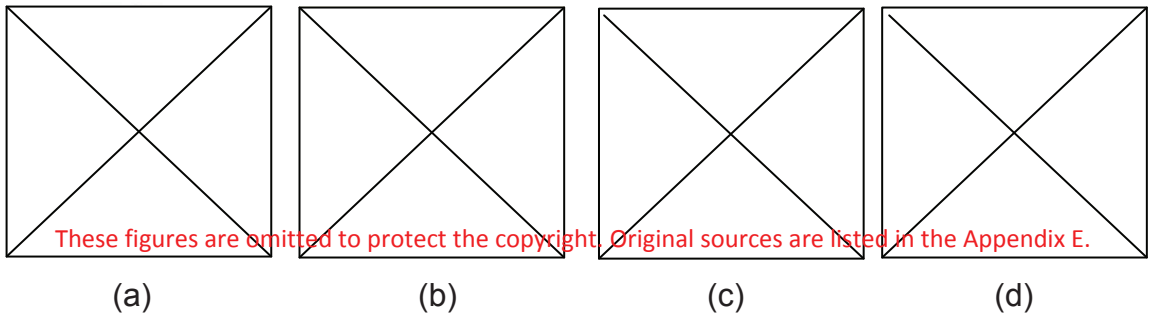


Figure 1.1: Non-switch wheel mechanisms. (a) Universal wheel [1]. (b) Mecanum wheel [2]. (c) Alternate wheel [3, 4]. (d) Ball wheel [5].

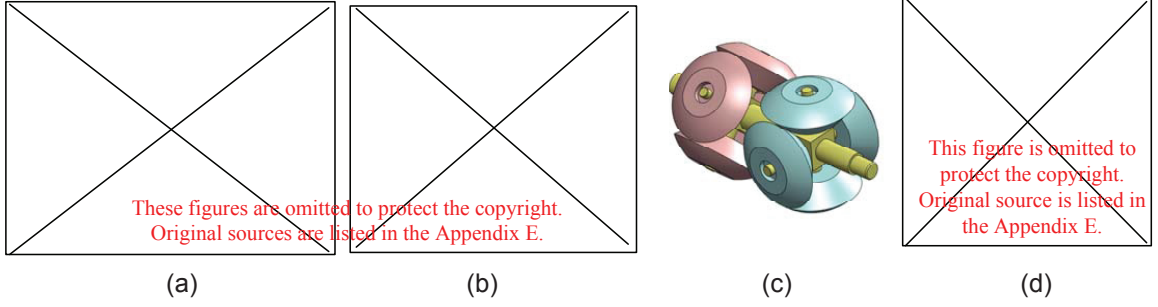


Figure 1.2: Switch wheel mechanisms. (a) Longitudinal orthogonal-wheel [6]. (b) MY wheel [7]. (c) MY wheel-II [8]. (d) Swedish wheel [9].

In addition, in our previous work [17], we divided all of these mechanisms into two groups: non-switch wheels and switch wheels, depending on whether the contact radius of the wheel to the robot geometric center switches. Majority of the wheels, such as Universal wheel [1], Mecanum wheel [2], Alternate wheel [3] and Ball wheel [5], are of the first group (see Figure 1.1). The switch wheel mechanisms proposed until now are shown in Figure 1.2. They are Longitudinal Orthogonal-wheel [6], MY wheel [7], MY wheel-II [8] and Swedish wheel [9]. The dynamics of the non-switch wheeled OMRs is nonlinear and smooth while the switch wheeled OMRs are nonlinear and piecewise-smooth dynamical systems. In fact, switch wheeled OMRs are autonomous switched nonlinear dynamical systems.

1.1.2 Applications

The high manoeuvrability provided by OMRs can be utilized in numerous indoor and outdoor applications. As already mentioned, they have the ability to easily perform certain tasks with high efficiency in congested environments with static obstacles, dynamic obstacles or in narrow spaces. As a result, practical applications of OMRs can be found in various fields, e.g., industrial field and medical field, etc. The following are a few examples.

Industrial Field

Figure 1.3 (a) shows an omnidirectional mobile platform from KUKA for transportation tasks, named KMP omniMove. The optical tracking, positioning aids and mechanical guide

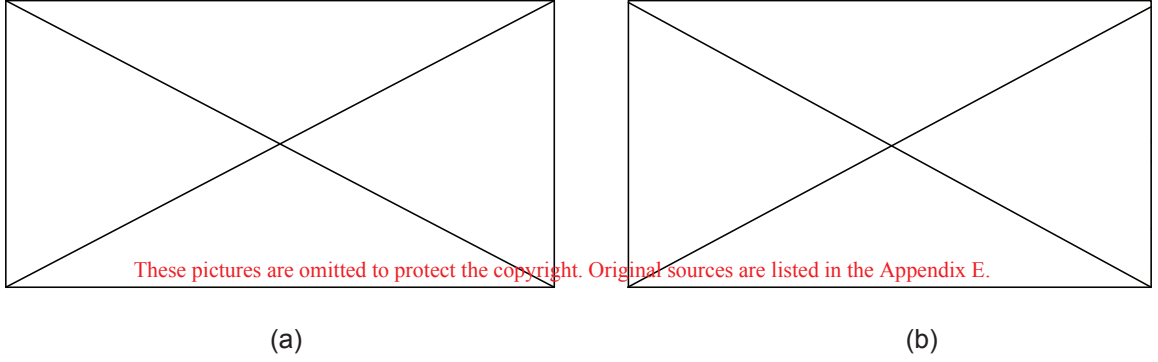


Figure 1.3: (a) KMP omniMove [10]. (b) KMR QUANTEC [11].

elements allow it to achieve a positioning accuracy of up to 1 mm. The KMP omniMove can move autonomously without risk of collision. Its unrestricted two-dimensional freedom of motion makes this possible and ensures maximum exhibility [10]. In addition, since KMP omniMove can move autonomously and precisely, the regulation or tracking control plays an important role in achieving the desired control performances, especially with high payload.

It is well-known that the movable region of mobile manipulators based nonholonomic mobile system is restricted to the setting of desired trajectory, while omnidirectional mobile manipulators do not have these constraints. Therefore, omnidirectional mobile manipulators are much more dexterous and the manipulability is greatly improved. Figure 1.3 (b) shows an omnidirectional mobile manipulator from KUKA, named KMR QUANTEC. Its omnidirectional wheel technology enables KMR QUANTEC to maneuver safely to the desired position in confined spaces and to achieve a positioning accuracy of 5 mm, no matter whether it has had to travel 5 or 150 meters to the site of operation [11]. Note that, to realize high precision of machining or operation, it is crucial that the OMR should be precisely controlled.

Medical Field

The wheelchairs based omnidirectional wheels are highly maneuverable in narrow or crowded areas such as residences, offices and hospitals. Several kinds of omnidirectional vehicle have been developed. Two examples of omnidirectional wheelchairs are shown in Figure 1.4. Recent development has made wheelchairs more intelligent, such as autonomous

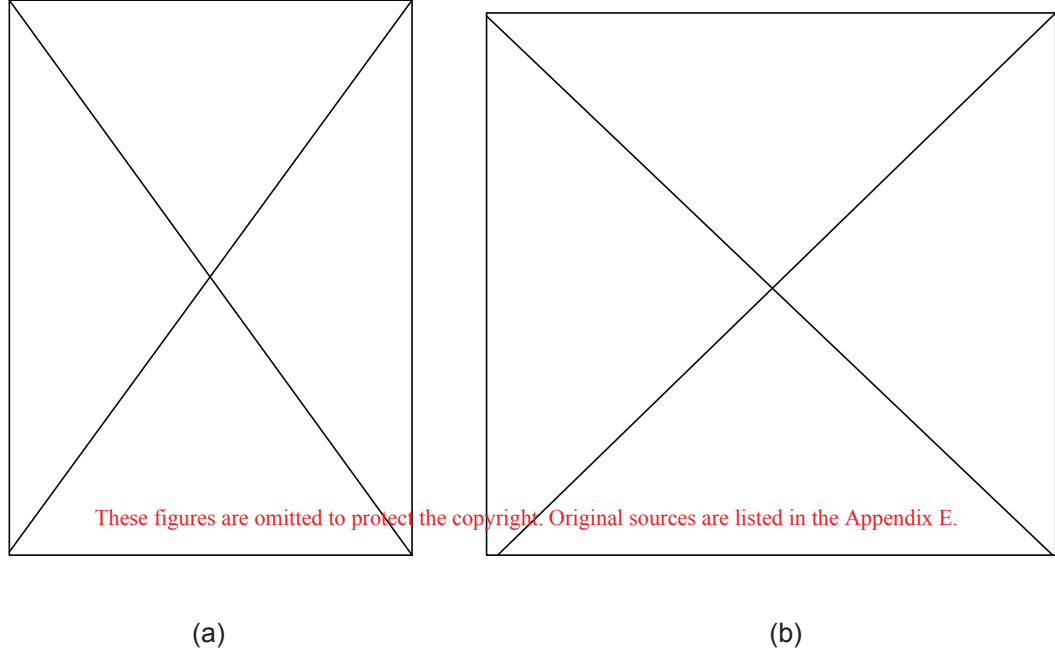


Figure 1.4: Omnidirectional wheelchairs: (a) OMR developed in University at Hagen [12]. (b) OMR developed in Chiba Institute of Technology [13].

navigation, obstacles avoidance and voice control, etc. It is obvious that the regulation or tracking control design is indispensable in realizing these functions.

As discussed above, the control system design of OMRs plays a crucial role in these applications, especially for the industrial applications since high precision is usually required.

1.2 Literature Review

1.2.1 Control of OMRs

The control of OMRs can be divided into kinematic based control and dynamic based control. Kinematic control of OMRs have been studied in [8, 9, 18, 19, 20, 21, 22, 23, 24]. It is well known that kinematic control is usually applied when the robot moves in low speed and low payload, or the control performances are not highly required. However, when the robot moves with high speed or with high payload, or high control performances are expected, the dynamic effects have to be taken into consideration to guarantee the control

performance. Therefore, in this part, we mainly focus on the literature review of dynamic based control.

Some works are based on feedback linearization control approaches. In [25], a resolved acceleration controller was designed for an omnidirectional holonomic autonomous platform, which was equipped with three Lateral orthogonal-wheel assemblies. The proposed controller is based on feedback linearization control approach and thus the control system performances depend on the accuracy of the robot dynamic model. In [26], the dynamic model of a three Swedish wheeled OMR is linearized to simplify controller design by using the kinematic relationship between its body movement and rotation velocities of wheels. In [27], a cascade control structure was applied for a three wheeled OMR with Universal wheels. The dynamic model is linearized by feedback of the friction forces, and then linear model-predictive control was designed based on the linearized dynamics. It should be noted that the modeling of the friction forces is needed to linearize the dynamic model. In [28], for a three Swedish wheeled OMR, the control system is also a cascade structure which consists of an outer-loop (kinematics) controller and an inner-loop (dynamics) controller. Both the outer-loop controller and inner-loop controller were designed using the trajectory linearization control method based on a nonlinear robot dynamic model.

In [29], based on a relaxed optimal control problem, the authors proposed an algorithm to calculate near-optimal minimum time trajectories for a four wheeled omnidirectional vehicle with Universal wheels. Adaptive control design was studied in [30, 31]. In [30], an adaptive motion controller was synthesized via the adaptive backstepping approach for a three Swedish wheeled OMR, by considering parameter variations and uncertainties caused by friction and payloads. In [31], for a three Swedish wheeled OMR, a switching algorithm was proposed to exchange of control authority between adaptive linearizing controller and adaptive sliding-mode controller. However, the parameter tuning may be tedious since several parameters are to be tuned. Observer based control system design was proposed in [32]. An output feedback control scheme was proposed based on a generalized proportional integral (GPI) observer for a three Swedish wheeled OMR. The main idea is that the

unknown, possibly state-dependent, additive nonlinearities influencing the input-output tracking error dynamics are modeled as an absolutely bounded, additive, unknown “time-varying disturbance” input signal. Then GPI observer is then employed to estimate this “time-varying disturbance” input signal. However, in this paper, the robot is directly considered as a non-switch wheeled OMR.

1.2.2 Control of Autonomous Switched Nonlinear System

Since our robot prototype is an autonomous switched nonlinear system (see Chapter 2), it is reasonable to consider the control system design based on switched system control theory. In switched system theory, in spite of the diverse switching mechanisms, the switching events can be classified into state-dependant versus time-dependant, or autonomous (uncontrolled) versus controlled. Correspondingly, in literature, the stability analysis and control design issues of the switched systems are divided into two categories, namely, systems under arbitrary switching (for autonomous switched systems) and systems under the constrained switching (for controlled switched systems) [33, 34]. Switch wheeled OMRs are autonomous switched nonlinear systems, since the switching signal depends on robot states. However, in literature, great interest has been generated in the control analysis and synthesis of switched linear systems [35, 36, 37, 38, 39], or controlled switched nonlinear systems [40, 41, 42, 43], to name a few.

For a switched system to be asymptotically stable under arbitrary switchings, it is crucial to find a common Lyapunov function for all subsystems [34]. However, a common Lyapunov function is usually difficult to derive for switched nonlinear systems. Therefore, for autonomous switched nonlinear systems, only stability analysis and set-point stabilization were studied in a few papers for some special systems [44, 45, 46, 47, 48], to name a few. The adaptive neural control and backstepping design were proposed in [44] and [45], respectively, for a special class of switched nonlinear system under several strict assumptions. For example, the switching signals are assumed to have the same persistent dwell time. In [46], model predictive control algorithm was proposed for switched nonlinear systems

with average dwell-time switching signals. In [47], stability analysis for a class of switched nonlinear systems with disturbance input and delay was studied. In [48], global finite-time stabilization was studied for a class of switched strict-feedback nonlinear systems whose subsystems have chained integrators with the powers of positive odd rational numbers.

It should be emphasized that the trajectory tracking control design for autonomous switched nonlinear systems has not yet been studied in switched system theory. The reason lies in the fact that it is difficult to establish a common Lyapunov function for all subsystems.

1.2.3 Motivation

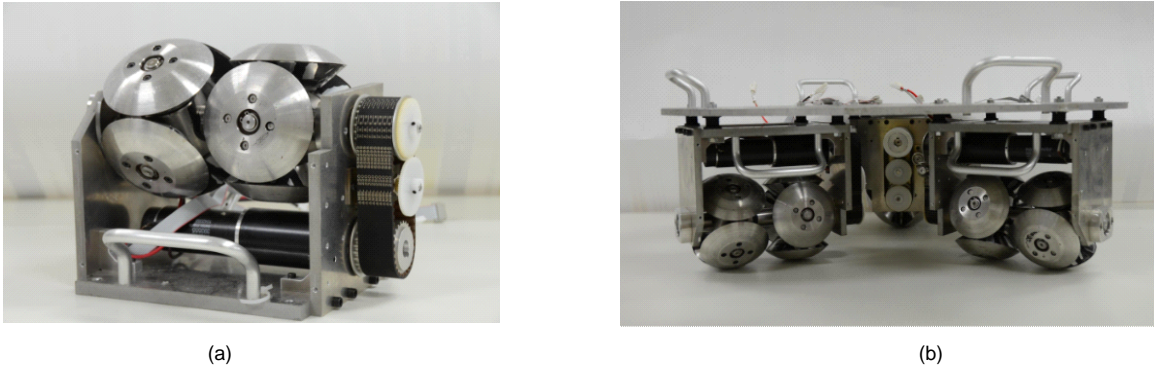


Figure 1.5: Robot prototype [8]: (a) MY wheel-II assembly. (b) A robot prototype with three MY Wheel-II assemblies.

In our lab, we have proposed an omnidirectional wheel mechanism, named MY Wheel-II, and developed a three wheeled robot prototype. Figure 1.5 shows the MY wheel-II assembly and robot prototype. As mentioned in Section 1.1.1, MY wheel-II is a switch wheeled mechanism. According to Section 1.2, all of the previous dynamic modeling and control designs are for the non-switch wheeled OMRs [25, 27, 29] and Swedish wheeled OMRs [26, 28, 30, 31, 32].

Although Swedish wheel is one of the switch wheel mechanisms, it is worthy pointing out that continuous dynamic models (i.e., simplified models) were directly employed in all of the previous controller design studies by considering it as a non-switch wheel. This

simplification is reasonable because the distance between the two small wheel parts in Swedish wheel is usually quite small compared with the wheel contact radius to the robot geometric center, producing fairly small modeling error (i.e., the switching effects can be ignored). This may be a good solution for the modeling and control design of Swedish wheeled OMRs. Nevertheless, the switching effects of the Longitudinal orthogonal wheel, MY wheel and MY wheel-II can not be ignored because the distance between the two small wheel parts in each assembly is usually relatively large compared with the contact radius to the robot geometric center.

On the other hand, since we focus on trajectory tracking control of OMRs in this study, the trajectory tracking control design for autonomous switched nonlinear systems has not yet been studied in switched system theory. Therefore, the control system of our robot prototype cannot be designed based on the current switched system theory. It is no surprise, therefore, that one current paradigm for dealing with switched systems is continuation. In this paradigm, it treats the switching dynamics as small unmodeled dynamics (and then use robust control), slowly-varying (and gain-scheduling), or rare and independent of the continuous state (jump linear systems) [49]. This motivates us to study the trajectory tracking control system design for our robot prototype based on continuous dynamic models.

1.3 Outline of This Thesis

The contents of this thesis are organized as follows:

Chapter 2 introduces the robot prototype and a dynamic model including the switching information. The motion principle of MY wheel mechanism and specifications of the prototype are presented. The experimental setup in this thesis is also introduced. Then a dynamic model considering the motor dynamics and the switching is derived. Finally, analysis of the dynamic properties of our robot prototype is presented in detail.

Chapter 3 presents two continuous dynamic models to facilitate the control design for the robot prototype, i.e., average dynamic model and nonlinear parameter varying dynamic

(NLPV) model. Then control systems are designed based on resolved acceleration control (RAC) using the two continuous dynamic models, respectively. Simulations are conducted to verify both control systems. Experimental tests are conducted for the average dynamic model based RAC.

Chapter 4 proposes a trajectory tracking control system based on a generalized proportional integral (GPI) observer for the robot prototype. The GPI observer is employed to estimate the modeling errors in the average dynamic model, i.e., 1) unmodeled switching dynamics, 2) unmodeled forces, and 3) parameter uncertainties. Bounded input bounded output (BIBO) stability is guaranteed in the designed control system. Both simulations and experimental results are presented to compare the control performances with average dynamic model based RAC.

Chapter 5 presents a passivity-based model free control (MFC) design by employing a modified GPI observer. Firstly, the passivity property of our robot prototype is analyzed based on the average dynamic model. The design objective is to propose a controller such that the passivity property of the robot is preserved in the closed-loop system by using the modified GPI observer. Stability property is analyzed based on the average dynamic model. Finally, experimental tests are conducted to compare with the control designs in previous chapters and discussions are also presented.

Chapter 6 concludes this thesis and discusses the possible works in the future.

Chapter 2

Kinematic and Dynamic Model of the Robot Prototype

In this chapter, we firstly introduce the MY wheel-II mechanism and the configuration of the robot prototype. The motion principle of MY wheel-II is also stated. Then the experimental setup is introduced, which is used in all the experiments of this thesis.

In addition, the kinematic model and dynamic model of the robot prototype are derived. A kinematic model for a switch wheeled OMR based on Longitudinal orthogonal-wheels was derived in [6]. However, in previous works of dynamic modeling of OMRs, all of dynamic models are derived for the non-switched OMRs or for Swedish wheeled OMRs by neglecting the switching effects. The dynamic model derived in this chapter is the first work for a switch wheeled OMR considering the wheel switching. More importantly, the analysis of the dynamic model is presented, which reveals the switching properties of our robot prototype.

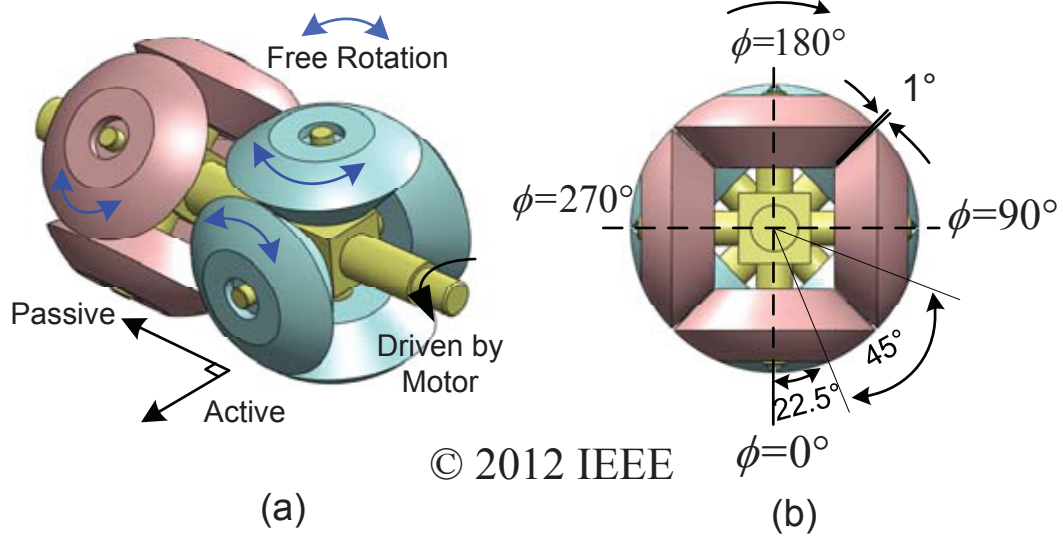


Figure 2.1: MY wheel-II mechanism: (a) Motion principle. (b) End-view.

2.1 Robot Prototype

2.1.1 MY Wheel-II Mechanism

As introduced in Section 1.1.1, various omnidirectional wheel mechanisms and robot prototypes have been developed in literature. For omnidirectional wheels based on “universal wheel” concept, these wheel mechanisms are sensitive to the rubbish on the floor, such as threads. This is because the small rollers on these wheels may easily get stuck due to these rubbish. Furthermore, these wheel mechanisms may have poor step climbing ability [5]. On the other hand, although the ball wheel mechanisms have higher step climbing ability, the ball wheel mechanisms usually have complex structure or poor payload ability, such as ball wheel mechanism proposed in [15].

In [8], we have proposed a novel omnidirectional wheel mechanism, referred to as MY wheel-II, based on “orthogonal-wheels” concept. This kind of wheel mechanism is not only insensitive to the rubbish on the floor, but also has a high payload ability and high step climbing ability.

The basic mechanism structure of the MY wheel-II mechanism is shown in Figure 2.1. The MY wheel-II consists of two balls of equal diameter on a common shaft and both balls

are sliced into four spherical crowns. Each spherical crown can rotate freely around its axis. To produce a combined circular profile, the two sets of spherical crowns are mounted at 45° from each other. The wheel mechanism has a constrained motion controlled by rotation of the main shaft, in the direction perpendicular to the shaft. The motion component in the direction parallel to the shaft is unconstrained, since the spherical crowns can freely rotate. To realize smooth motion on the ground, the two sets of crowns make alternative contact with the ground. Whenever the shaft turns 45° , the contact point with the ground switches to from one to the other. Therefore, during each turn of the wheel shaft, eight switches happen. Note that a 1° gap exists between two adjacent spherical crowns (shown in Figure 2.1 (b)).

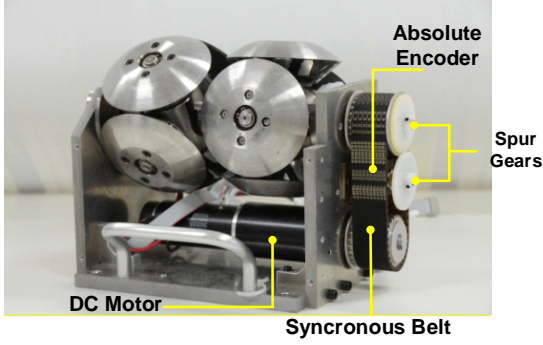
The MY wheel-II mechanism is insensitive to the fragments on the ground, since it can be seen that the rotation axis of each spherical crown lies inside the spherical crown. It also has higher step climbing ability due to the sliced ball structure, compared with other omnidirectional wheel structures, such as Swedish wheel. Moreover, the MY wheel-II mechanism has a higher payload ability compared with ball wheels such as [15].

2.1.2 Robot Prototype

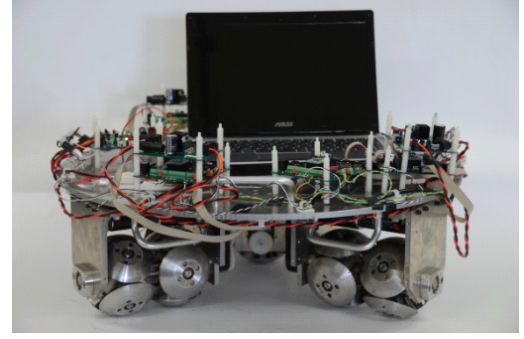
Figure 2.2 (a) shows the details of the MY wheel-II assembly. One end of the shaft is connected to the DC motor through a synchronous belt. An absolute encoder is installed to detect the switching of contact point. A pair of spur gears is employed to transmit the wheel rotation to the absolute encoder. It should be noted that the absolute encoder is indispensable for MY wheel-II, since it is used to detect the switching time of each wheel. Three MY wheel-II assemblies are arranged with a 120° interval angle underneath a steel disk (Figure 2.2 (b)). The specifications of the prototype platform are listed in Table 2.1.

2.1.3 Experimental Setup

The complete schematic of the hardware control system is shown in Figure 2.3. This is the experimental setup for all of the experiments in this thesis. The sampling time of all the



(a)



(b)

Figure 2.2: (a) MY Wheel-II assembly. (b) Prototype platform.

Table 2.1: Specifications of the prototype platform

Body Dimension	620 mm \times 190 mm
Weight	40 Kg
Payload	150 Kg
DC Motor	Maxon DC Motor 90 W \times 3
Radius of Wheel	60 mm
Contact Radius	$D_{in}=147$ mm, $D_{out}=236$ mm

experiments is 10 ms, and therefore the experimental setup is appropriate for experiments and satisfies the basic requirements for the control system verification.

The central controller board and each motor controller board were designed using dsPIC micro-controllers (dsPIC33FJ128MC804 from Microchip, USA). All of the dsPIC micro-controllers were programmed to operate at 40 million instructions per second. The three DC motors (Order number: 323890, Maxon) are identical with gear reduction ratio of 186 and nominal voltage of 24 V. Each motor is installed with an incremental encoder (Order number: 225787, Maxon). The incremental encoder is with 1024 counts per turn. The H-Bridge drivers of three DC motors are identical (LMD18200 from Texas Instruments, USA). As mentioned before, three absolute encoders (MAB2510HS5VSER from MegaMotive, Germany) are used to detect the switching of contact point with ground.

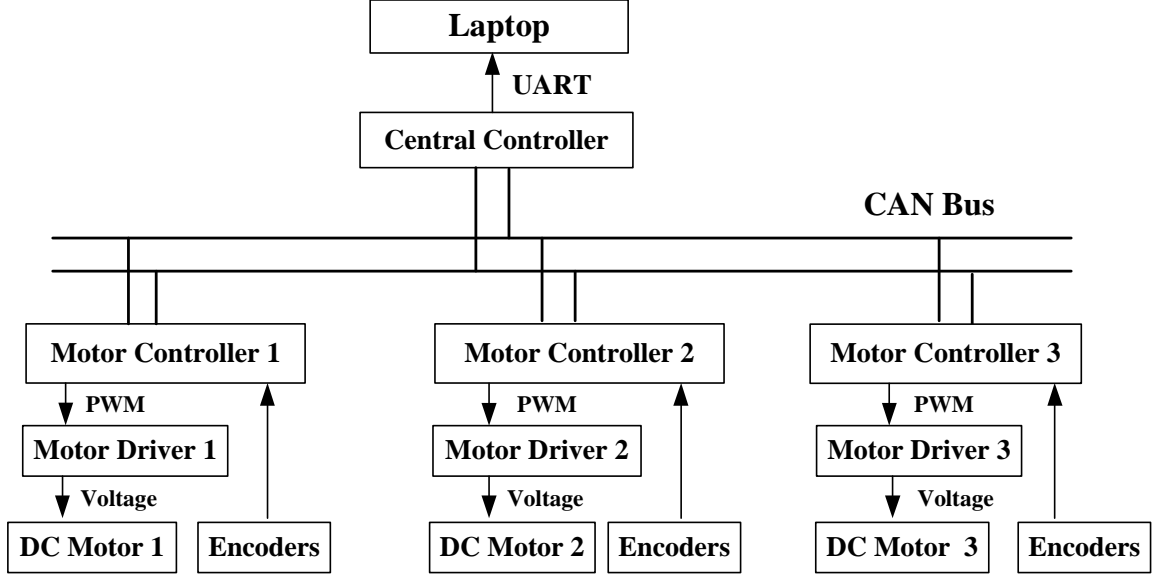


Figure 2.3: Schematic of the experimental setup.

A laptop is employed to collect and display the measured data. Communication between the laptop and the central controller is via UART, which was programmed to operate at a data transfer rate to 2.5 Mbaud. The communication between the central motor controller and the three motor controllers is via CAN bus, which was programmed to operate at 1 Mb/s. The central controller calculates the control law and generates the control input (i.e., motor voltages) to the three motor controllers. Then each motor controller generates the corresponding pulse-width modulation (PWM) signal of the control input to each motor driver. In addition, the information of each absolute encoder and incremental encoder is collected by the motor controller and then sent to the central controller. Note that the robot posture is determined using odometry which is commonly used in the tracking control study of mobile robots [50, 51, 52], to name a few. The robot velocity is obtained using the forward kinematics. Finally, the designed boards of central controller, motor controller and motor driver, are shown in Appendix B and C.

2.2 Kinematic Model and Dynamic Model

2.2.1 Kinematic Model

For the switch wheeled OMRs, kinematic modeling and analysis were studied in [6, 19, 22]. In [6], a kinematic model was derived for a mobile platform with three Longitudinal orthogonal-wheel assemblies. In this kinematic model, the switching of the contact radius is considered. That is, the discontinuous contact radius is not constant in this model. One problem is that the switching of the contact radius results in fluctuations of the motor angular velocities when calculating the motor velocities using the kinematic model. Thus, for the same kind of omnidirectional mobile platform in [19], an average wheel contact radius was used instead of the real contact radius in the inverse kinematic model, to solve the problem of motor angular velocity fluctuations. In [8] and [22], the kinematic analysis was studied by adopting an optimal scale factor (OSF) instead of using the average contact radius and the factors influencing the OSF were discussed.

The details of the kinematic model can be found in [8]. Figure 2.4 shows the two coordinate frames with definitions of the variables necessary in developing the kinematic model. The world coordinate frame $\{W\}$ is fixed on the ground and the moving coordinate frame $\{M\}$ is assumed to be fixed on the geometric center of the robot. $\dot{\Phi} = \begin{bmatrix} \dot{\phi}_1 & \dot{\phi}_2 & \dot{\phi}_3 \end{bmatrix}^T$ is the wheel angular velocity vector. $\omega = \begin{bmatrix} \omega_1 & \omega_2 & \omega_3 \end{bmatrix}^T$ is the motor angular rate. θ denotes the angle between X_W - and X_M - frame, i.e., the rotational angle of the moving coordinate frame with respect to the world coordinate frame. D_{in} and D_{out} are the contact radius from the geometric center of the robot to the inner and outer contact point with ground in each wheel assembly, respectively. r is the radius of the wheel. The posture vector the robot in the world coordinate frame is defined as $\mathbf{q} = \begin{bmatrix} x & y & \theta \end{bmatrix}^T$. The robot velocity expressed in the moving coordinate is $\mathbf{V}_M = \begin{bmatrix} V_x & V_y & \dot{\theta} \end{bmatrix}^T$.

The coordinate transformation matrix from the moving coordinate frame to the world

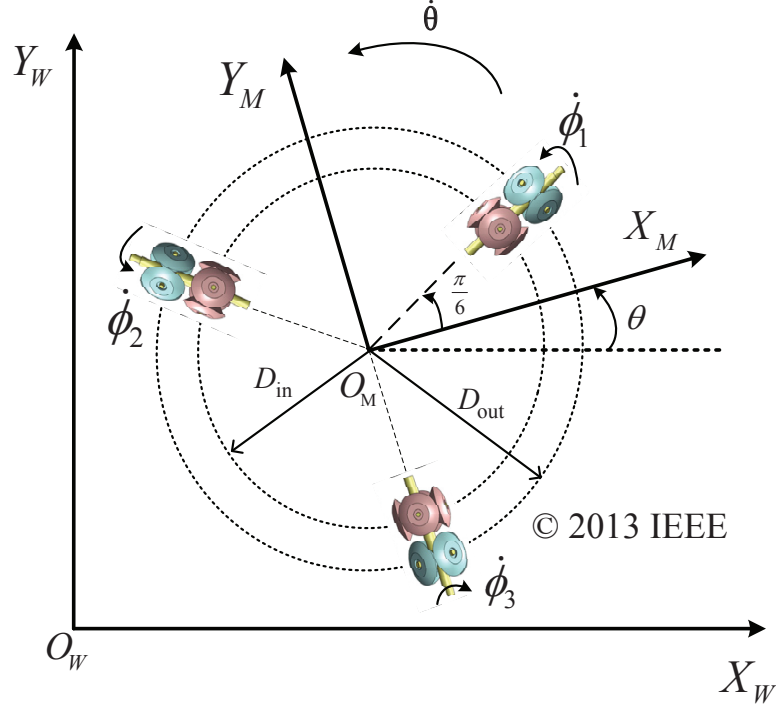


Figure 2.4: Coordinate frames of the omnidirectional mobile robot.

coordinate frame is as follows:

$${}^W_M \mathbf{R} = \begin{bmatrix} \cos \theta & -\sin \theta & 0 \\ \sin \theta & \cos \theta & 0 \\ 0 & 0 & 1 \end{bmatrix}. \quad (2.1)$$

Then we have:

$$\dot{\mathbf{q}} = {}^W_M \mathbf{R} \mathbf{V}_M. \quad (2.2)$$

The kinematic relationship in the moving coordinate can be described as follows [6][25]:

$$\begin{aligned} r\dot{\phi}_1 &= -\frac{1}{2}V_x + \frac{\sqrt{3}}{2}V_y + L_1\dot{\theta} \\ r\dot{\phi}_2 &= -\frac{1}{2}V_x - \frac{\sqrt{3}}{2}V_y + L_2\dot{\theta}, \\ r\dot{\phi}_3 &= V_x + L_3\dot{\theta} \end{aligned} \quad (2.3)$$

where L_i ($i = 1, 2, 3$) represent the distance between the geometric center of the robot and the contact point with ground of each wheel (Figure 2.4) and is given as:

$$L_i = \begin{cases} D_{in}, & \text{if } \frac{\pi}{8} + \frac{n\pi}{2} < \phi_i \leq \frac{3\pi}{8} + \frac{n\pi}{2} \\ D_{out}, & \text{if } -\frac{\pi}{8} + \frac{n\pi}{2} < \phi_i \leq \frac{\pi}{8} + \frac{n\pi}{2} \end{cases} \quad n = 0, \pm 1, \pm 2, \dots \quad (2.4)$$

where ϕ_i is the angular position of the wheel i .

Defining the motor gear reduction ratio n , we have

$$\omega = n\dot{\Phi}. \quad (2.5)$$

Combining (2.1) - (2.5), the inverse kinematic equation of the robot prototype in the world coordinate can be expressed as follows:

$$\omega = \mathbf{J}^{-1}\dot{\mathbf{q}}, \quad (2.6)$$

where $\mathbf{J}^{-1} \in \mathbb{R}^{3 \times 3}$ is given by:

$$\mathbf{J}^{-1} = \frac{n}{r} \begin{bmatrix} -\cos(\frac{\pi}{3} - \theta) & \cos(\frac{\pi}{6} + \theta) & L_1 \\ \sin(\theta - \frac{\pi}{6}) & -\cos(\frac{\pi}{6} - \theta) & L_2 \\ \cos \theta & \sin \theta & L_3 \end{bmatrix},$$

where \mathbf{J} corresponds to the Jacobian matrix relating the motor velocity vector to the robot velocity vector.

The forward kinematic equation, used in the odometry positioning method, is as:

$$\dot{\mathbf{q}} = \mathbf{J}\omega, \quad (2.7)$$

where \mathbf{J} is given by:

$$\mathbf{J} = \frac{r}{n\sqrt{3}(L_1 + L_2 + L_3)} \begin{bmatrix} J_{11} & J_{12} & J_{13} \\ J_{21} & J_{22} & J_{23} \\ \sqrt{3} & \sqrt{3} & \sqrt{3} \end{bmatrix}, \quad (2.8)$$

where

$$\begin{aligned} J_{11} &= -2L_3 \sin(\theta + \frac{\pi}{6}) - 2L_2 \sin \theta, & J_{12} &= 2L_3 \sin(\theta - \frac{\pi}{3}) + 2L_1 \sin \theta \\ J_{13} &= 2L_1 \sin(\theta + \frac{\pi}{3}) + 2L_2 \sin(\frac{\pi}{3} - \theta), & J_{21} &= 2L_3 \sin(\frac{\pi}{6} - \theta) + 2L_2 \cos \theta \\ J_{22} &= -2L_3 \sin(\theta + \frac{\pi}{6}) - 2L_1 \cos \theta, & J_{23} &= 2L_1 \sin(\theta - \frac{\pi}{6}) + 2L_2 \sin(\theta + \frac{\pi}{6}). \end{aligned}$$

It can be seen from (2.4) that the wheel contact radius switches between the inner and outer contact radius, i.e., between D_{in} and D_{out} . However, according to (2.6), it can be

seen that the motor velocity is smooth when the robot moves without rotation. The motor velocity will have fluctuations due to switching of the contact radius L_i when the robot moves with rotation. In other words, the fluctuations in the motor velocity only appear as the robot moves with rotational motion, even though the robot is a switch wheeled OMR. In addition, it should be noted that the switching frequency of the contact radius depends on the angular velocity of the wheel. In other words, the higher the angular velocity of the wheel is, the higher the switching frequency of the contact radius is. Therefore, the high switching frequency of the contact radius leads to severe fluctuations in the motor velocity. In [24], we conducted the kinematic analysis, which shows that eight possible kinematic models exist. A predictive kinematic control method was proposed by making use of eight possible kinematic models. The readers are referred to [24] for more details.

2.2.2 Dynamic Model and Analysis

Dynamic Model

Most of the dynamic models for OMRs were derived in the cartesian space [25, 26, 28, 29, 53, 54]. In [25, 26, 28, 29], dynamic models were derived for OMRs by neglecting the Viscous friction and Coulomb friction forces with ground as well as the slippage. In [53], a dynamic model was derived by considering the Viscous friction and Coulomb friction forces. Three experimental methods of estimation of Viscous friction coefficients and Coulomb friction coefficients have been proposed. A dynamic model for an OMR, considering slipping between the wheels and motion surface, as well as friction forces, has been proposed in [54]. In addition, a dynamic model was derived in polar space, neglecting the motor dynamics [30].

However, for switch wheeled OMRs, the dynamic modeling and analysis taking switching effects into consideration have not been studied in previous works. We derived and analyzed a dynamic model for our robot prototype in [17].

The dynamic model is derived based on the following assumptions, which are often

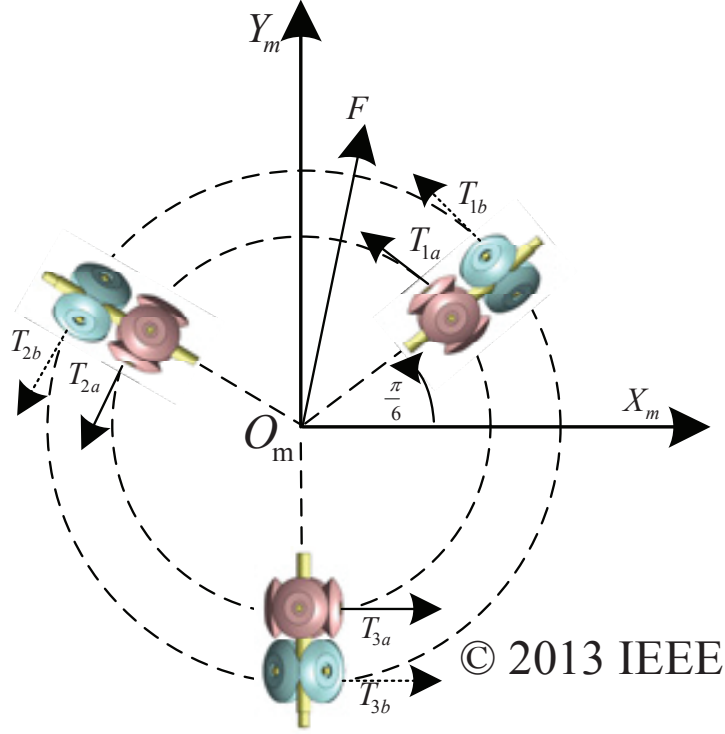


Figure 2.5: Force analysis.

made in the literature, such as [25, 28]. The wheel contact friction forces in the direction perpendicular to the traction force are ignored. It is assumed that no slippage exists between the wheel and the motion surface. The friction forces on the wheel shaft and gear are Viscous friction. The Coulomb and Viscous friction forces related to the robot motion are neglected. For the dynamic modeling and parameter estimation considering friction forces related to the robot motion, we refer readers to [53]. In addition, the motor electric circuit dynamics is neglected. The two coordinate frames used in the modeling have been shown in Figure 2.4. The nomenclature is defined in Table 2.2.

The dynamic properties of the mobile robot can be described with respect to the moving coordinate frame as [25][28]:

$$\begin{aligned}
 m(\dot{V}_x - V_y\dot{\theta}) &= F_x \\
 m(\dot{V}_y + V_x\dot{\theta}) &= F_y \\
 I_v\ddot{\theta} &= M_I,
 \end{aligned} \tag{2.9}$$

where M_I is the moment of force around the axis of the robot gravity center. F_x , F_y and

Table 2.2: Nomenclature

World coordinate frame	
$\mathbf{q} = [x \ y \ \theta]^T$	Robot position and orientation angle
Moving coordinate frame	
$\mathbf{V}_M = [V_x \ V_y \ \dot{\theta}]^T$	Robot translational velocity and rotational angular rate expressed in the moving coordinate frame
Mechanical constants	
m	Robot mass
I_v	Robot moment of inertia around the mass center of the robot
I_w	Wheel moment of inertia around the wheel shaft
r	Wheel radius
D_{in}	Inner contact radius
D_{out}	Outer contact radius
I_0	Combined moment of inertia of motor, gear train and wheel referred to the motor shaft
b_0	Combined Viscous friction coefficient of the motor, gear and wheel shaft
k_b	Motor back EMF constant
k_t	Motor torque constant
R_a	Motor armature resistance
n	Gear reduction ratio

M_I can be obtained from Figure 2.5 :

$$\begin{aligned}
 F_x &= -\frac{1}{2}T_1 - \frac{1}{2}T_2 + T_3 \\
 F_y &= \frac{\sqrt{3}}{2}T_1 - \frac{\sqrt{3}}{2}T_2 \\
 M_I &= T_1L_1 + T_2L_2 + T_3L_3,
 \end{aligned} \tag{2.10}$$

where L_i is defined in 2.4. T_i is the traction force of each assembly, $i = 1, 2, 3$, and is defined as,

$$T_i = \begin{cases} T_{ia}, & \text{if } \frac{\pi}{8} + \frac{n\pi}{2} < \phi_i \leq \frac{3\pi}{8} + \frac{n\pi}{2} \\ T_{ib}, & \text{if } -\frac{\pi}{8} + \frac{n\pi}{2} < \phi_i \leq \frac{\pi}{8} + \frac{n\pi}{2} \end{cases} \quad n = 0, \pm 1, \pm 2 \dots,$$

and ϕ_i is the angular position of the wheel shaft, $i = 1, 2, 3$.

Combining (2.9) and (2.10), the dynamic properties of the mobile robot can be described with respect to the moving coordinate frame as [25][28]:

$$\mathbf{M}_1 \dot{\mathbf{V}}_M + \mathbf{C}_1 \mathbf{V}_M = \mathbf{B}_1 \mathbf{T}, \tag{2.11}$$

where

$$\mathbf{M}_1 = \begin{bmatrix} m & 0 & 0 \\ 0 & m & 0 \\ 0 & 0 & I_v \end{bmatrix}, \quad \mathbf{C}_1 = \begin{bmatrix} 0 & -m\dot{\theta} & 0 \\ m\dot{\theta} & 0 & 0 \\ 0 & 0 & 0 \end{bmatrix},$$

$$\mathbf{B}_1 = \begin{bmatrix} -\frac{1}{2} & -\frac{1}{2} & 1 \\ \frac{\sqrt{3}}{2} & -\frac{\sqrt{3}}{2} & 0 \\ L_1 & L_2 & L_3 \end{bmatrix}, \quad \mathbf{T} = \begin{bmatrix} T_1 & T_2 & T_3 \end{bmatrix}^T.$$

The motors dynamics can be described as follows:

$$I_0 \dot{\boldsymbol{\omega}} + (b_0 + \frac{k_t k_b}{R_a}) \boldsymbol{\omega} + \frac{r}{n} \mathbf{T} = \frac{k_t}{R_a} \mathbf{u}. \quad (2.12)$$

where $\boldsymbol{\omega} = \begin{bmatrix} \omega_1 & \omega_2 & \omega_3 \end{bmatrix}^T$, $\mathbf{u} = \begin{bmatrix} u_1 & u_2 & u_3 \end{bmatrix}^T$. ω_i is the motor angular rate, u_i is the applied motor voltage.

The kinematic relationship with respect to the moving coordinate frame is given by (see (2.3)):

$$\dot{\boldsymbol{\Phi}} = \frac{1}{r} \mathbf{J}_M \mathbf{V}_M, \quad (2.13)$$

$$\boldsymbol{\omega} = n \dot{\boldsymbol{\Phi}}, \quad (2.14)$$

$$\text{where } \dot{\boldsymbol{\Phi}} = \begin{bmatrix} \dot{\phi}_1 & \dot{\phi}_2 & \dot{\phi}_3 \end{bmatrix}^T, \quad \mathbf{J}_M = \begin{bmatrix} -\frac{1}{2} & \frac{\sqrt{3}}{2} & L_1 \\ -\frac{1}{2} & -\frac{\sqrt{3}}{2} & L_2 \\ 1 & 0 & L_3 \end{bmatrix}.$$

From (2.11) - (2.14), we obtain the dynamic model of the mobile robot expressed in the moving coordinate frame:

$$\mathbf{M}_2 \dot{\mathbf{V}}_M + \mathbf{C}_2 \mathbf{V}_M = \mathbf{B}_2 \mathbf{u}, \quad (2.15)$$

where

$$\mathbf{M}_2 = \begin{bmatrix} \frac{3}{2}\beta_0 + m & 0 & \beta_0(-\frac{L_1+L_2-2L_3}{2}) \\ 0 & \frac{3}{2}\beta_0 + m & \frac{\sqrt{3}}{2}\beta_0(L_1 - L_2) \\ \beta_0(-\frac{L_1+L_2-2L_3}{2}) & \frac{\sqrt{3}}{2}\beta_0(L_1 - L_2) & \beta_0(L_1^2 + L_2^2 + L_3^2) + I_v \end{bmatrix},$$

Table 2.3: Contact modes of the three-wheeled mobile robot

L_1, L_2, L_3	D_{in}, D_{in}, D_{in}	D_{in}, D_{in}, D_{out}	D_{in}, D_{out}, D_{in}	D_{in}, D_{out}, D_{out}
Contact Mode	Mode 1	Mode 2	Mode 3	Mode 4
L_1, L_2, L_3	D_{out}, D_{in}, D_{in}	D_{out}, D_{in}, D_{out}	D_{out}, D_{out}, D_{in}	$D_{out}, D_{out}, D_{out}$
Contact Mode	Mode 5	Mode 6	Mode 7	Mode 8

$$\mathbf{C}_2 = \begin{bmatrix} \frac{3}{2}\beta_1 & -m\dot{\theta} & \beta_1(-\frac{L_1+L_2-2L_3}{2}) \\ m\dot{\theta} & \frac{3}{2}\beta_1 & \frac{\sqrt{3}}{2}\beta_1(L_1 - L_2) \\ \beta_1(-\frac{L_1+L_2-2L_3}{2}) & \frac{\sqrt{3}}{2}\beta_1(L_1 - L_2) & \beta_1(L_1^2 + L_2^2 + L_3^2) \end{bmatrix},$$

$$\mathbf{B}_2 = \beta_2 \begin{bmatrix} -\frac{1}{2} & -\frac{1}{2} & 1 \\ \frac{\sqrt{3}}{2} & -\frac{\sqrt{3}}{2} & 0 \\ L_1 & L_2 & L_3 \end{bmatrix},$$

$$\beta_0 = \frac{n^2 I_0}{r^2}, \beta_1 = \frac{n^2}{r^2} (b_0 + \frac{k_t k_b}{R_a}), \beta_2 = \frac{n k_t}{r R_a}.$$

Finally, the robot dynamic model in the world coordinate frame can be obtained by combining (2.1), (2.2) and (2.15):

$$\mathbf{M}\ddot{\mathbf{q}} + \mathbf{C}\dot{\mathbf{q}} = \mathbf{B}\mathbf{u}, \quad (2.16)$$

where $\mathbf{M} = \mathbf{M}_2^W \mathbf{R}^T$, $\mathbf{C} = \mathbf{C}_2^W \mathbf{R}^T - \mathbf{M}_2^W \mathbf{R}^T \dot{\mathbf{R}}^W \mathbf{R}^T$, $\mathbf{B} = \mathbf{B}_2$.

Analysis

As one MY wheel-II assembly has two contact modes with the ground, i.e., inner wheel contact with contact radius D_{in} and outer wheel contact with contact radius D_{out} , the mobile robot with three MY wheel-II assemblies has eight contact modes in total. All of the contact modes are listed in Table 2.3. Each contact mode corresponds to a smooth

nonlinear robot dynamical subsystem. Therefore, the robot has eight nonlinear smooth dynamical subsystems in total and switches between these subsystems, i.e., a switched nonlinear system. In other words, the dynamic model (2.16) expresses a switched nonlinear system. On the other hand, the robot dynamic system can also be regarded as a piecewise-smooth nonlinear dynamical system. The smoothness is lost only at the instantaneous and discrete switching events. Therefore, the robot dynamical system can also be considered as continuous-time dynamical system with discrete switch events [34].

As discussed in [28], for a non-switch wheeled OMR, the mobile robot is a linear dynamical system if either the robot does not rotate while in translational motion, or the robot rotates at a fixed position without translational motion, and the nonlinearity is introduced when the robot moves with both translational and rotational motion. However, for the switch wheeled OMR, the robot is a smooth linear system only if the robot moves without rotation, which can be derived from (2.9) and (2.10). In addition, the robot is a switched linear system when it rotates at a fixed position without translational motion. When the robot moves with both translation and rotation simultaneously, the robot is a switched nonlinear system. In other words, although the switch wheeled mobile robot has eight contact modes in total regardless of whether the robot moves with rotation, the nonlinearity and switching of the robot dynamics are introduced only when the robot moves with rotation. For a detailed kinematic analysis of the robot motion with and without robot rotation, we refer readers to [6].

Moreover, switched systems are a class of hybrid dynamical systems consisting of a family of subsystems, and a rule (i.e., switching signal) that orchestrates the switching between them [34]. For the switch wheeled OMRs, as shown in (2.15) and (2.16), the switching signal is the wheel contact radius, i.e., $\mathbf{L} = \begin{bmatrix} L_1 & L_2 & L_3 \end{bmatrix}^T$. It is worth pointing out that the switching signal depends simultaneously on the contact radius of the three wheels, i.e., the vector \mathbf{L} . In other words, the current active subsystem is determined by the value of L_1 , L_2 and L_3 . For instance, at one time instant, if the contact radius of the

three wheels is $\mathbf{L} = \begin{bmatrix} D_{in} & D_{in} & D_{in} \end{bmatrix}^T$, it can be seen from Table 2.3 that the current active subsystem is Contact Mode 1.

As already mentioned in Chapter 1, in spite of the diverse switching mechanisms, the switching events can be classified into state-dependant versus time-dependant, or autonomous (uncontrolled) versus controlled [34, 49]. As shown in Table 2.3, the contact mode depends directly on the contact radius L_i , $i = 1, 2, 3$, while the latter depends on the wheel angular positions (see (2.4)). At any instant of time, the wheel angular position depends on the robot position, velocity and initial wheel angular positions. Therefore, the switch wheeled OMRs can be viewed as state-dependant switching systems. On the other hand, there is no direct control over the switching mechanism that triggers the switching of the contact modes. Thereby, the switch wheeled OMRs are autonomous switching systems, since the switching happens when the robot states hit “certain boundaries” [34, 49].

Finally, it is worth pointing out that a three-wheeled OMR based on any one of the four switch wheels (see Figure 1.2) has only eight contact modes in total, regardless of the number of switches during each wheel turn. This is because each of the four kinds of switch wheels switch wheel mechanism has only two contact modes. However, the number of switches of the wheel contact radius during each wheel turn will influence the switching frequency of the contact modes. For instance, as shown in Figure 1.2, for wheels of the same size, the Swedish wheel has the maximum of switches in each turn. Therefore, for the same robot trajectory, Swedish wheeled OMRs have the largest switching frequency between the contact modes, compared with other switched wheeled OMRs of the same size.

2.3 Summary

In this chapter, we have introduced the details of the MY wheel-II mechanism and assembly, such as the mechanical wheel structure and motion principle. The specifications of the prototype platform have also been introduced. In addition, the hardware control system has also been introduced in detail, which is the experimental setup for all of the

experiments in this thesis. Then the forward and inverse kinematic models have been derived. The forward kinematic model is used in the robot positioning based on odometry method. A dynamic model considering the motor dynamics and the switching has been derived. Analysis of the dynamic properties has been presented, which shows that the robot has eight smooth nonlinear subsystems and is an autonomous switched nonlinear system. The switching signal is the wheel contact radius, i.e., $\mathbf{L} = \begin{bmatrix} L_1 & L_2 & L_3 \end{bmatrix}^T$.

Chapter 3

Resolved Acceleration Control (RAC)

In Chapter 2, we have analyzed that the robot prototype is an autonomous switched nonlinear dynamic system. It consists of eight continuous nonlinear dynamic subsystems. As stated in Section 1.2.2, because of the difficulties in control of switched nonlinear systems, studies in the literature are focused on stabilization control of some special switched nonlinear systems. In particular, the trajectory tracking control of autonomous switched nonlinear system has not yet been studied in switched system theory.

On the other hand, in the control theory, most of the analysis and control synthesis approaches are based on continuous models. In fact, one current paradigm for dealing with switched nonlinear system is continuation [49]. That is, to control a switched nonlinear system, the first step is to derive a continuous model for the switched nonlinear system and then design controller based on the derived continuous model. The resulting switching dynamics is considered as unmodeled dynamics or disturbances to the nominal dynamic model.

As a result, to control our robot prototype, continuous dynamic modeling is expected for the robot prototype. In this chapter, we firstly present two continuous dynamic models,

namely average dynamic model and nonlinear parameter varying (NLPV) dynamic model, to facilitate the model-based control design. Simulations are conducted to compare the above two dynamic models in terms of modeling accuracy. Note that, since both models are derived from the switched nonlinear model (2.16), it can only be guaranteed that the derived two continuous dynamic models approach the switched nonlinear dynamic model in terms of accuracy, rather than the robot prototype.

Next, based on the derived two continuous dynamic models, a traditional feedback linearization control method, i.e., resolved acceleration control (RAC), is employed to design controllers for the robot prototype. Simulations results, comparisons and discussions are presented. In addition, the performances of the average dynamic model based RAC have also been verified through experiments.

Finally, it is worthy mentioning that a switched system does not necessarily inherit the properties of its constituent subsystems. For example, it is possible for the switched system to get instability by switching between asymptotically stable systems [33]. As a result, even though the feedback linearization controller is designed for each subsystem and the asymptotic stability is assured for each subsystem, the stability of the whole switched nonlinear system cannot be guaranteed.

3.1 Continuous Dynamic Modeling

In this section, we will derive two continuous dynamic models. It is the switching of the contact radius (discontinuous) that results in the robot prototype a switched nonlinear system (discontinuous system). Therefore, one continuous model is called average dynamic model, which is derived using the average contact radius instead of the switching contact radius while regarding the parameter errors as modeling errors. To further reduce the modeling errors of the average dynamic model, a new model is derived by replacing the real discontinuous contact radius in the switched nonlinear dynamic model (2.16) with an adaptive continuous curve. This dynamic model is called NLPV dynamic model.

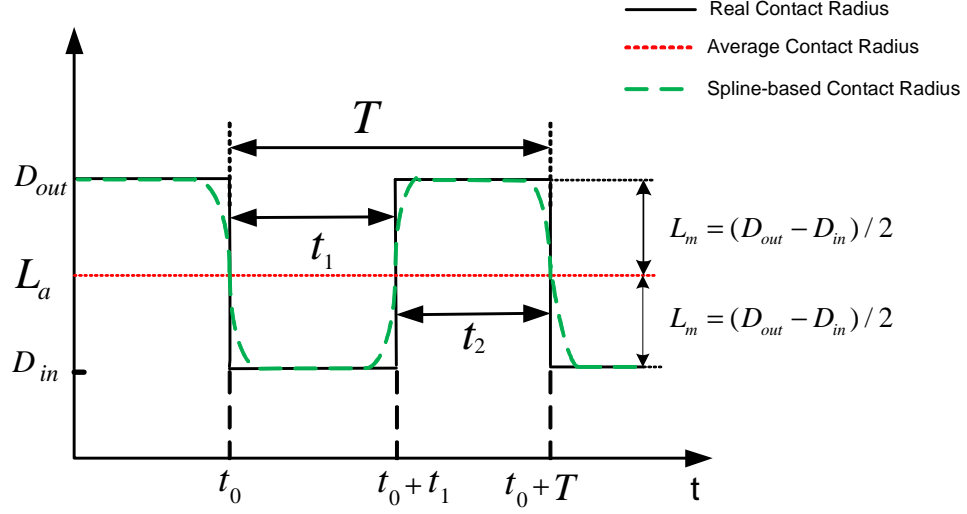


Figure 3.1: The real contact radius (solid black line), average contact radius (dotted red line) and spline contact radius (dashed green line).

3.1.1 Average Dynamic Model

As shown in (2.15), discontinuity is introduced into the robot dynamics because of the discontinuous contact radius L_i , $i = 1, 2, 3$. Therefore, a simple way to derive an average dynamic model is to use the average contact radius L_a instead of the real contact radius in the discontinuous dynamic model (2.16); that is,

$$L_i = L_a = \frac{D_{out} + D_{in}}{2} \quad i = 1, 2, 3.$$

Define $\mathbf{q}_{av} = \begin{bmatrix} x_{av} & y_{av} & \theta_{av} \end{bmatrix}^T$ as the robot posture vector in the average model, then the average model can be written as:

$$\mathbf{M}_{av} \ddot{\mathbf{q}}_{av} + \mathbf{C}_{av} \dot{\mathbf{q}}_{av} = \mathbf{B}_{av} \mathbf{u}, \quad (3.1)$$

where

$$\mathbf{M}_{av} = \mathbf{M}_{2avM}^W \mathbf{R}_{av}^T, \quad \mathbf{C}_{av} = \mathbf{C}_{2avM}^W \mathbf{R}_{av}^T - \mathbf{M}_{2avM}^W \mathbf{R}_{avM}^T \dot{\mathbf{R}}_{avM}^W \mathbf{R}_{av}^T,$$

$$\mathbf{M}_{2av} = \begin{bmatrix} \frac{3}{2}\beta_0 + m & 0 & 0 \\ 0 & \frac{3}{2}\beta_0 + m & 0 \\ 0 & 0 & 3\beta_0 L_a^2 + I_v \end{bmatrix}, \quad \mathbf{C}_{2av} = \begin{bmatrix} \frac{3}{2}\beta_1 & -m\dot{\theta}_{av} & 0 \\ m\dot{\theta}_{av} & \frac{3}{2}\beta_1 & 0 \\ 0 & 0 & 3\beta_1 L_a^2 \end{bmatrix},$$

$$\mathbf{B}_{av} = \beta_2 \begin{bmatrix} -\frac{1}{2} & -\frac{1}{2} & 1 \\ \frac{\sqrt{3}}{2} & -\frac{\sqrt{3}}{2} & 0 \\ L_a & L_a & L_a \end{bmatrix}, \quad {}^W_M \mathbf{R}_{av} = \begin{bmatrix} \cos \theta_{av} & -\sin \theta_{av} & 0 \\ \sin \theta_{av} & \cos \theta_{av} & 0 \\ 0 & 0 & 1 \end{bmatrix}.$$

and β_0 , β_1 and β_2 are the same as those in (2.15).

The fact that it is easy to derive is a distinct advantage of the average dynamic model (3.1). The derived average dynamic model is continuous and nonlinear, and does not require the detection of switching time, abolishing the need of encoder. As the average dynamic model is derived from the switched nonlinear dynamic model (2.16), its modeling accuracy depends on whether the switched nonlinear dynamic model is accurate in modeling the robot prototype.

However, the average dynamic model has large parameter errors compared with switched nonlinear dynamic model. As shown in Figure 3.1, the real contact radius in the subinterval $(t_0, t_0 + t_1)$ and $(t_0 + t_1, t_0 + T)$ is D_{in} and D_{out} , respectively, whereas the contact radius in the average dynamic modeling method is L_a (dotted red line). The resulting error in the parameter L_i is $\pm(D_{out} - D_{in})/2$. In addition, this problem becomes much more pronounced especially when the following condition is violated, producing large modeling errors:

$$\frac{L_m}{L_a} \ll 1, \quad (3.2)$$

where $L_m = \frac{D_{out} - D_{in}}{2}$. In other words, the real contact radius L_i can be considered as the nominal contact radius L_a in the average dynamic model with parameter variations. If the condition (3.2) is not satisfied, it means that the parameter variations are too large. In this case, the nominal contact radius L_a in the average dynamic model has large errors compared with the real contact radius L_i , resulting in large modeling errors.

Moreover, the condition (3.2) is equivalent to the following equation:

$$\gamma = \frac{D_{out} - D_{in}}{D_{in}} \ll 1. \quad (3.3)$$

In other words, to reduce the modeling errors of average dynamic model, the distance between the two wheel sets (i.e., $D_{out} - D_{in}$) of the MY wheel-II should be sufficiently small compared with the contact radius (i.e., D_{in} or D_{out}). Equation (3.3) also explains why Swedish wheels are commonly regarded as non-switch wheels in literature. For a Swedish wheeled OMR, the distance between the two wheel sets is usually quite small compared the contact radius. Therefore, the average dynamic modeling approach for Swedish wheeled OMRs produces very small parameter errors in the contact radius L_i . However, for a switch wheeled OMR with large γ , the average modeling approach results in significant modeling errors.

3.1.2 Nonlinear Parameter Varying Dynamic Model

Since the average dynamic modeling approach results in large modeling errors if OMRs are with large γ , such as our robot prototype ($\gamma = 0.61$), more accurate continuous modeling approach is thereby expected. In this subsection, we first analyze the two conditions leading to the switching of MY wheel-II. Then based on the two switching conditions, we propose a NLPV model derived from the switched nonlinear dynamic model (3.1).

Switching Conditions

Since each MY wheel-II assembly has two contact radius with the ground, i.e., D_{in} and D_{out} , the contact radius switches between the inner contact and outer contact when the wheel rotates. According to (2.4), we define:

$$\phi_{i0} = \begin{cases} \phi_{i0}^{in} = \phi_i - \frac{\pi}{8} - \frac{n\pi}{2}, & \text{if } L_i = D_{in}, \\ \phi_{i0}^{out} = \phi_i + \frac{\pi}{8} - \frac{n\pi}{2}, & \text{if } L_i = D_{out}, \end{cases} \quad n = 0, \pm 1, \pm 2 \dots \quad (3.4)$$

For MY wheel-II, the two conditions resulting in the switching of the contact radius are given as follows:

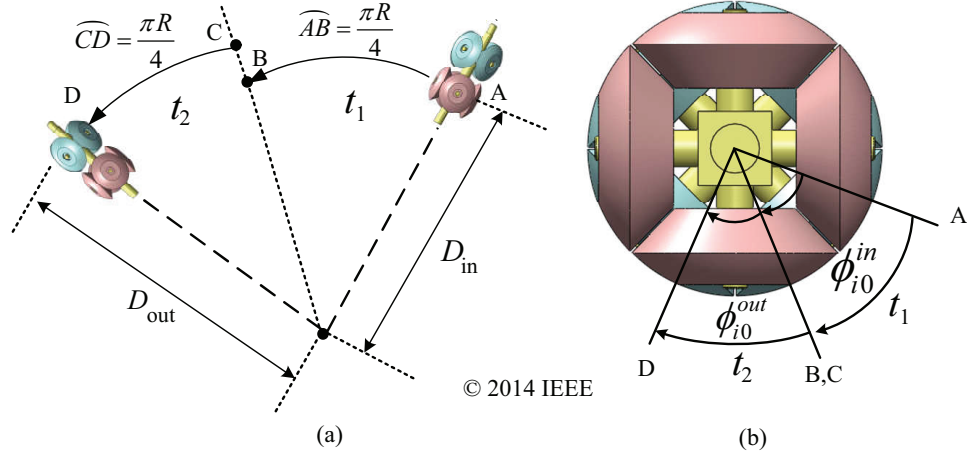


Figure 3.2: Switching condition (i): (a) Top view. (b) End view.

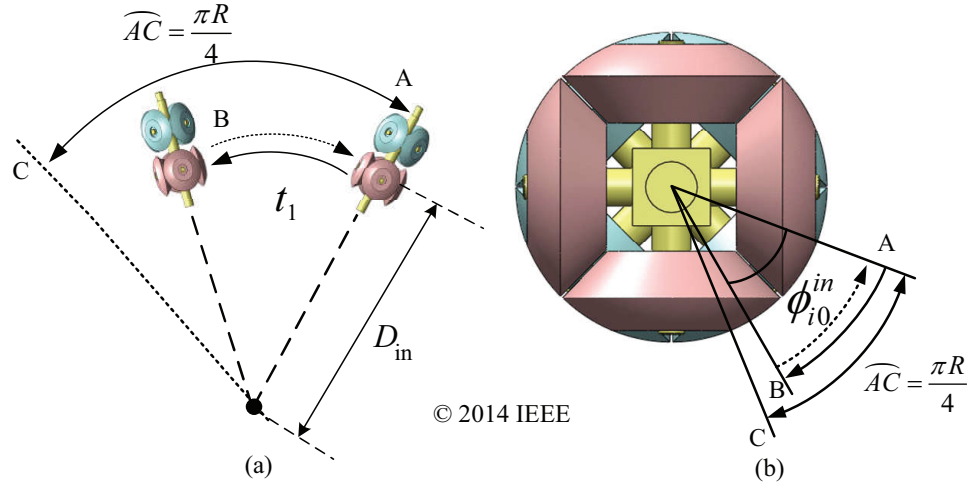


Figure 3.3: Switching condition (ii): (a) Top view. (b) End view.

(i) if the wheel rotates in one direction, i.e., forward or backward, the contact radius switches whenever the wheel rotates $\frac{\pi}{4}$, i.e., $\phi_{i0}^{in} = \frac{\pi}{4}$ or $\phi_{i0}^{out} = \frac{\pi}{4}$ (see Figure 3.2).

(ii) if the wheel changes its direction of rotation, the turned angle of the wheel resulting in the switch depends on the wheel angular position before changing the direction, i.e., ϕ_{i0}^{in} or ϕ_{i0}^{out} ($0 \leq \phi_{i0}^{in}, \phi_{i0}^{out} < \frac{\pi}{4}$) (see Figure 3.3).

Figure 3.2 shows a wheel switching example under condition (i). As shown in Figure 3.2, the wheel switches from the inner wheel contact to the outer wheel contact. It firstly moves along \widehat{AB} with inner wheel contacting with the ground. Then it switches to outer

wheel contact, and moves along \widehat{CD} . It can be obtained that the turned angle of the wheel resulting in switching of the contact radius is $\frac{\pi}{4}$.

Figure 3.3 shows an example of a wheel switching under condition (ii). As shown in Figure 3.3, the change of the wheel rotation direction occurs during the inner wheel contact. It can be seen that during the inner wheel contact, the wheel first moves along \widehat{AB} in one direction. Then it changes the rotation direction and moves along \widehat{BA} . In this case, the turned angle of the wheel resulting in the switching of contact radius is ϕ_{i0}^{in} .

As discussed previously, it is known that the average dynamic modeling approach produce an error of $\pm L_m$ in the contact radius L_i . Therefore, it is reasonable that to derive a more accurate dynamic model can be achieved by reducing this parameter error $\pm L_m$. To this end, our efforts are to seek a continuous curve that approaches the real discontinuous contact radius D_{in} and D_{out} in the subinterval $(t_0, t_0 + t_1)$ and $(t_0 + t_1, t_0 + T)$, respectively. Figure 3.1 shows an example using spline curve to approach the real discontinuous contact radius (see the dashed green line). It is obvious that approximating the real contact radius L_i by the spline curve produces much smaller parameter errors than the average contact radius L_a . As a result, in our proposed modeling approach, the real discontinuous contact radius L_i in (2.16) is directly replaced with a continuous curve, such as the spline curve, resulting in a NLPV model. Note that in this approach, the parameter error of the contact radius is small regardless of large γ , compared with the average modeling approach. Therefore, the NLPV model can predict robot behavior much more accurately than the average dynamic model, regardless of large γ of a switch wheeled OMR.

However, unfortunately, periodic switching of the contact radius L_i establishes only under some special conditions (see Appendix A). In other words, the switching of the contact radius L_i is non-periodic in most cases. A continuous curve that approaches periodic switching of the contact radius can be simply designed. For non-periodic switching of the contact radius, the difficulty lies in the fact that the designed continuous curve should adaptively approach the non-periodic switching of the contact radius. Fortunately, this

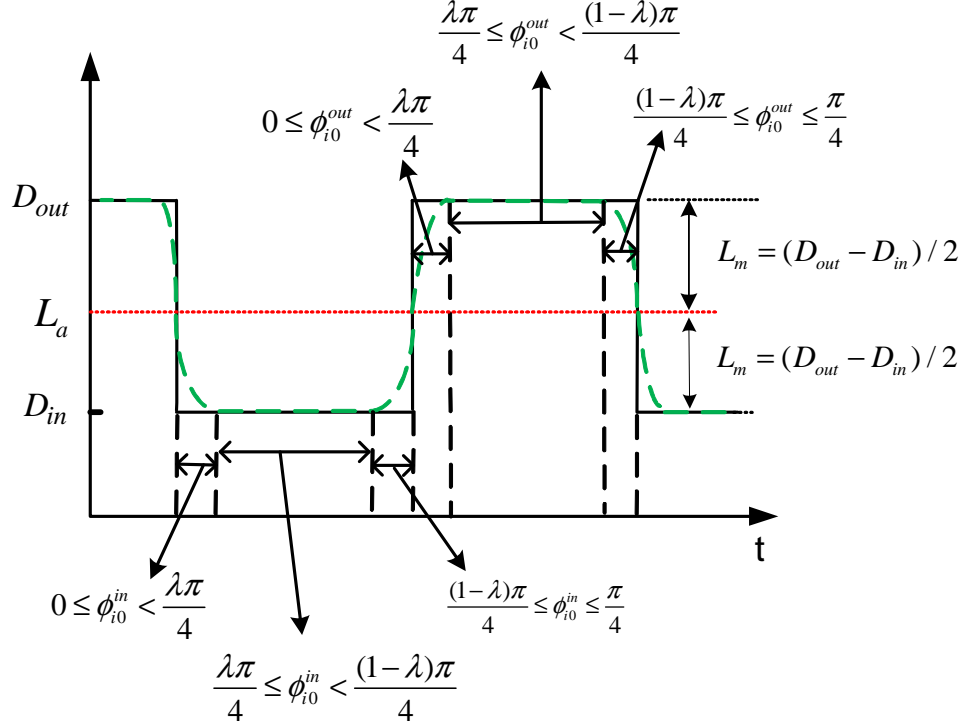


Figure 3.4: Example of adaptive spline curve.

problem can be easily solved based on the derived switching conditions, regardless of periodic or non-periodic switching of the contact radius.

In the following, as an example, a simple spline L_i^{sp} is designed to adaptively approach the discontinuous contact radius L_i (Figure 3.4). The spline curve is the combination of sine curve and line segment. Based on the switching conditions (i) and (ii), it is found that the MY wheel-II turns through a maximum angle of $\frac{\pi}{4}$ when the switching of contact radius happens. This is an essential property of the MY wheel-II mechanism. According to this property, the key idea of the adaptive curve design is that the ϕ_{i0}^{in} and ϕ_{i0}^{out} can be used as the variables of the sine curve. Note that since the switching of the contact radius alternates between D_{in} and D_{out} , it is easy to understand that the period of the sinusoid curve should be set as $\frac{\pi}{2}$. Finally, the adaptive spline L_i^{sp} is obtained as follows:

Define $0 < \lambda < 1$, and λ is an adjustable parameter,

$$L_i^{sp} = \begin{cases} L_{i_in}^{sp}, & \text{if } L_i = D_{in} \\ L_{i_out}^{sp}, & \text{if } L_i = D_{out} \end{cases} \quad (3.5)$$

if $L_i = D_{in}$,

$$L_i^{sp} = \begin{cases} L_a - L_m \sin(\frac{2}{\lambda} \phi_{i0}^{in}), & 0 \leq \phi_{i0}^{in} < \frac{\lambda\pi}{4} \\ D_{in}, & \frac{\lambda\pi}{4} \leq \phi_{i0}^{in} < \frac{(1-\lambda)\pi}{4} \\ L_a - L_m \cos[\frac{2}{\lambda}(\phi_{i0}^{in} - \frac{(1-\lambda)\pi}{4})], & \frac{(1-\lambda)\pi}{4} \leq \phi_{i0}^{in} \leq \frac{\pi}{4} \end{cases}$$

if $L_i = D_{out}$,

$$L_i^{sp} = \begin{cases} L_a + L_m \sin(\frac{2}{\lambda} \phi_{i0}^{out}), & 0 \leq \phi_{i0}^{out} < \frac{\lambda\pi}{4} \\ D_{out}, & \frac{\lambda\pi}{4} \leq \phi_{i0}^{out} < \frac{(1-\lambda)\pi}{4} \\ L_a + L_m \cos[\frac{2}{\lambda}(\phi_{i0}^{out} - \frac{(1-\lambda)\pi}{4})], & \frac{(1-\lambda)\pi}{4} \leq \phi_{i0}^{out} \leq \frac{\pi}{4} \end{cases}$$

where L_a and L_m are the same as those defined in (3.2). Since the spline curve is designed based on the above two switching conditions, it is able to adaptively approach all of the contact radius L_i , regardless of periodic or non-periodic switching of the contact radius.

Now, a NLPV continuous dynamic model is obtained by directly replacing the real discontinuous contact radius L_i with the continuous spline L_i^{sp} in the switched nonlinear dynamic model (2.16), which is as follows:

$$\mathbf{M}^{sp} \ddot{\mathbf{q}}_{sp} + \mathbf{C}^{sp} \dot{\mathbf{q}}_{sp} = \mathbf{B}^{sp} \mathbf{u}, \quad (3.6)$$

where $\mathbf{q}_{sp} = \begin{bmatrix} x_{sp} & y_{sp} & \theta_{sp} \end{bmatrix}^T$, $\mathbf{M}^{sp} = \mathbf{M}_1^{sp} (\mathbf{W}_M \mathbf{R}^{sp})^T$, $\mathbf{C}^{sp} = \mathbf{C}_1^{sp} (\mathbf{W}_M \mathbf{R}^{sp})^T - \mathbf{C}_1^{sp} (\mathbf{W}_M \mathbf{R}^{sp})^T \mathbf{W}_M \dot{\mathbf{R}}^{sp} (\mathbf{W}_M \mathbf{R}^{sp})^T$, $\mathbf{B}^{sp} = \mathbf{B}_1^{sp}$.

$$\begin{aligned}
\mathbf{M}_1^{sp} &= \begin{bmatrix} \frac{3}{2}p_0 + m & 0 & p_0(-\frac{L_1^{sp}+L_2^{sp}-2L_3^{sp}}{2}) \\ 0 & \frac{3}{2}p_0 + m & \frac{\sqrt{3}}{2}p_0(L_1^{sp} - L_2^{sp}) \\ p_0(-\frac{L_1^{sp}+L_2^{sp}-2L_3^{sp}}{2}) & \frac{\sqrt{3}}{2}p_0(L_1^{sp} - L_2^{sp}) & p_0p_3 + I_v \end{bmatrix}, \\
\mathbf{C}_1^{sp} &= \begin{bmatrix} \frac{3}{2}p_1 & -m\dot{\theta}_{sp} & p_1(-\frac{L_1^{sp}+L_2^{sp}-2L_3^{sp}}{2}) \\ m\dot{\theta}_{sp} & \frac{3}{2}p_1 & \frac{\sqrt{3}}{2}p_1(L_1^{sp} - L_2^{sp}) \\ p_1(-\frac{L_1^{sp}+L_2^{sp}-2L_3^{sp}}{2}) & \frac{\sqrt{3}}{2}p_1(L_1^{sp} - L_2^{sp}) & p_1p_3 \end{bmatrix}, \\
\mathbf{B}_1^{sp} &= p_2 \begin{bmatrix} -\frac{1}{2} & -\frac{1}{2} & 1 \\ \frac{\sqrt{3}}{2} & -\frac{\sqrt{3}}{2} & 0 \\ L_1^{sp} & L_2^{sp} & L_3^{sp} \end{bmatrix}, \quad {}^W_M \mathbf{R}^{sp} = \begin{bmatrix} \cos \theta_{sp} & -\sin \theta_{sp} & 0 \\ \sin \theta_{sp} & \cos \theta_{sp} & 0 \\ 0 & 0 & 1 \end{bmatrix},
\end{aligned}$$

$$p_0 = \frac{n^2 I_0}{r^2}, p_1 = \frac{n^2}{r^2}(b_0 + \frac{k_t k_b}{R_a}), p_2 = \frac{n k_t}{r R_a}, p_3 = (L_1^{sp})^2 + (L_2^{sp})^2 + (L_3^{sp})^2.$$

Since the derived NLPV model is a smooth nonlinear model, it may then be employed to design model-based controllers for switch wheeled OMRs. In addition, to implement this modeling approach in practice, it only requires real-time measurement of the wheel rotation angle or the absolute wheel angular position. This is can be realized by various encoders, such as optical encoder or absolute encoder. Note that, the encoders should be well installed to detect the exact switching time.

Moreover, the bounded differential of L_i^{sp} , i.e., $\dot{L}_i^{sp}(t)$, is usually required in the control of NLPV system [55]. It can be seen from (3.5) that the $\dot{L}_i^{sp}(t)$ is bounded. It is worth pointing out that all of the wheel switching cases, under either switching conditions (i) or (ii), are included in the designed spline L_i^{sp} . Note that the above approach is not restricted to the designed spline curves.

The above approach is not restricted to the designed spline curves. The discontinuous contact radius can be approximated by various continuous curves, such as polynomial curves and other spline curves. These curves can be derived based on the same idea presented above. That is, the ϕ_{i0}^{in} and ϕ_{i0}^{out} must be selected as variables in the curve expressions.

3.1.3 Simulation Verification

In this subsection, open-loop simulations are conducted to verify the effectiveness of the average dynamic model and the NLPV dynamic model in predicting the behavior of the switched nonlinear dynamic model. The spline-based NLPV model derived above is used in the simulations.

The parameter values used in the simulations are as follows: $m = 35$ kg, $I_v = 1.35$ kg \cdot m², $r = 0.06$ m, $D_{in} = 0.147$ m, $D_{out} = 0.236$ m, $I_0 = 3.15 \times 10^{-5}$ kg \cdot m², $k_t = 0.0292$ N \cdot m/A, $k_b = 328$ rpm/V, $n = 186$, $b_0 = 1.5 \times 10^{-4}$ Nms/rad, $R_a = 0.61$ Ω . λ is set as 0.1. The initial wheel angular position is set as $\begin{bmatrix} \phi_1 & \phi_2 & \phi_3 \end{bmatrix}^T = \begin{bmatrix} 5.44 \text{ (rad)} & 5.28 \text{ (rad)} & 4.12 \text{ (rad)} \end{bmatrix}^T$. The following simulations were implemented in Matlab/Simulink.

In typical model validations, the responses of different models are compared under the same control input [56, 57]. Thereby, the three models, namely, the switched nonlinear dynamic model, average dynamic model and NLPV dynamic model, were supplied with same control input. To show the effectiveness of the spline L_i^{sp} in adaptively approaching the non-periodic switching of the contact radius, the following time-varying control input $u(t) = \begin{bmatrix} u_1(t) & u_2(t) & u_3(t) \end{bmatrix}^T$ (V) is selected:

$$\begin{aligned} u_1(t) &= 10 \sin(0.1t), \\ u_2(t) &= 10 \sin(0.1t), \\ u_3(t) &= 20 \cos(0.1t). \end{aligned} \tag{3.7}$$

Figure 3.5 - Figure 3.7 show the simulation results. It is observed from Figure 3.5 (a) that, the designed spline contact radius is able to adaptively approach the real discontinuous

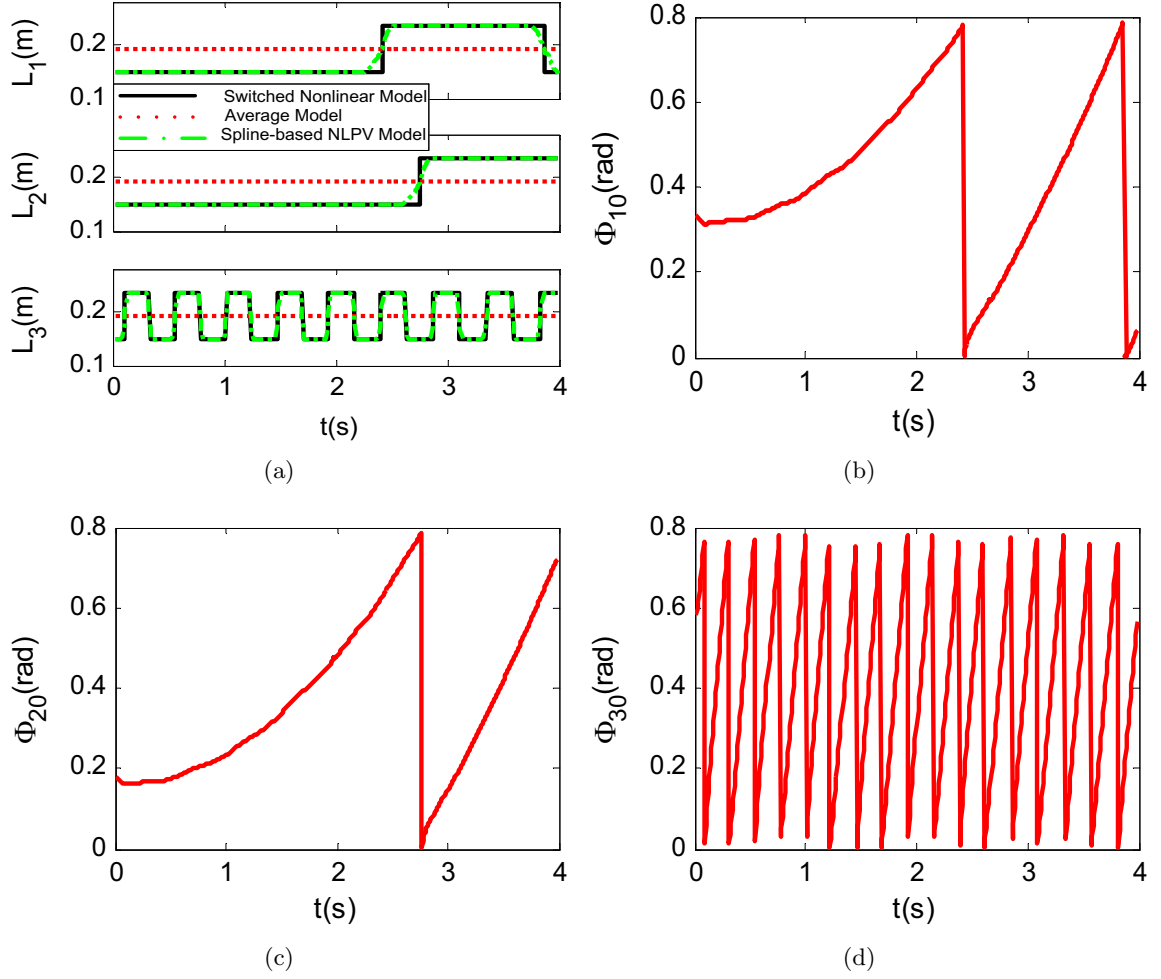


Figure 3.5: Open-loop simulation results: (a) Real contact radius L_i , average contact radius L_a and spline contact radius L_i^{sp} . (b) Variable ϕ_{10} (see (3.4)). (c) Variable ϕ_{20} (see (3.4)). (d) Variable ϕ_{30} (see (3.4)).

contact radius even though the discontinuous contact radius is non-periodic. The wheel rotation angles that results in the switching of the contact radius are shown in Figure 3.5 (b) - (d). Note that all of the three wheels turn in one direction in this simulation. Therefore, according to switching condition (i), the wheel rotation angle resulting in switching of the contact radius is $\frac{\pi}{4}$, which is clearly shown in Figure 3.5 (b) - (d).

The robot posture and velocity responses generated by the three models are shown in Figure 3.6 - Figure 3.7. As seen in Figure 3.6 - Figure 3.7, the responses of the average dynamic model obviously have large estimation errors against the responses produced by

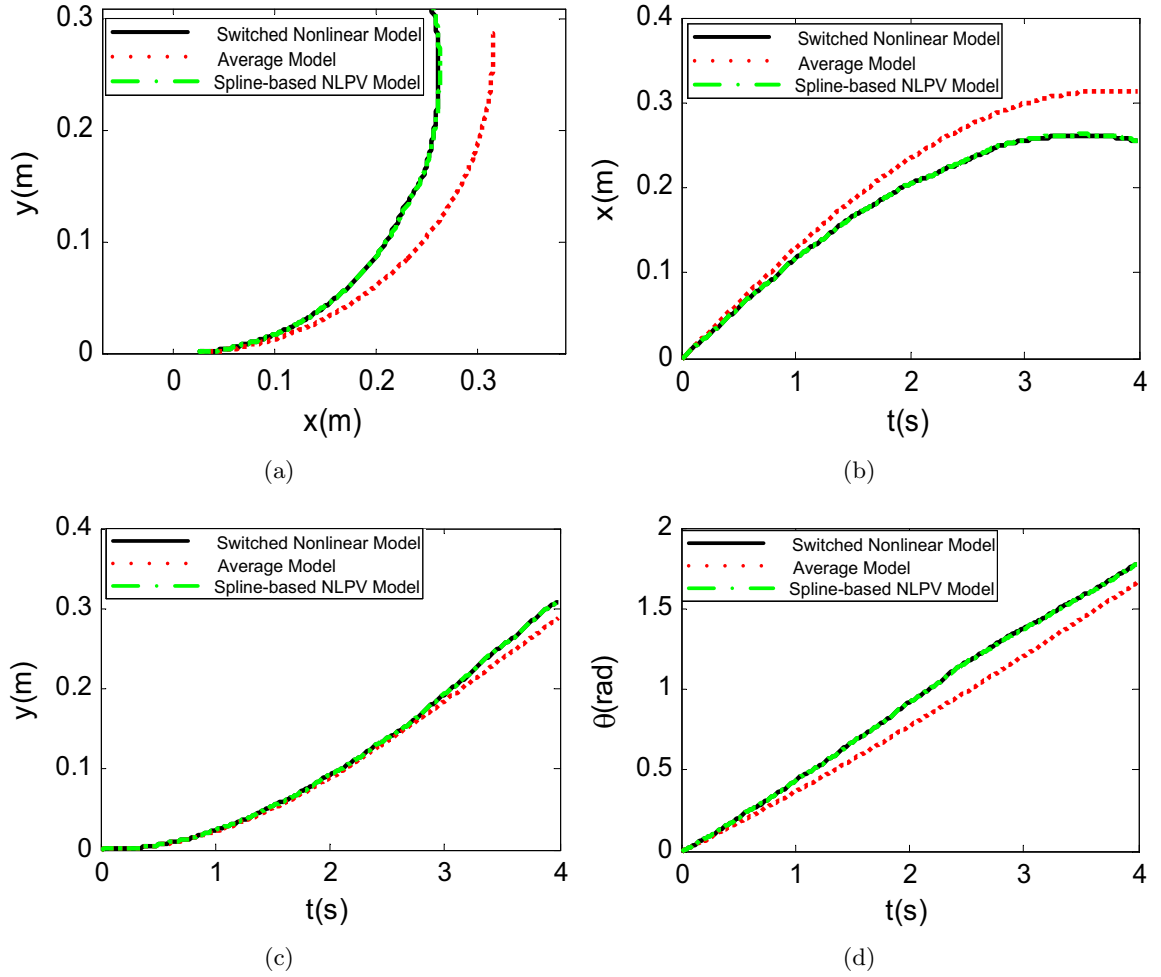


Figure 3.6: Open-loop simulation results: (a) Robot trajectory in the xy-plane. (b) Robot position in x component. (c) Robot position in y component. (d) Robot orientation θ .

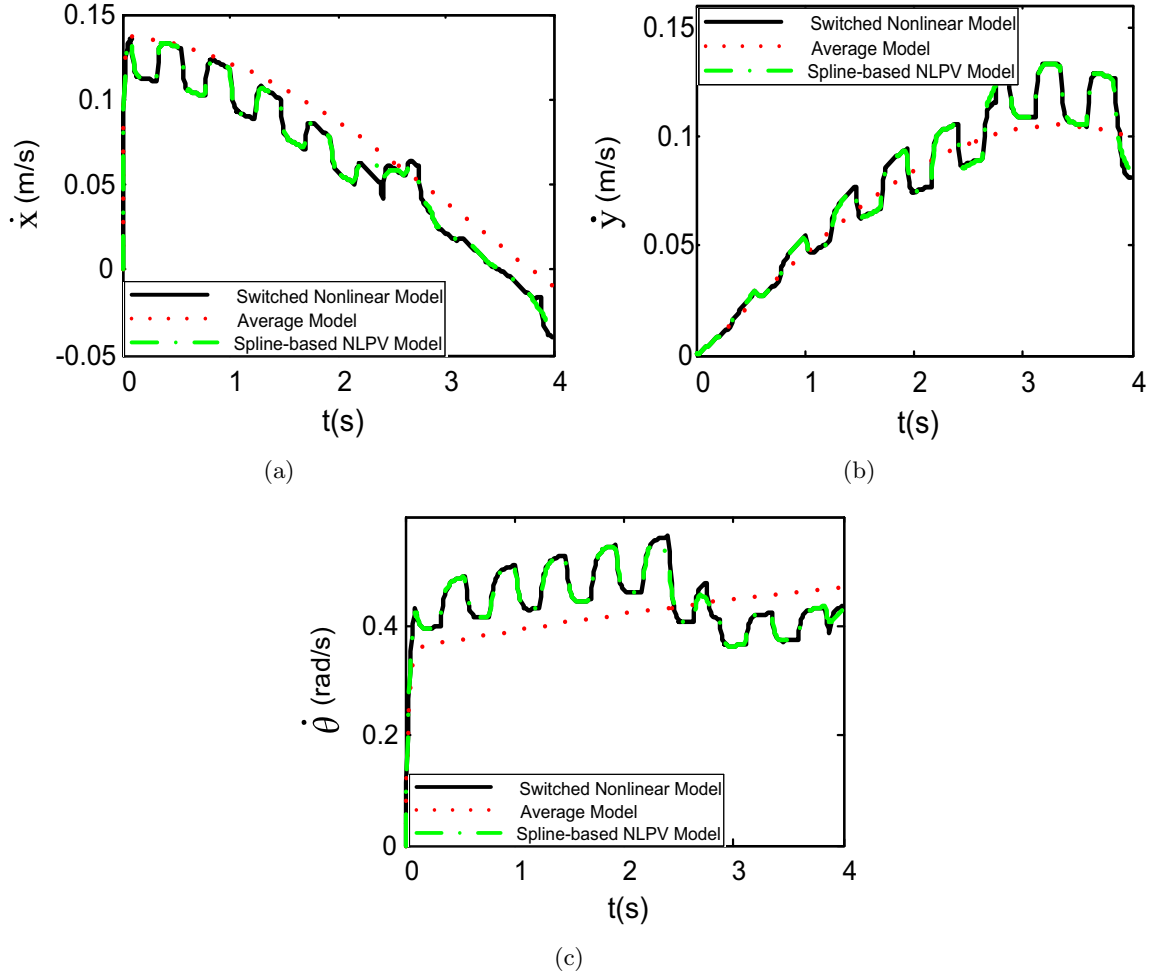


Figure 3.7: Open-loop simulation results: (a) Robot velocity in x component. (b) Robot velocity in y component. (c) Robot rotational velocity $\dot{\theta}$.

the switched nonlinear dynamic model. For example, as shown in Figure 3.6, the responses generated by the average model have a large deviation against the responses of the switched nonlinear dynamic model, while responses of the NLPV model have a good agreement with those of the switched nonlinear dynamic model. It should be noted that our robot prototype has a large value of γ , i.e., $\gamma = 0.61$. Therefore, as already analyzed before, the robot configuration does not meet the requirement in (3.3), and thus the average dynamic modeling approach produces large modeling errors. However, even though the robot prototype has large value of γ , it is seen that the responses of the proposed NLPV model are in excellent agreement with the responses produced by the switched nonlinear dynamic model.

To quantitatively compare the average dynamic model and NLPV dynamic model, the performances are quantified by calculating \mathcal{L}_2 norm of the response errors [56]. We define \mathcal{L}_2 norm of the posture and velocity response errors between average dynamic model and switched nonlinear dynamic model as follows:

$$E_{pos}^{av} = \sqrt{\int \left[(x - x_{av})^2 + (y - y_{av})^2 + (\theta - \theta_{av})^2 \right] dt},$$

$$E_{vel}^{av} = \sqrt{\int \left[(\dot{x} - \dot{x}_{av})^2 + (\dot{y} - \dot{y}_{av})^2 + (\dot{\theta} - \dot{\theta}_{av})^2 \right] dt}.$$

\mathcal{L}_2 norm of the posture and velocity response errors between NLPV dynamic model and switched nonlinear dynamic model is defined as follows:

$$E_{pos}^{sp} = \sqrt{\int \left[(x - x_{sp})^2 + (y - y_{sp})^2 + (\theta - \theta_{sp})^2 \right] dt},$$

$$E_{vel}^{sp} = \sqrt{\int \left[(\dot{x} - \dot{x}_{sp})^2 + (\dot{y} - \dot{y}_{sp})^2 + (\dot{\theta} - \dot{\theta}_{sp})^2 \right] dt}.$$

It should be mentioned that the \mathcal{L}_2 norm defined in this paper has no unit. The purpose of employing \mathcal{L}_2 norm is to indicate the performance differences between the two models above. The lower values indicate a closer agreement between average dynamic model or

NLPV dynamic model and switched nonlinear dynamic model. The calculated results of the simulations above are as follows: $E_{pos}^{av} = 46.20$, $E_{pos}^{sp} = 0.63$, $E_{vel}^{av} = 28.01$, $E_{vel}^{sp} = 1.37$. It can be seen that \mathcal{L}_2 norm of the posture and velocity errors produced by the spline-based NLPV model is much less than that produced by the average dynamic model. This means that the responses produced by the spline-based NLPV model have a much better agreement with those produced by the switched nonlinear dynamic model. In other words, assuming that the switched nonlinear dynamic model is the ideal model of the robot prototype, the NLPV dynamic model is more accurate than the average dynamic model in modeling the prototype.

As discussed before, the NLPV modeling approach is able to produce much less modeling errors, even for the robot with large γ , while in this case the average modeling approach produces large modeling errors. As a result, we conducted simulations by choosing different value of γ to compare the performance of average dynamic model and NLPV dynamic model. In the following simulations, the value of D_{in} is kept constant and is set as 0.147 m . We change the value of $(D_{out} - D_{in})$, which in turn changes the value of γ (see (3.3)). Simulation time was set as 4 s and the same control input (3.7) is used. Simulation results are shown in Table 3.1. It can be seen that, the NLPV model produces much smaller \mathcal{L}_2 norm value than average model, even for the robot with very large γ . As a result, the proposed NLPV model demonstrates definitely much better performance in approaching the responses produced by the switched nonlinear dynamic model, compared with the average dynamic model even though for the robot with large γ .

It should be emphasized that the accuracy of the proposed average dynamic model and NLPV dynamic model depends on the modeling accuracy of the switched nonlinear dynamic model (2.16). This is because both the average dynamic model and NLPV dynamic model are derived from the switched nonlinear dynamic model (2.16). The unmodeled dynamics, such as the Viscous and Coulomb frictions, dead-zone, parameter uncertainties, etc, are neglected in the switched nonlinear dynamic model (2.16). Therefore, these modeling errors are the same for both average dynamic model and NLPV dynamic model. The above

Table 3.1: Simulation results with different γ

γ	0.54	0.68	0.82	0.95	1.1
E_{pos}^{av}	42.49	50.83	58.53	64.49	70.58
E_{pos}^{sp}	0.78	1.03	1.49	1.32	0.99
E_{vel}^{av}	25.97	30.31	34.34	37.26	40.21
E_{vel}^{sp}	1.27	1.55	1.75	1.76	1.90
γ	1.22	1.36	1.5	1.63	1.77
E_{pos}^{av}	75.80	80.58	85.76	89.35	93.98
E_{pos}^{sp}	1.59	1.36	1.88	1.47	2.23
E_{vel}^{av}	42.67	45.02	47.28	48.93	51.01
E_{vel}^{sp}	2.18	2.23	2.33	2.14	2.51

simulation results only demonstrate that the modeling errors resulting from the switching of the contact radius in NLPV dynamic model are smaller than the average dynamic model.

The average dynamic model is easy to be obtained and the model is smooth nonlinear. It also does not require detection of switching of the contact radius and thus the encoders measuring the wheel angular position are not needed. However, the average dynamic modeling approach leads to large modeling error when (3.3) is not satisfied. On the other hand, the NLPV modeling approach produces much smaller modeling errors, even though for the robot with large γ . However, one price is that detection of switching of the contact radius is needed; that is, the encoders measuring the wheel angular position are indispensable.

In addition, both the modeling approaches can also be applied to other switch wheeled OMRs. Special attention that should be paid to the NLPV dynamic modeling approach is that, for different wheel mechanisms, switching conditions will also be different. For example, for the Longitudinal orthogonal-wheel [6], switching condition (i) should be that the wheel turned angle resulting in switching of the contact radius is $\frac{\pi}{2}$, rather than $\frac{\pi}{4}$.

3.2 RAC Design and Verification

In this section, RAC is employed to design controllers for the robot prototype based on the average dynamic model and NLPV dynamic model, respectively. Then both controllers are verified and compared through simulations. We only conduct experiments for average dynamic model based RAC, since it is simple to be implemented in practice. For our robot prototype, some difficulties exist in implementing the experiments of NLPV dynamic model based RAC. For example, the NLPV modeling approach requires exact switching time while this cannot be achieved for our robot prototype. Finally, discussions on the two model based control systems are presented.

The tracking control problem is formulated as follows: given a reference trajectory $\mathbf{q}_d(t) = \begin{bmatrix} x_d & y_d & \theta_d \end{bmatrix}^T$, which is bounded and twice continuously differentiable, find a control input $\mathbf{u}(t)$ such that the responses of the robot, $\mathbf{q}(t) = \begin{bmatrix} x & y & \theta \end{bmatrix}^T$, converges to $\mathbf{q}_d(t) = \begin{bmatrix} x_d & y_d & \theta_d \end{bmatrix}^T$ for any initial condition.

3.2.1 RAC Design

Define the tracking error as $\mathbf{e} = \mathbf{q} - \mathbf{q}_d$. The average dynamic model based RAC is given as follows:

$$\mathbf{u}_{av} = \mathbf{B}_{av}^{-1} \mathbf{M}_{av} (\ddot{\mathbf{q}}_d - \mathbf{K}_d \dot{\mathbf{e}} - \mathbf{K}_p \mathbf{e}) + \mathbf{B}_{av}^{-1} \mathbf{C}_{av} \dot{\mathbf{q}}, \quad (3.8)$$

where $\mathbf{M}_{av} = \mathbf{M}_{2av}^W \mathbf{R}^T$, $\mathbf{C}_{av} = \mathbf{C}_{2av}^W \mathbf{R}^T - \mathbf{M}_{2av}^W \mathbf{R}^T \dot{\mathbf{R}}_M^W \mathbf{R}^T$, \mathbf{M}_{2av} and \mathbf{B}_{av} are the same with those in (3.1). \mathbf{C}_{2av} is given as:

$$\mathbf{C}_{2av} = \begin{bmatrix} \frac{3}{2}\beta_1 & -m\dot{\theta} & 0 \\ m\dot{\theta} & \frac{3}{2}\beta_1 & 0 \\ 0 & 0 & 3\beta_1 L_a^2 \end{bmatrix},$$

and β_0 , β_1 and β_2 are the same as those in (2.15). Note that in \mathbf{C}_{2av} , $\dot{\theta}$ has been used instead of $\dot{\theta}_{av}$. Besides, $^W \mathbf{R}$ has been used instead of $^W \mathbf{R}_{av}$. This is because in simulations or experiments, the real robot position and velocity are used in the control design.

The NLPV dynamic model based RAC is given as follows:

$$\mathbf{u}_{NLPV} = \mathbf{B}_{sp}^{-1} \mathbf{M}_{sp} (\ddot{\mathbf{q}}_d - \mathbf{K}_d \dot{\mathbf{e}} - \mathbf{K}_p \mathbf{e}) + \mathbf{B}_{sp}^{-1} \mathbf{C}_{sp} \dot{\mathbf{q}}, \quad (3.9)$$

where $\mathbf{M}^{sp} = \mathbf{M}_{1M}^{spW} \mathbf{R}^T$, $\mathbf{C}^{sp} = \mathbf{C}_{1M}^{spW} \mathbf{R}^T - \mathbf{C}_{1M}^{spW} \mathbf{R}_{1M}^{TW} \dot{\mathbf{R}}_M^W \mathbf{R}^T$, $\mathbf{B}^{sp} = \mathbf{B}_1^{sp}$. \mathbf{M}_1^{sp} and \mathbf{B}_1^{sp} are the same with those in (3.6).

$$\mathbf{C}_1^{sp} = \begin{bmatrix} \frac{3}{2}p_1 & -m\dot{\theta} & p_1(-\frac{L_1^{sp}+L_2^{sp}-2L_3^{sp}}{2}) \\ m\dot{\theta} & \frac{3}{2}p_1 & \frac{\sqrt{3}}{2}p_1(L_1^{sp}-L_2^{sp}) \\ p_1(-\frac{L_1^{sp}+L_2^{sp}-2L_3^{sp}}{2}) & \frac{\sqrt{3}}{2}p_1(L_1^{sp}-L_2^{sp}) & p_1p_3 \end{bmatrix},$$

$p_0 = \frac{n^2 I_0}{r^2}$, $p_1 = \frac{n^2}{r^2}(b_0 + \frac{k_t k_b}{R_a})$, $p_2 = \frac{nk_t}{rR_a}$, $p_3 = (L_1^{sp})^2 + (L_2^{sp})^2 + (L_3^{sp})^2$. Also note that in \mathbf{C}_1^{sp} , $\dot{\theta}_{sp}$ has been changed with $\dot{\theta}$, and ${}^W_M \mathbf{R}$ has been used instead of ${}^W_M \mathbf{R}_{sp}$. L_i^{sp} is derived from (3.5).

3.2.2 Simulation Verification

In this part, simulations are implemented in Matlab/Simulink, to compare the two model based controllers (3.8) and (3.9). Three typical trajectories in trajectory tracking control study of mobile robot are employed, i.e., circle trajectory, square trajectory and lemniscate trajectory. Note that the selected trajectories are ones that the robot can achieve without actuator saturation. In other words, further increase in the translational or rotational speed will cause the actuator saturation problem. Since the path planning problem is out of the scope of this paper, the robot initial posture of the three tests is set on the initial point of robot trajectory, to avoid actuator saturation.

The controller gains \mathbf{K}_p and \mathbf{K}_d for both controllers are set as the same, and are as follows:

$$\mathbf{K}_p = \begin{bmatrix} 16 & & \\ & 16 & \\ & & 16 \end{bmatrix}, \quad \mathbf{K}_d = \begin{bmatrix} 40 & & \\ & 40 & \\ & & 40 \end{bmatrix}. \quad (3.10)$$

Simulation 1: the robot is commanded to track a circle of 0.8 m radius within 30 s, i.e., $x_d = 0.8 \cos(\frac{\pi}{15}t)$ m; $y_d = 0.8 \sin(\frac{\pi}{15}t)$ m. The robot initial posture is set as $\begin{bmatrix} 0.8 \text{ (m)} & 0 \text{ (m)} & 0 \text{ (rad)} \end{bmatrix}^T$. In the first 10 s, the robot performs translational motion without rotation, i.e., $\theta_d = 0$ rad. After 10 s, the desired robot orientation angle is set as $\theta_d = 0.35(t - 10)$ rad. Simulation results are shown in Figure 3.8 - Figure 3.9.

In the previous part, it is known that, compared with the switched nonlinear dynamic model, the modeling errors of the average dynamic model and NLPV dynamic model only result from the parameter uncertainties in \mathbf{L} . It is also known that the modeling errors of average dynamic model is larger than the NLPV dynamic model. However, as shown in Figure 3.8 (a)- (c), the performances of both controllers in the first 10 s are almost the same. After 10 s, the tracking errors of average dynamic model based RAC are much larger than NLPV dynamic model based RAC.

As discussed in Chapter 2, the switch wheeled OMRs are linear systems when the robot moves with only translational motion. That is, the switching of the contact radius does not influence the robot dynamics when the robot performs only translational motion. Therefore, in the first 10 s, compared with the switched nonlinear dynamic model, no modeling errors are introduced into the average dynamic model and the NLPV dynamic model. Therefore, the control performances are ideal and the same for both controllers in the first 10 s. However, after 10 s, the robot dynamic system turns to a switched nonlinear system because of the switching of the contact radius. In this case, modeling errors are introduced to average and NLPV dynamic models due to parameter errors in the contact radius. It is well known that the control performances of RAC depend on the modeling accuracy. Since the modeling errors of average dynamic model are larger than the NLPV

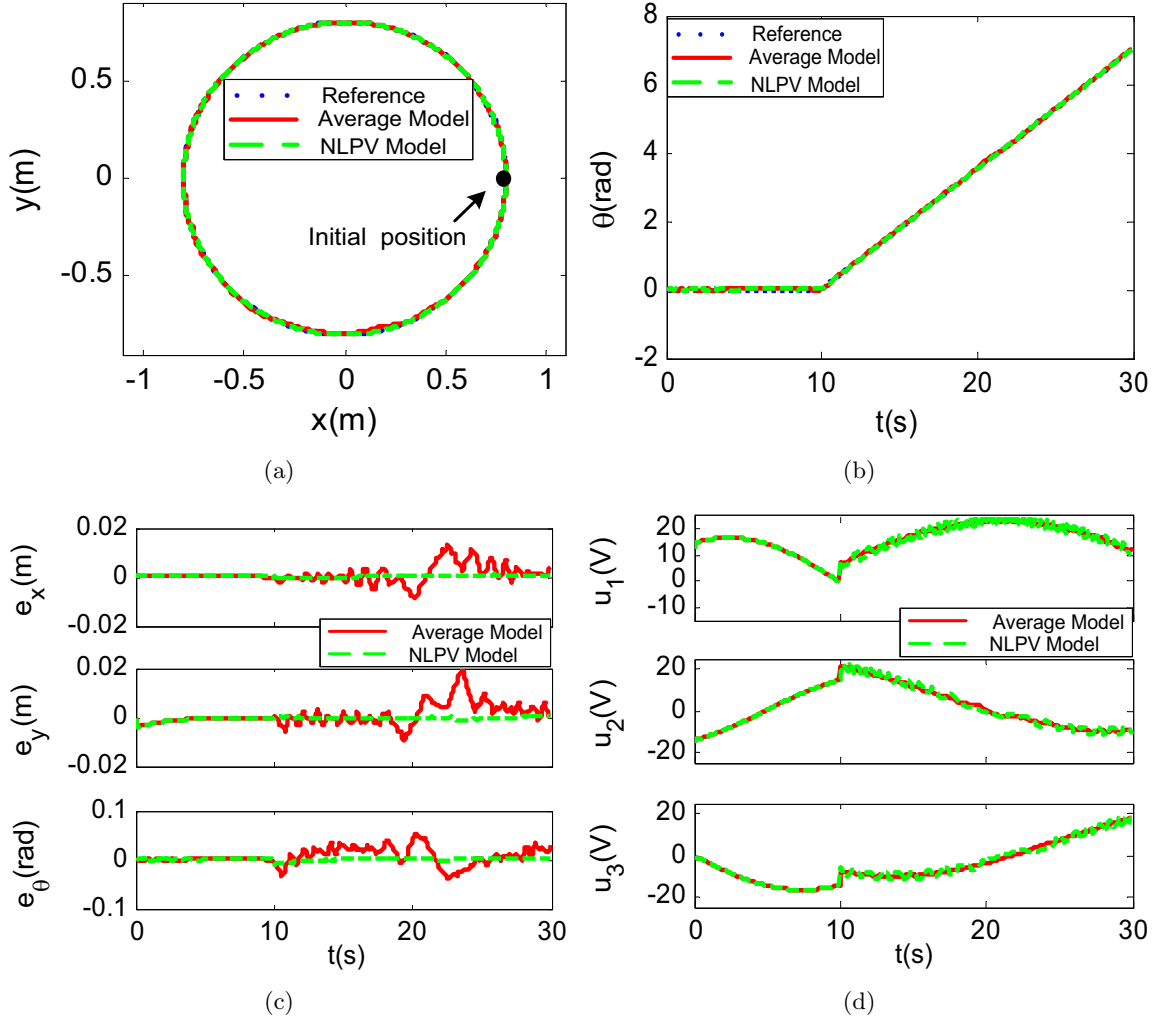


Figure 3.8: Simulation results of average dynamic model based RAC and NLPV dynamic model based RAC (circle trajectory): (a) Reference trajectory and responses in the xy -plane. (b) Reference trajectory and responses in the orientation direction. (c) Tracking errors. (d) Control input $\mathbf{u}(t)$.

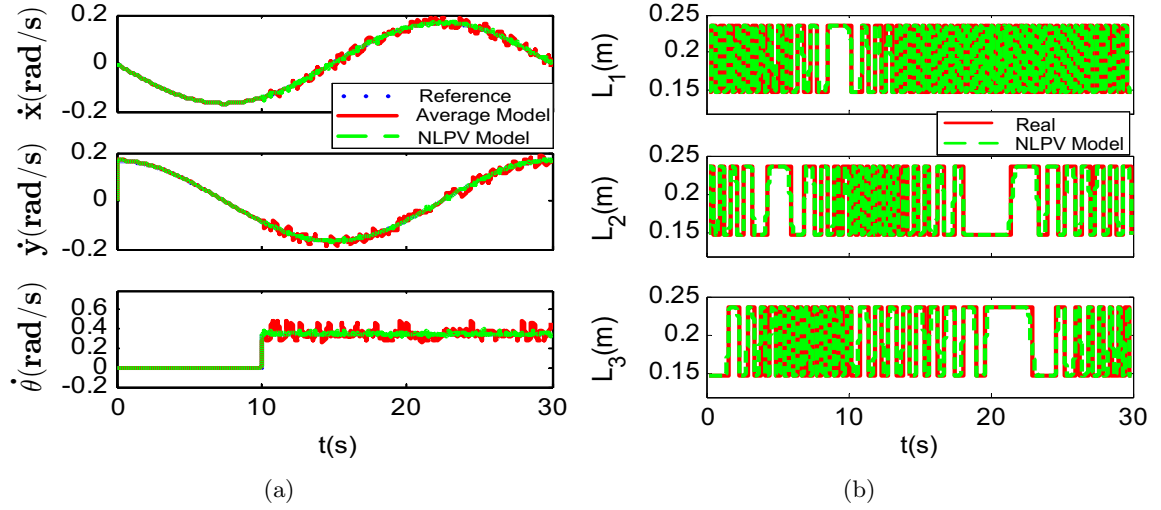


Figure 3.9: Simulation results of average dynamic model based RAC and NLPV dynamic model based RAC (circle trajectory): (a) Reference velocity and responses. (b) Contact radius of NLPV dynamic model based RAC and the adaptive approaching curves.

dynamic model, the control performances of average dynamic model based RAC are thus worse than the NLPV dynamic model based RAC.

Figure 3.8 (d) shows the control inputs of both control systems. It is shown that the control input of the average dynamic model based RAC is smooth, since the switching effects are neglected in the average dynamic model and thus cannot be compensated in the control system. On the other hand, the switching of the discontinuous contact radius is approached by the adaptive continuous curves in the derived NLPV dynamic model. The switching of the contact radius can be partly compensated by the controller. As a result, fluctuations in the control inputs appear when the robot moves with rotation. The effects on compensation of the switching contact radius are also shown in Figure 3.9 (a). Since the NLPV dynamic model based control can partly compensate the switching effects, the fluctuations in the robot velocity are reduced compared with those of average dynamic model based RAC.

The switching of the contact radius of NLPV dynamic model based RAC is shown in Figure 3.9 (b). It can be seen that even though the switching of the contact radius is non-

periodic, the designed continuous curves can adaptively approach the discontinuous contact radius of the robot prototype.

Table 3.2: IAE of average dynamic model based and NLPV dynamic model based RAC

Trajectory	Circle		Square		Lemniscate	
IAE	$IAE_{xy}(\text{m})$	$IAE_{\theta}(\text{rad})$	$IAE_{xy}(\text{m})$	$IAE_{\theta}(\text{rad})$	$IAE_{xy}(\text{m})$	$IAE_{\theta}(\text{rad})$
Average	0.150	0.370	0.200	0.275	0.226	0.352
NLPV	0.028	0.035	0.066	0.050	0.036	0.077

Simulation 2: in this test, the robot is commanded to track a square trajectory (see Figure 3.10). The robot initial posture is set as $\begin{bmatrix} 0(\text{m}) & 0(\text{m}) & 0(\text{rad}) \end{bmatrix}^T$. The desired speed of translational motion is set as 0.15 m/s. On the side of AB and CD, the robot orientation is fixed. On the side of BC, the reference orientation angle is $\theta_d = \frac{\pi}{15}(t-10)$ rad. On the side of DA, the reference orientation angle is a sinusoidal curve: $\theta_d = \frac{\pi}{6} \sin(\frac{\pi}{5}(t-30))$ rad. Simulation results are shown in Figure 3.10.

Simulation 3: in this test, the reference lemniscate trajectory is set as: $x_d = 0.5 \cos(\frac{\pi}{20}t)$ m; $y_d = 0.5 \sin(\frac{\pi}{10}t)$ m. The robot initial posture is set as $\begin{bmatrix} 0.5(\text{m}) & 0(\text{m}) & 0(\text{rad}) \end{bmatrix}^T$. In the first 20 s, the robot orientation is fixed, i.e., $\theta_d = 0$ rad. After 20 s, the desired orientation angle is $\theta_d = \frac{\pi}{10}(t-20)$ rad. Simulation results are shown in Figure 3.11.

We use the integral absolute error (IAE) as the evaluation criterion of control performance. The definition is as follows: $IAE_{xy} = \int_0^t (|e_x| + |e_y|)dt$; $IAE_{\theta} = \int_0^t |e_{\theta}|dt$. The IAE of average dynamic model based and NLPV dynamic model based RAC is shown in Table 3.2. It is seen from simulations of the above three trajectories that IAE of NLPV dynamic model based RAC is much smaller than that of average dynamic model based RAC. Therefore, the NLPV dynamic model based RAC has demonstrated much better performances than the average dynamic model based RAC.

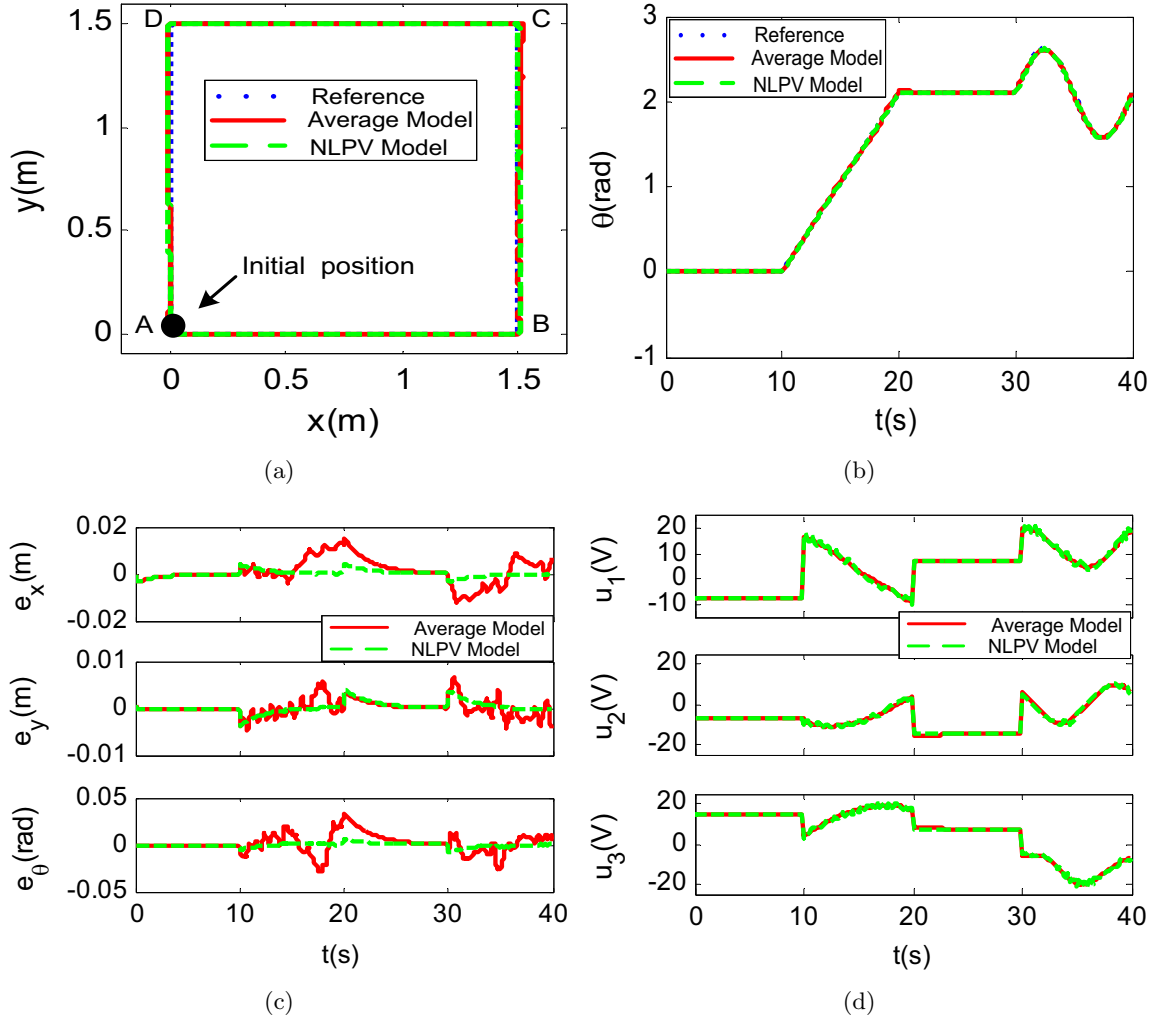


Figure 3.10: Simulation results of average dynamic model based RAC and NLPV dynamic model based RAC (square trajectory): (a) Reference trajectory and responses in the xy-plane. (b) Reference trajectory and responses in the orientation direction. (c) Tracking errors. (d) Control input $\mathbf{u}(t)$.

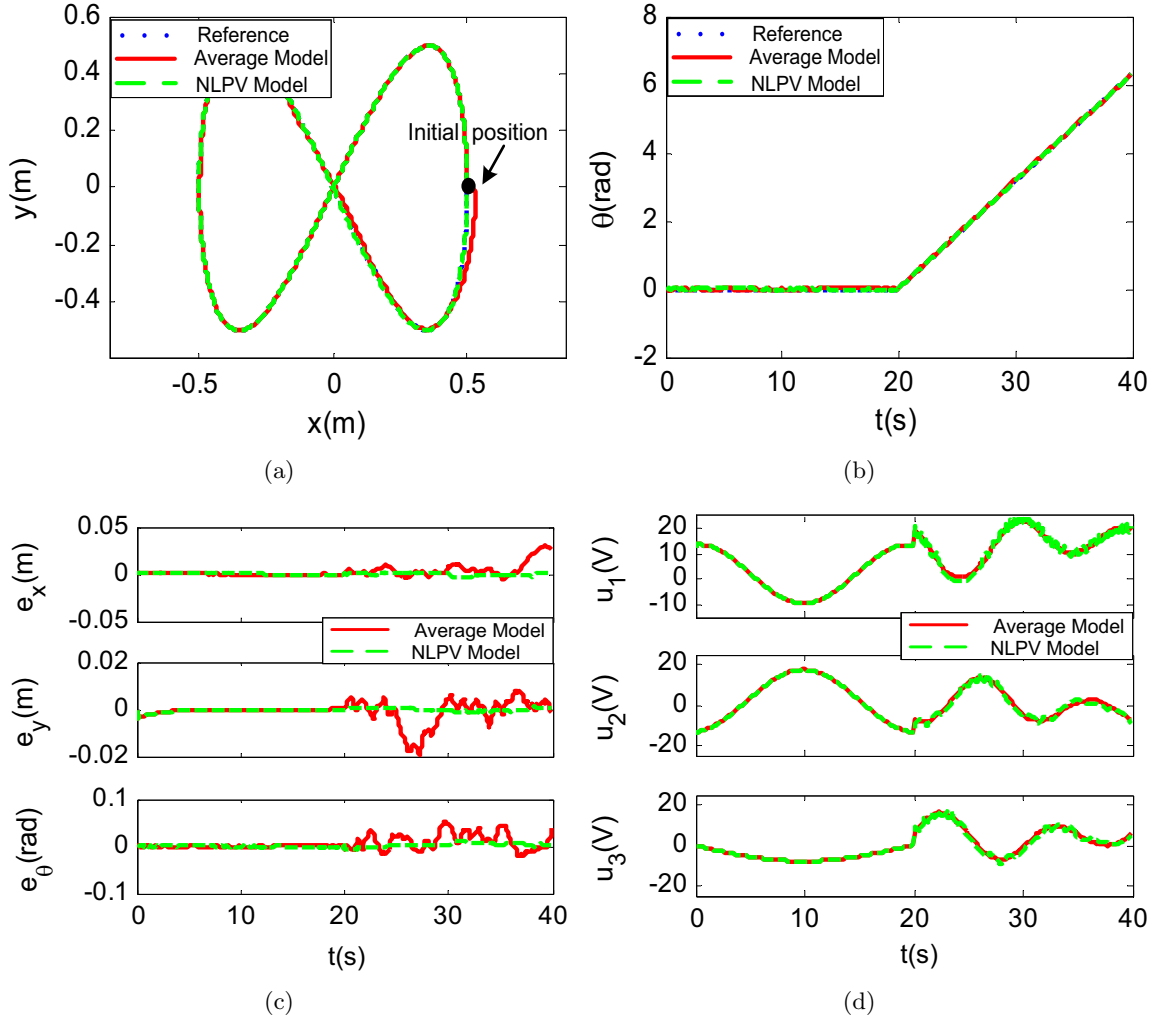


Figure 3.11: Simulation results of average dynamic model based RAC and NLPV dynamic model based RAC (lemniscate trajectory): (a) Reference trajectory and responses in the xy -plane. (b) Reference trajectory and responses in the orientation direction. (c) Tracking errors. (d) Control input $\mathbf{u}(t)$.

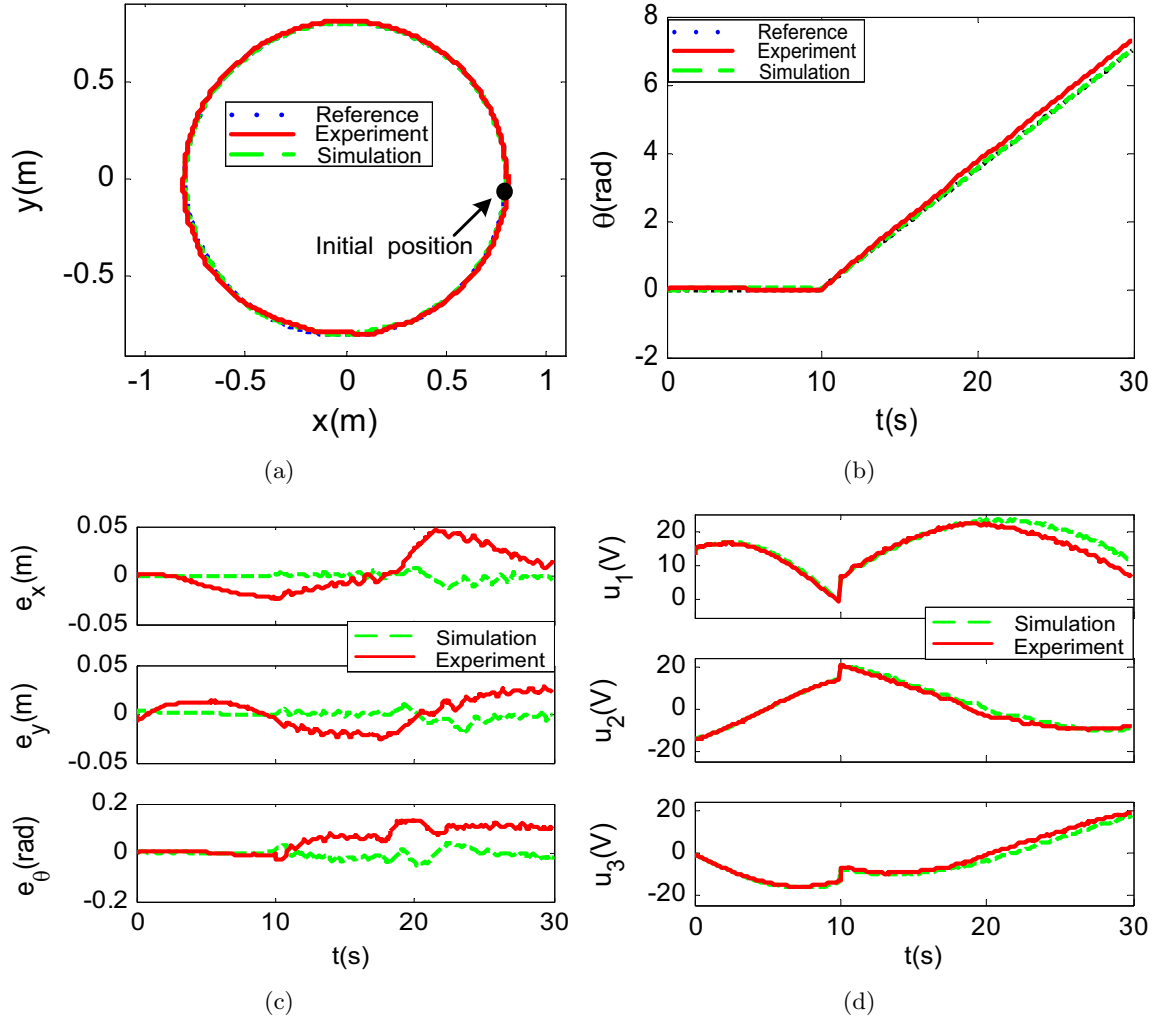


Figure 3.12: Simulation and experimental results of average dynamic model based RAC (circle trajectory): (a) Reference trajectory and responses in the xy-plane. (b) Reference trajectory and responses in the orientation direction. (c) Tracking errors. (d) Control input $\mathbf{u}(t)$.

Table 3.3: IAE of average dynamic model based RAC

Trajectory	Circle		Square		Leminisatate	
IAE	$IAE_{xy}(m)$	$IAE_t(rad)$	$IAE_{xy}(m)$	$IAE_t(rad)$	$IAE_{xy}(m)$	$IAE_t(rad)$
Simulation	0.150	0.370	0.200	0.275	0.226	0.352
Experiment	0.979	1.972	0.800	1.074	0.646	1.360

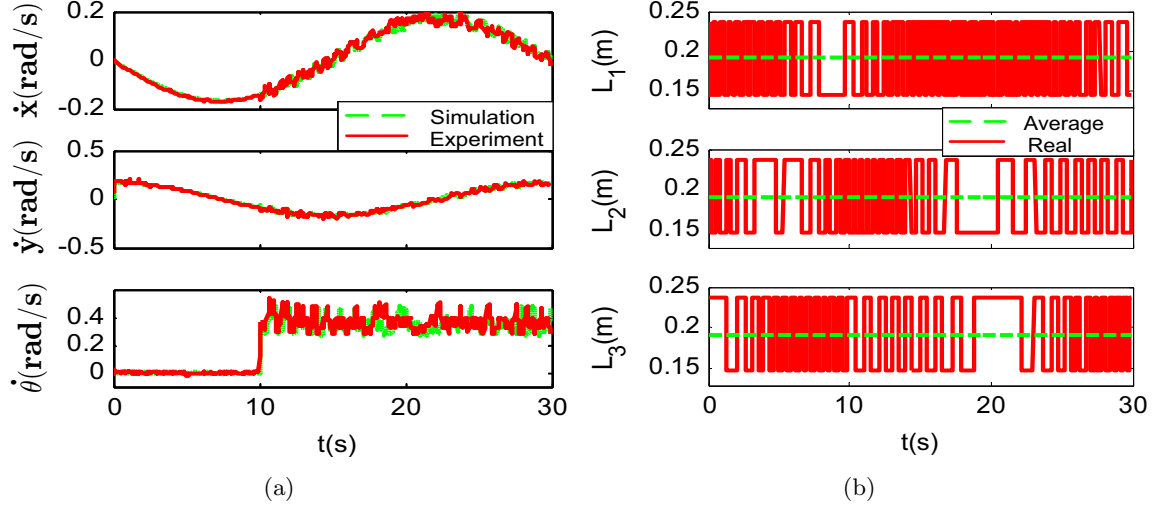


Figure 3.13: Simulation and experimental results of average dynamic model based RAC (circle trajectory): (a) Robot velocity. (b) Measured contact radius in the experiments and the average contact radius L_a in the average dynamic model.

3.2.3 Experiments of Average Dynamic Model based RAC

We have mentioned that the average dynamic model based RAC is easy to be implemented in practice. In this part, experiments of the above three trajectories are conducted to test the performances of average dynamic model based RAC. The experimental setup has been introduced in Chapter 2. The same controller gains used in the simulations are used in our experiments. Experimental results are shown in Figure 3.12 - Figure 3.15.

It is shown in Figure 3.12, 3.14 and 3.15 that the experimental results have large tracking errors than the simulation results. Therefore, the performances of average model based RAC in experiments are greatly reduced compared with simulation results. The IAE of simulation and experimental results is shown in Table 3.3. The experimental results in Table 3.3 are

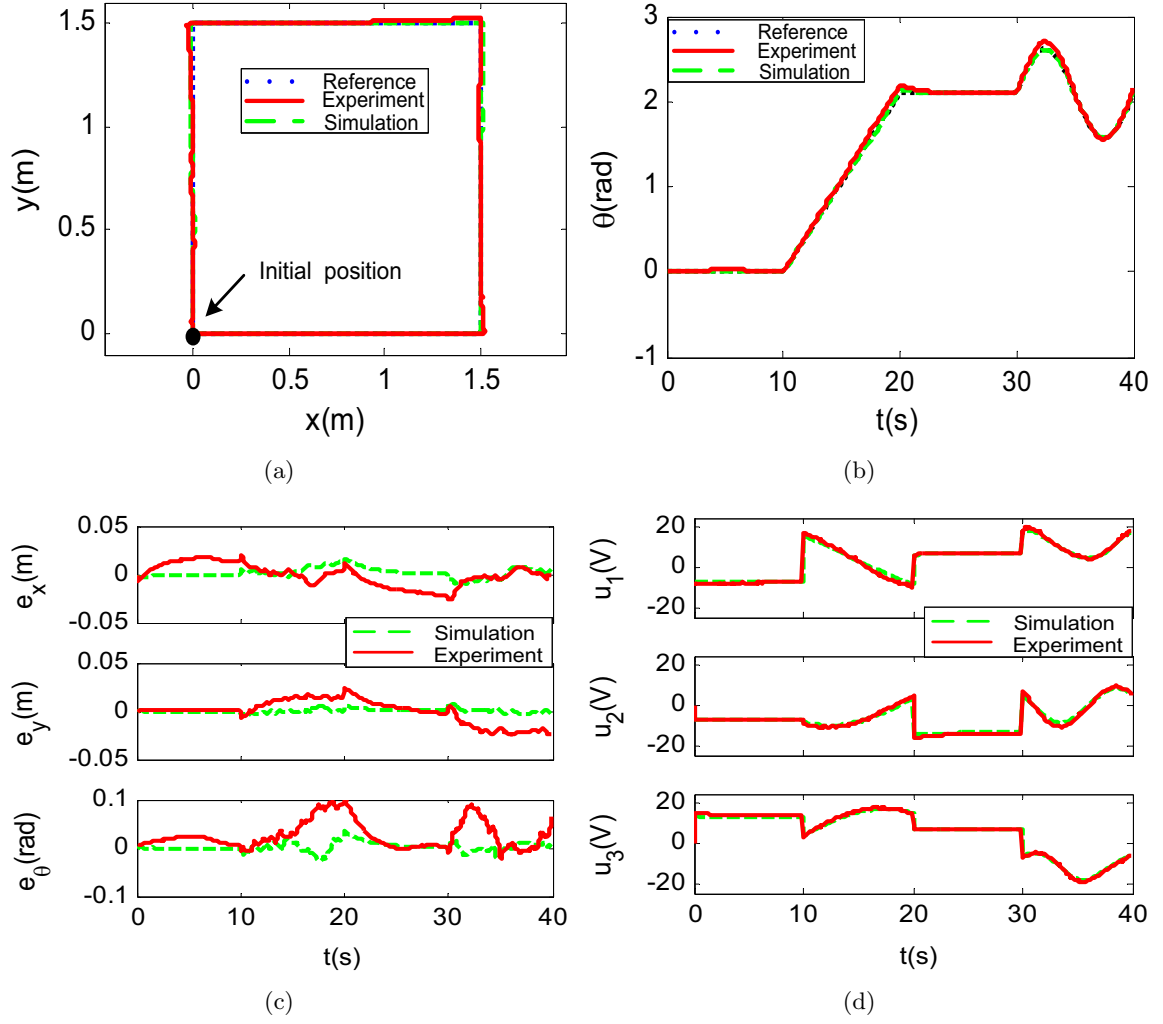


Figure 3.14: Simulation and experimental results of average dynamic model based RAC (square trajectory): (a) Reference trajectory and responses in the xy-plane. (b) Reference trajectory and responses in the orientation direction. (c) Tracking errors. (d) Control input $\mathbf{u}(t)$.

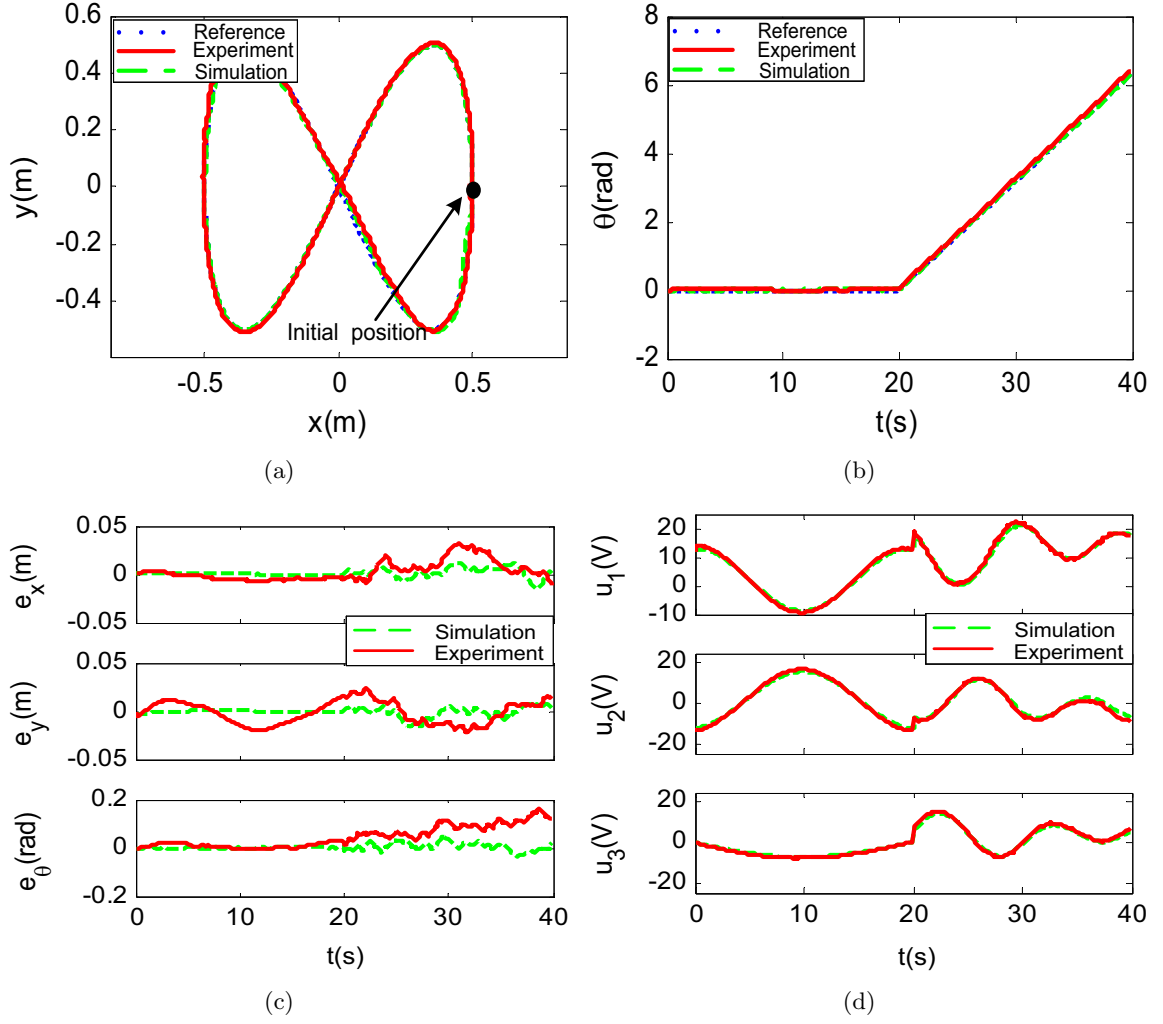


Figure 3.15: Simulation and experimental results of average dynamic model based RAC (lemniscate trajectory): (a) Reference trajectory and responses in the xy-plane. (b) Reference trajectory and responses in the orientation direction. (c) Tracking errors. (d) Control input $\mathbf{u}(t)$.

the average results of experiments with three times. The original data is shown in Appendix D.

The poor control performances are caused by modeling errors, which can be classified into three aspects: 1) unmodeled switching dynamics. In our previous analysis, it is known that our robot prototype is a switched nonlinear system and has eight smooth nonlinear dynamic subsystems. However, the average dynamic model is only a smooth dynamic model. Therefore, the switching dynamics is not modeled. 2) unmodeled forces. For example, Viscous and Coulomb frictions, dead-zone, etc, are not modeled in all the above three dynamic models. 3) parameter uncertainties. The robot dynamic parameters, such as, robot moment of inertia around the mass center I_v , combined Viscous friction coefficient of the motor, gear and wheel shaft b_0 , are not accurately estimated and thus have parameter errors.

It can be seen from Figure 3.13 (a) that, similar to the simulation results, the robot velocity is smooth when the robot moves with only translational motion. Fluctuations are introduced when the robot moves with rotational motion. Therefore, the experimental results consistent with the simulation results as well as the dynamic model analysis. In addition, the switching signal of the robot prototype, i.e., contact radius \mathbf{L} , is show in Figure 3.13 (b). It is measured by the installed absolute encoders. Figure 3.13 (b) also shows the average contact radius L_a used in the average dynamic model. The parameter errors between the real contact radius and the average contact radius are shown clearly.

3.3 Summary

In this chapter, we have introduced two continuous dynamic models, i.e., average dynamic model and NLPV dynamic model, to facilitate the control design for the robot prototype. The average dynamic model is derived by using the average contact radius instead of the switching contact radius. The NLPV dynamic model is derived by using continuous curves to adaptively approach the switching of contact radius, which may be non-periodic. The

key point to achieve this is based on the two switching conditions. Simulation results have shown that the average dynamic model produces much larger modeling errors than NLPV dynamic model. However, the average dynamic model does not need exact switching signal and is simple in the practical implementation. The NLPV dynamic model needs the exact real time switching information to produce the continuous curves. Then RAC has been employed to design controllers based on the two continuous dynamic models. Experimental results of the average dynamic model based RAC have shown that the control performances are not good due to the modeling errors of the average dynamic model.

Chapter 4

Generalized Proportional Integral (GPI) Observer based Control

In Chapter 3, we have analyzed that the modeling errors of the average dynamic model (3.1) are resulted from the following three aspects: 1) unmodeled switching dynamics, 2) unmodeled forces, 3) parameter uncertainties. It is also shown in the experiments that good control performances of average dynamic model based RAC cannot be achieved. This motivates us to improve the performances of average dynamic model based control design by compensating the above modeling errors.

Generalized proportional integral (GPI) observer is a disturbance observer characterized by a high dimensional extension [58], and it thus has a good estimation performance of fast-varying disturbances, such as the complicated switching dynamics. In addition, GPI observers are most naturally applicable to the control of perturbed differentially flat nonlinear systems with measurable flat outputs [32]. GPI observer based control has been successfully applied in various practical applications [32, 59, 60, 61, 62, 63, 64], to name a few.

In this chapter, we present a trajectory tracking controller for the robot prototype based on GPI observer. The controller is designed and implemented based on the average

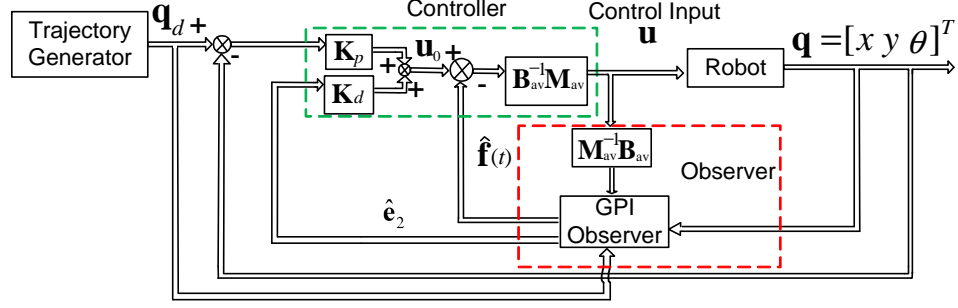


Figure 4.1: Block diagram of GPI observer based control system for the mobile robot.

dynamic model. The main idea is that all of the above modeling errors (such as switching dynamics, unmodeled forces, parameter uncertainties, etc.), as well as the input-output cross coupling effects are considered as an unknown time-varying perturbation input vector. The original switched nonlinear multi-input multi-output (MIMO) system is then approximately regarded as three decoupled single-input single-output (SISO) double integrators with an additive perturbation input vector. The perturbation input vector is then online estimated by the GPI observer, and compensated in the control signal. By GPI observer, the control design of the robot prototype is approximately reduced to the control design of the resulting three double integrators. Then simple proportional derivative (PD) control can be applied to the three double integrators. In addition, it is worth pointing out that only part of the robot model information is used in the control system design. Finally, both simulations and experiments are conducted to verify the effectiveness of the proposed control design. Comparisons with average dynamic model based RAC are also presented.

4.1 Control System Design

In this section, the GPI observer based trajectory tracking control design is presented. The designed control system is divided into two parts, i.e., controller design and GPI observer design. The block diagram of GPI observer based control system is shown in Figure 4.1.

4.1.1 Controller Design

In the switched nonlinear dynamic model (2.16), the parameter uncertainties, Viscous and Coulomb friction and other nonlinearities (e.g., dead-zone and backlash, etc.), are viewed as unmodeled dynamics and are not included. Therefore, the switched nonlinear dynamic model (2.16) considering these unmodeled robot dynamics can be rewritten as:

$$\ddot{\mathbf{q}} = -\mathbf{M}^{-1}(\mathbf{C}\dot{\mathbf{q}} + \mathbf{w}(t)) + (\mathbf{M}^{-1}\mathbf{B} - \mathbf{M}_{av}^{-1}\mathbf{B}_{av})\mathbf{u} + \mathbf{M}_{av}^{-1}\mathbf{B}_{av}\mathbf{u}, \quad (4.1)$$

where $\mathbf{w}(t)$ is a 3×1 unknown vector representing the unmodeled dynamics, such as the unmodeled friction forces, parameter uncertainties. \mathbf{M}_{av} and \mathbf{B}_{av} are the same as the average dynamic model (3.1), in which the switching effects are removed. The switching dynamics in $\mathbf{M}^{-1}\mathbf{B}$ is left in the term $(\mathbf{M}^{-1}\mathbf{B} - \mathbf{M}_{av}^{-1}\mathbf{B}_{av})$. Therefore, all of the complex switching dynamics are involved in the unknown term $-\mathbf{M}^{-1}(\mathbf{C}\dot{\mathbf{q}} + \mathbf{w}(t)) + (\mathbf{M}^{-1}\mathbf{B} - \mathbf{M}_{av}^{-1}\mathbf{B}_{av})\mathbf{u}$.

Considering the reference trajectory $\mathbf{q}_d = [x_d \ y_d \ \theta_d]^T$, the desired nominal system can be derived from (4.1) as:

$$\ddot{\mathbf{q}}_d = -\mathbf{M}_d^{-1}(\mathbf{C}_d\dot{\mathbf{q}}_d + \mathbf{w}_d(t)) + (\mathbf{M}_d^{-1}\mathbf{B} - \mathbf{M}_{avd}^{-1}\mathbf{B}_{av})\mathbf{u}_d + \mathbf{M}_{avd}^{-1}\mathbf{B}_{av}\mathbf{u}_d, \quad (4.2)$$

where $\mathbf{M}_d = \mathbf{M}(\mathbf{q}_d)$, $\mathbf{M}_{avd} = \mathbf{M}_{av}(\mathbf{q}_d)$, $\mathbf{C}_d = \mathbf{C}(\mathbf{q}_d, \dot{\mathbf{q}}_d)$, and $\mathbf{w}_d = \mathbf{w}(\mathbf{q}_d, \dot{\mathbf{q}}_d)$, \mathbf{u}_d is the nominal control input.

Defining tracking error $\mathbf{e} = \mathbf{q} - \mathbf{q}_d$, the tracking error dynamic equation becomes:

$$\begin{aligned} \ddot{\mathbf{e}} = \ddot{\mathbf{q}} - \ddot{\mathbf{q}}_d = & \mathbf{M}_{av}^{-1}\mathbf{B}_{av}\mathbf{u} - \mathbf{M}^{-1}(\mathbf{C}\dot{\mathbf{q}} + \mathbf{w}(t)) + (\mathbf{M}^{-1}\mathbf{B} - \mathbf{M}_{av}^{-1}\mathbf{B}_{av})\mathbf{u} - \mathbf{M}_{avd}^{-1}\mathbf{B}_{av}\mathbf{u}_d \\ & + \mathbf{M}_d^{-1}(\mathbf{C}_d\dot{\mathbf{q}}_d + \mathbf{w}_d(t)) - (\mathbf{M}_d^{-1}\mathbf{B} - \mathbf{M}_{avd}^{-1}\mathbf{B}_{av})\mathbf{u}_d. \end{aligned} \quad (4.3)$$

Defining

$$\begin{aligned} \mathbf{f} = & -\mathbf{M}^{-1}(\mathbf{C}\dot{\mathbf{q}} + \mathbf{w}(t)) + (\mathbf{M}^{-1}\mathbf{B} - \mathbf{M}_{av}^{-1}\mathbf{B}_{av})\mathbf{u} - \mathbf{M}_{av}^{-1}\mathbf{B}_{av}\mathbf{u}_d \\ & + \mathbf{M}_d^{-1}(\mathbf{C}_d\dot{\mathbf{q}}_d + \mathbf{w}_d(t)) - (\mathbf{M}_d^{-1}\mathbf{B} - \mathbf{M}_{avd}^{-1}\mathbf{B}_{av})\mathbf{u}_d, \end{aligned} \quad (4.4)$$

then (4.3) can be written as:

$$\ddot{\mathbf{e}} = \mathbf{f} + \mathbf{M}_{av}^{-1}\mathbf{B}_{av}\mathbf{u}, \quad (4.5)$$

where $\mathbf{f} = \begin{bmatrix} f_x(t) & f_y(t) & f_\theta(t) \end{bmatrix}^T$ is the unknown time-varying perturbation input vector in three channels (i.e., x , y and θ). It includes all of the complicated switching dynamics, unmodeled friction forces, parameter uncertainties, as well as the input-output cross coupling effects. Note that \mathbf{f} is a discontinuous vector since the switching dynamics are involved in it.

Defining $\hat{\mathbf{f}}$ as the estimation of \mathbf{f} , we apply the following control law:

$$\mathbf{u} = (\mathbf{M}_{av}^{-1} \mathbf{B}_{av})^{-1} (-\hat{\mathbf{f}} + \mathbf{u}_0). \quad (4.6)$$

Assuming that \mathbf{f} can be well estimated, the tracking error dynamics can be reduced into three decoupled double integrators in an approximate manner by combining (4.5) and (4.6):

$$\ddot{\mathbf{e}} \approx \mathbf{u}_0. \quad (4.7)$$

Since (4.7) is three decoupled double integrators, simple PD control can be applied to the three channels:

$$\begin{aligned} \mathbf{u}_0 &= -\mathbf{K}_p(\mathbf{q} - \mathbf{q}_d) - \mathbf{K}_d(\dot{\mathbf{q}} - \dot{\mathbf{q}}_d) \\ &= -\mathbf{K}_p \mathbf{e} - \mathbf{K}_d \dot{\mathbf{e}}. \end{aligned} \quad (4.8)$$

For the sake of simplicity, the same control gains are selected for the three channels in (4.8):

$$\mathbf{K}_p = \begin{bmatrix} \omega_c^2 & & \\ & \omega_c^2 & \\ & & \omega_c^2 \end{bmatrix}, \quad \mathbf{K}_d = \begin{bmatrix} 2\xi\omega_c & & \\ & 2\xi\omega_c & \\ & & 2\xi\omega_c \end{bmatrix},$$

where ω_c ($\omega_c > 0$) is a parameter to place the desired poles of the closed-loop dynamics, and $\xi > 0$ is a parameter representing the damping ratio. It is found in our experiments that with proper selection of parameter ξ , the oscillations in the system responses can be avoided. The selection of \mathbf{K}_p and \mathbf{K}_d is to make the characteristic polynomial of each channel Hurwitz; that is,

$$\chi(s) = s^2 + 2\xi\omega_c s + \omega_c^2. \quad (4.9)$$

Combining (4.6) and (4.8), the control law is:

$$\mathbf{u} = (\mathbf{M}_{av}^{-1} \mathbf{B}_{av})^{-1} (-\hat{\mathbf{f}} - \mathbf{K}_p \mathbf{e} - \mathbf{K}_d \dot{\mathbf{e}}). \quad (4.10)$$

4.1.2 GPI Observer Design

As mentioned above, the above system simplification is based on the assumption that \mathbf{f} can be well estimated. In this subsection, the GPI observer is constructed to estimate the time-varying perturbation input vector \mathbf{f} . Since a discontinuous function can be approximated by polynomials, splines, etc, it is therefore reasonable to assume that the discontinuous \mathbf{f} can be approximated by continuous functions. Thereby, the following assumption holds.

Assumption: The time-varying perturbation input vector \mathbf{f} can be approximated by a $(p - 1)$ -degree family of Taylor time-polynomial inputs and a residual term; that is,

$$\mathbf{f}(t) \approx \sum_{i=0}^{p-1} \alpha_i t^i + \mathbf{r}(t), \quad (4.11)$$

with $\alpha_i \in \mathbb{R}^3$ being constant coefficients, and the j th time derivatives of the residual term $\mathbf{r}(t)$, i.e., $\mathbf{r}^{(j)}(t) (j \geq p)$, being uniformly absolutely bounded.

Defining $\mathbf{e}_1 = \mathbf{e}$, $\mathbf{e}_2 = \dot{\mathbf{e}}$ and $\mathbf{f}_1 = \mathbf{f}$, the tracking error dynamics (4.5) can be written as:

$$\begin{aligned} \dot{\mathbf{e}}_1 &= \mathbf{e}_2, \\ \dot{\mathbf{e}}_2 &= \mathbf{M}_{av}^{-1} \mathbf{B}_{av} \mathbf{u} + \mathbf{f}_1, \\ \dot{\mathbf{f}}_1 &= \mathbf{f}_2, \\ &\vdots \\ \dot{\mathbf{f}}_{p-1} &= \mathbf{f}_p, \\ \dot{\mathbf{f}}_p &= \mathbf{r}^{(p)}(t). \end{aligned} \quad (4.12)$$

Define $\hat{\mathbf{e}}_1$ and $\hat{\mathbf{e}}_2$ as the estimation of \mathbf{e}_1 and \mathbf{e}_2 , respectively. Then the GPI observer can be derived for the error dynamics (4.12) as follows:

$$\begin{aligned}
\dot{\hat{\mathbf{e}}}_1 &= \hat{\mathbf{e}}_2 + \lambda_{p+1}\tilde{\mathbf{e}}, \\
\dot{\hat{\mathbf{e}}}_2 &= \mathbf{M}_{av}\mathbf{B}_{av}^{-1}\mathbf{u} + \hat{\mathbf{f}}_1 + \lambda_p\tilde{\mathbf{e}}, \\
\dot{\hat{\mathbf{f}}}_1 &= \hat{\mathbf{f}}_2 + \lambda_{p-1}\tilde{\mathbf{e}}, \\
&\vdots \\
\dot{\hat{\mathbf{f}}}_{p-1} &= \hat{\mathbf{f}}_p + \lambda_1\tilde{\mathbf{e}}, \\
\dot{\hat{\mathbf{f}}}_p &= \lambda_0\tilde{\mathbf{e}},
\end{aligned} \tag{4.13}$$

where $\tilde{\mathbf{e}} = \mathbf{e} - \hat{\mathbf{e}}_1$, λ_i , $i = 0, 1, \dots, p+1 \in \mathbb{R}^{3 \times 3}$ are the observer gains, $\hat{\mathbf{f}}_i$ is the estimation of \mathbf{f}_i , $i = 1, 2, \dots, p$. p is the order of GPI observer.

The selection of the observer gains λ_i ($i = 0, 1, \dots, p+1$) is to make sure that the poles of the decoupled observer error dynamics are placed at the desired locations for the three channels. The characteristic polynomial of the decoupled observer error dynamics is as follows:

$$\boldsymbol{\eta}(s) = s^{p+2}\mathbf{I} + \lambda_{p+1}s^{p+1} + \dots + \lambda_1s + \lambda_0, \tag{4.14}$$

where $\boldsymbol{\eta}(s) \in \mathbb{R}^3$.

For the sake of simplicity, all of the poles in the three channels are placed in the same location; that is,

$$\boldsymbol{\eta}(s) = (s + \omega_o)^{p+2}\mathbf{I}, \tag{4.15}$$

where ω_o ($\omega_o > 0$) is a parameter to specify the desired poles. Then the observer gains can be easily obtained by comparing (4.14) and (4.15).

Although theoretically speaking, higher order of GPI observer produces better estimation performance of the disturbances, especially fast varying disturbances. However, due to the fact that GPI observer is a high gain observer, the actuator saturation may happen because of large disturbances, noises, etc. For a higher order of GPI, it can be seen from (4.15) that the gains λ_i will be larger. In our experiments, we found that if $p \geq 3$, then measures have to be taken to avoid actuator saturation. For the sake of simplicity, we set $p = 2$ in this paper.

Then, according to (4.14) and (4.15), the observer gains are given as follows:

$$\begin{aligned}\lambda_0 &= \begin{bmatrix} \omega_o^4 & & \\ & \omega_o^4 & \\ & & \omega_o^4 \end{bmatrix}, \quad \lambda_1 = \begin{bmatrix} 4\omega_o^3 & & \\ & 4\omega_o^3 & \\ & & 4\omega_o^3 \end{bmatrix}, \\ \lambda_2 &= \begin{bmatrix} 6\omega_o^2 & & \\ & 6\omega_o^2 & \\ & & 6\omega_o^2 \end{bmatrix}, \quad \lambda_3 = \begin{bmatrix} 4\omega_o & & \\ & 4\omega_o & \\ & & 4\omega_o \end{bmatrix}.\end{aligned}$$

Finally, since $\hat{\mathbf{e}}_2$ is the estimation of $\dot{\mathbf{e}}$, the robot velocity can be estimated by GPI observer. Therefore, if in practice the accurate robot velocity cannot be obtained from installed sensors of the robot, then the controller (4.10) can be written by using the estimated velocity error as follows:

$$\mathbf{u} = (\mathbf{M}_{av}^{-1}\mathbf{B}_{av})^{-1}(-\hat{\mathbf{f}} - \mathbf{K}_p\mathbf{e} - \mathbf{K}_d\hat{\mathbf{e}}_2). \quad (4.16)$$

As seen in the controller (4.16) and GPI observer (4.13), \mathbf{M}_{av} and \mathbf{B}_{av} are the only required robot model information in the GPI observer based control system design. It is worthy pointing out that the matrix \mathbf{C} in (2.16) is not used in the proposed control design. Thereby, the involved parameter b_0 in \mathbf{C} is unnecessary to be known. It should be noted that the matrix \mathbf{C} is usually indispensable in the control of OMR [25, 28], to name a few. Therefore, only part of the robot model information is needed in the proposed control design. Moreover, a common rule of thumb to set ω_c and ω_o is to choose: $\omega_o \approx (3 - 5)\omega_c$.

4.1.3 Stability Analysis

Combining (4.5) and (4.10), the closed-loop error dynamic equation is obtained:

$$\ddot{\mathbf{e}} + \mathbf{K}_d\dot{\mathbf{e}} + \mathbf{K}_p\mathbf{e} = \tilde{\mathbf{f}}, \quad (4.17)$$

where $\tilde{\mathbf{f}} = \mathbf{f} - \hat{\mathbf{f}}$ is the estimation error of the time-varying perturbation input \mathbf{f} .

Note that the selection of \mathbf{K}_p and \mathbf{K}_d has resulted in a stable linear perturbed error dynamic system (4.17). On the other hand, the boundness of $\tilde{\mathbf{f}}$ can be guaranteed by the

designed observer. Therefore, the linear perturbed system (4.17) is bounded-input bounded-output (BIBO) stability. In addition, the bound of the error in (4.17) is proportional to the upper bound of $\tilde{\mathbf{f}}$ (i.e., $\|\tilde{\mathbf{f}}\|_\infty$), multiplied by the inverse of the absolute value of the smallest real part of the roots of (4.9) [58].

4.2 Simulation and Experimental Verification

4.2.1 Simulations

In this section, the proposed GPI observer based control system is compared with the average dynamic model based RAC through simulations. The simulations are implemented in Matlab/Simulink. The purpose is to verify that the performances of the control system can be improved by the partly compensation of the switching dynamics. It should be pointed out that the switching dynamics cannot be completely compensated due to limited bandwidth of the observer.

The parameter values of the robot prototype used in the simulations have been presented in Chapter 3. For the GPI observer based control system, the controller parameters and observer parameters are set as: $\omega_c = 4$ rad/s, $\xi = 5$, $\omega_o = 16$ rad/s. In other words, the \mathbf{K}_p and \mathbf{K}_d in (4.8) are set as:

$$\mathbf{K}_p = \begin{bmatrix} 16 & & \\ & 16 & \\ & & 16 \end{bmatrix}, \quad \mathbf{K}_d = \begin{bmatrix} 40 & & \\ & 40 & \\ & & 40 \end{bmatrix}. \quad (4.18)$$

For comparison purpose, the controller gains \mathbf{K}_p and \mathbf{K}_d of average dynamic model based RAC are set as the same of GPI observer based control system.

As already mentioned, the robot velocity tracking errors can be estimated by GPI observer, i.e., $\hat{\mathbf{e}}_2$ is the estimation of $\dot{\mathbf{e}}$. Therefore, in our simulations and experiments, the feedback signal of robot velocity tracking error is obtained from GPI observer. In other words, only robot position measurements are needed in the GPI observer based control. In

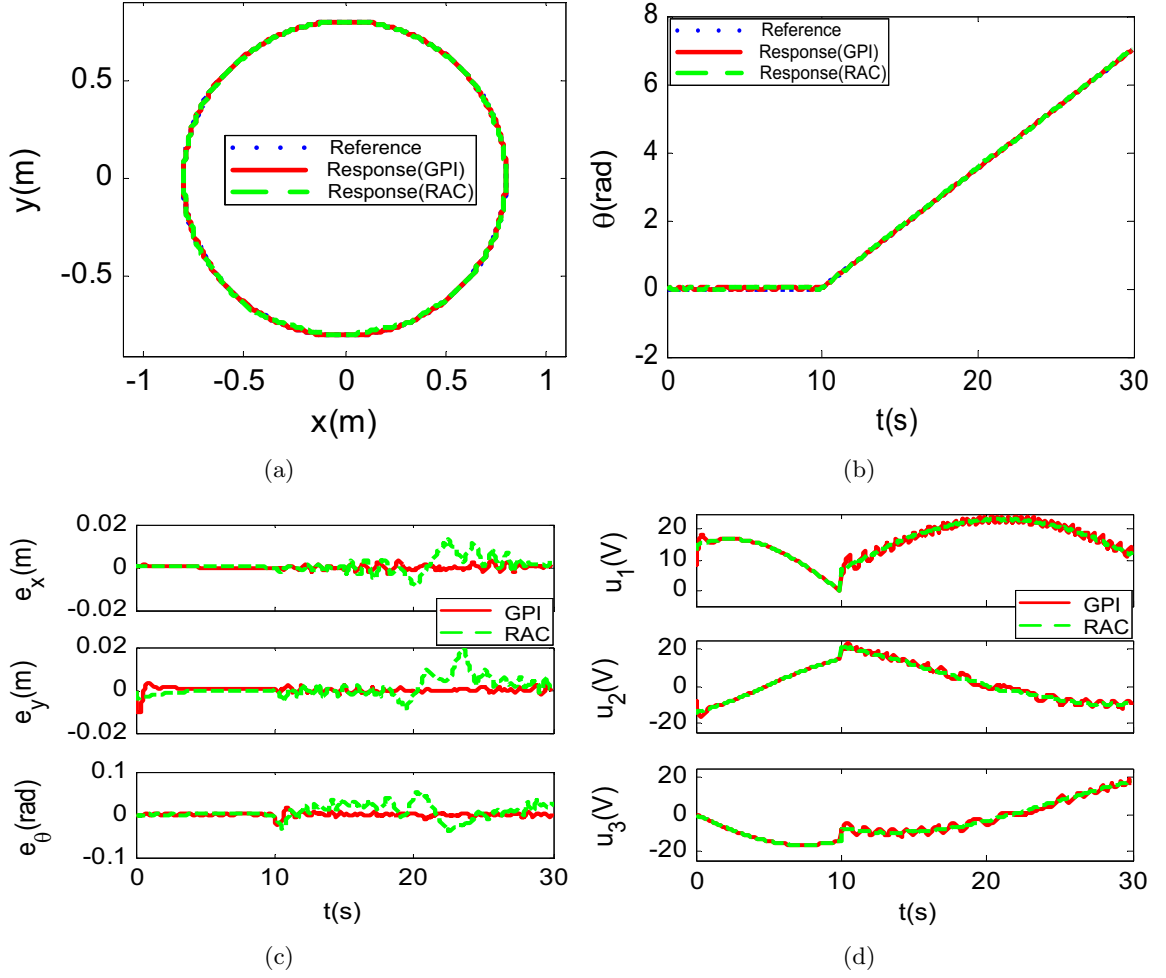


Figure 4.2: Simulation results of average dynamic model based RAC and GPI observer based control (circle trajectory): (a) Circle trajectory in the xy -plane: reference trajectory and responses. (b) Circle trajectory in the orientation direction: reference trajectory and responses. (c) Tracking errors. (d) Control input $\mathbf{u}(t)$.

Table 4.1: Simulation results: IAE of average dynamic model based RAC and GPI observer based control

Trajectory	Circle		Square		Lemniscate	
IAE	$IAE_{xy}(\text{m})$	$IAE_{\theta}(\text{rad})$	$IAE_{xy}(\text{m})$	$IAE_{\theta}(\text{rad})$	$IAE_{xy}(\text{m})$	$IAE_{\theta}(\text{rad})$
RAC	0.150	0.370	0.200	0.275	0.226	0.352
GPI	0.048	0.064	0.179	0.205	0.115	0.153

addition, since the GPI observer is a high gain observer and the path planning problem is out of the scope of this paper, the robot initial posture is set as the same with the initial start point of the robot trajectory, to avoid actuator saturation. The same three typical trajectories used in Chapter 3, i.e., circle, square and lemniscate trajectory, are employed as the reference trajectories. Simulation results are shown in Figure 4.2 - Figure 4.6. The IAE of average dynamic model based RAC and GPI observer based control is shown in Table 4.1.

It is shown in Table 4.1 that, for all the three trajectories, the control performances of GPI observer based control are better than the average dynamic model based RAC. These simulations only demonstrate that the control performances of average dynamic model based RAC can be improved by compensating the switching dynamics with GPI observer. Note that in our simulations, the “Robot” in Figure 4.1 is replaced by the switched nonlinear dynamic model (2.16). Therefore, the only differences between the average dynamic model and the switched nonlinear dynamic model are the unmodeled switching dynamics. The GPI observer based control in estimating and compensating the unmodeled forces as well as parameter uncertainties, will be introduced in our experiments.

Figure 4.3 (a) shows that the perturbation input vector \mathbf{f} is smooth in the first 10 s and fluctuations appear when the robot moves with rotation after 10 s. This has been analyzed in Chapter 3 that the robot is a simple linear system in the first 10 s and is a switched nonlinear system when the robot moves with rotation. It can also be seen that the GPI observer can well estimate the perturbation input vector \mathbf{f} in the first 10 s while cannot well estimate the sharp changes of \mathbf{f} after 10 s. This is because the instantaneous switching events between

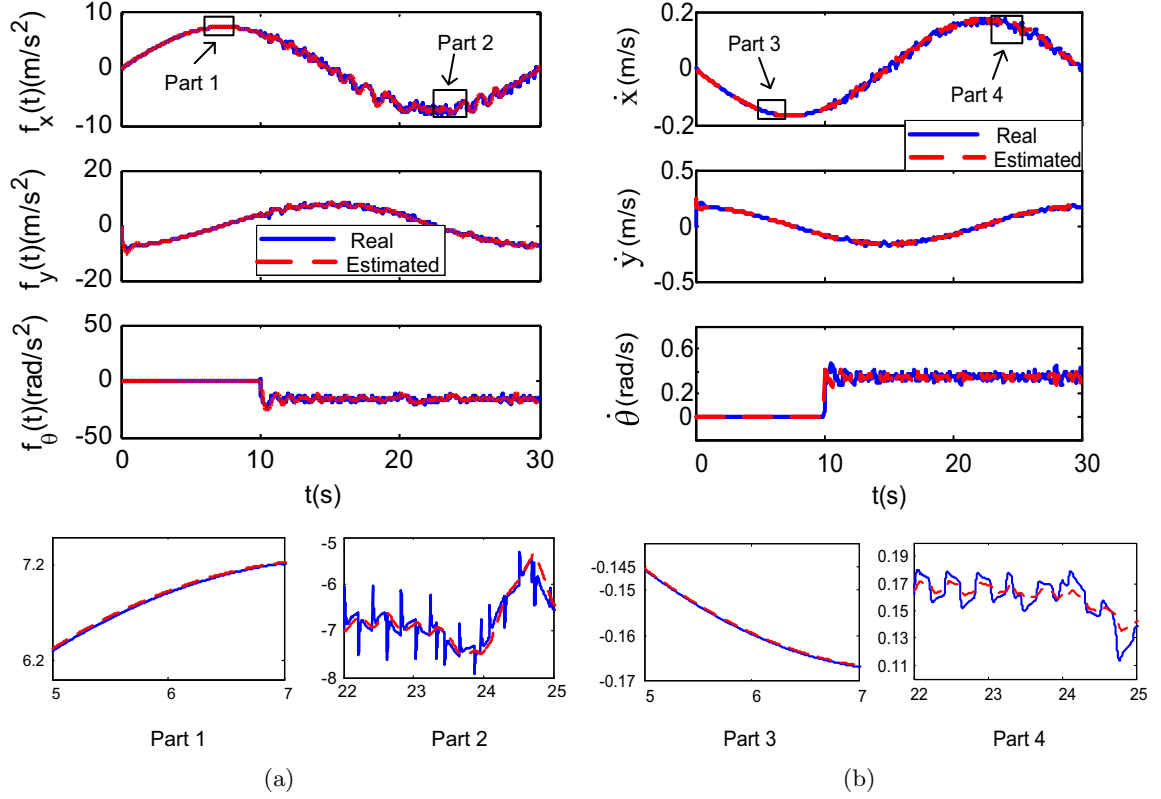


Figure 4.3: Simulation results of GPI observer based control (circle trajectory): (a) Real perturbation input vector \mathbf{f} and its estimation by the GPI observer $\hat{\mathbf{f}}(t)$. (b) Real robot velocity and its estimation by the GPI observer.

two subsystems happen very fast. The GPI observer cannot accurately estimate the fast-varying changing dynamics. In other words, the robot switching dynamics can only be partly compensated by the GPI observer, and thus cannot be completely compensated in the control signal. It is observed in Figure 4.2 (d) that the control input of GPI observer based control has fluctuations after 10 s while the control input of average dynamic model based RAC is smooth. The fluctuations in the control input are introduced due to the switching dynamics estimated by GPI observer.

Figure 4.3 (b) shows the estimation performance of the robot velocity. It is observed that, fluctuations in the robot velocity are introduced when the robot moves with rotation. This is resulted from the fact that the switching dynamics, especially the sharp changes, cannot be well estimated and completely compensated in the control signal. In addition, it is also observed that the robot velocity cannot be well estimated by GPI observer when the robot moves with rotation, since the robot velocity changes fast due to the switching of the robot dynamics. Due to the estimation errors of the robot velocity by GPI observer, it is worth noting that the control performances of GPI observer based control can be further improved by using the real robot velocity in the feedback, instead of the one estimated by GPI observer.

Even though both average dynamic model based RAC and GPI observer based control are designed based on continuous dynamic models, the robot prototype itself is a switched nonlinear system. The switching signals (i.e., contact radius) of both control systems are shown in Figure 4.4.

4.2.2 Experiments

As already mentioned, two aspects of the modeling errors of the average dynamic model, i.e., unmodeled forces and parameter uncertainties in practice, are not considered in the above simulations. In this part, experimental tests of the three trajectories are conducted to verify the effectiveness of GPI observer based control in estimation and compensation of these modeling errors, as well as the unmodeled switching dynamics. The experimental

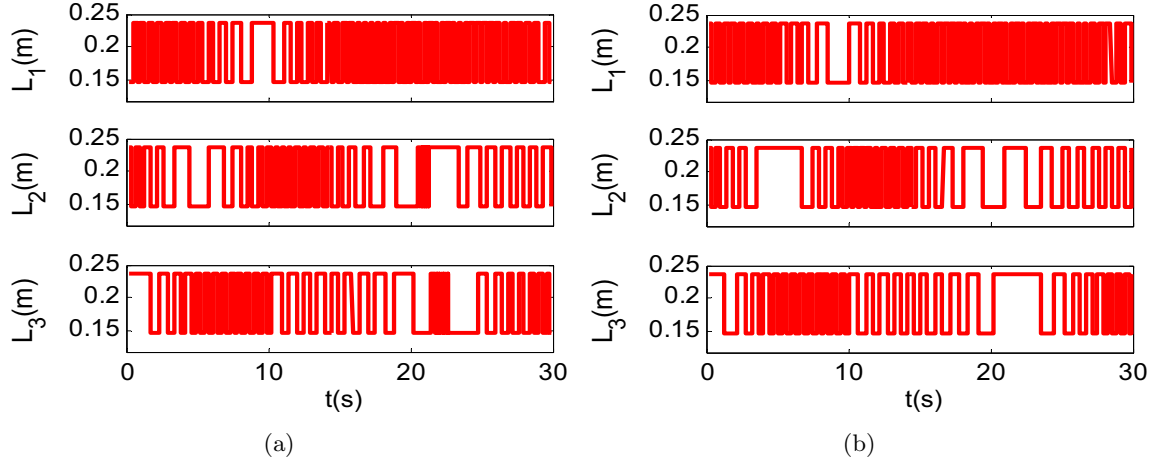


Figure 4.4: Simulation results of average dynamic model based RAC and GPI observer based control (circle trajectory): (a) Contact radius of average model based RAC (L_i , $i=1,2,3$). (b) Contact radius of the GPI observer based control (L_i , $i=1,2,3$).

Table 4.2: Experimental results: IAE of average dynamic model based RAC and GPI observer based control

Trajectory	Circle		Square		Lemniscate	
IAE	$IAE_{xy}(m)$	$IAE_{\theta}(rad)$	$IAE_{xy}(m)$	$IAE_{\theta}(rad)$	$IAE_{xy}(m)$	$IAE_{\theta}(rad)$
RAC	0.979	1.972	0.800	1.074	0.646	1.360
GPI	0.103	0.153	0.182	0.192	0.115	0.158

results of average dynamic model based RAC in Chapter 3 are also presented here for comparisons. The experimental setup and robot dynamic parameters have been introduced in Chapter 2 and 3, respectively. The control parameters of both control systems, i.e., average dynamic model based RAC and GPI observer based control, are set as the same with those of simulations. Experimental results are shown in Figure 4.7 - Figure 4.10. The IAE of average dynamic model based RAC and GPI observer based control is shown in Table 4.2. Note that the experimental results in Table 4.2 are the average results of experiments with three times. The original data is shown in Appendix D.

As shown in Table 4.2, GPI observer based control achieves much better performances than the average dynamic model based RAC (also see Figure 4.7 (c), Figure 4.9 (c), and

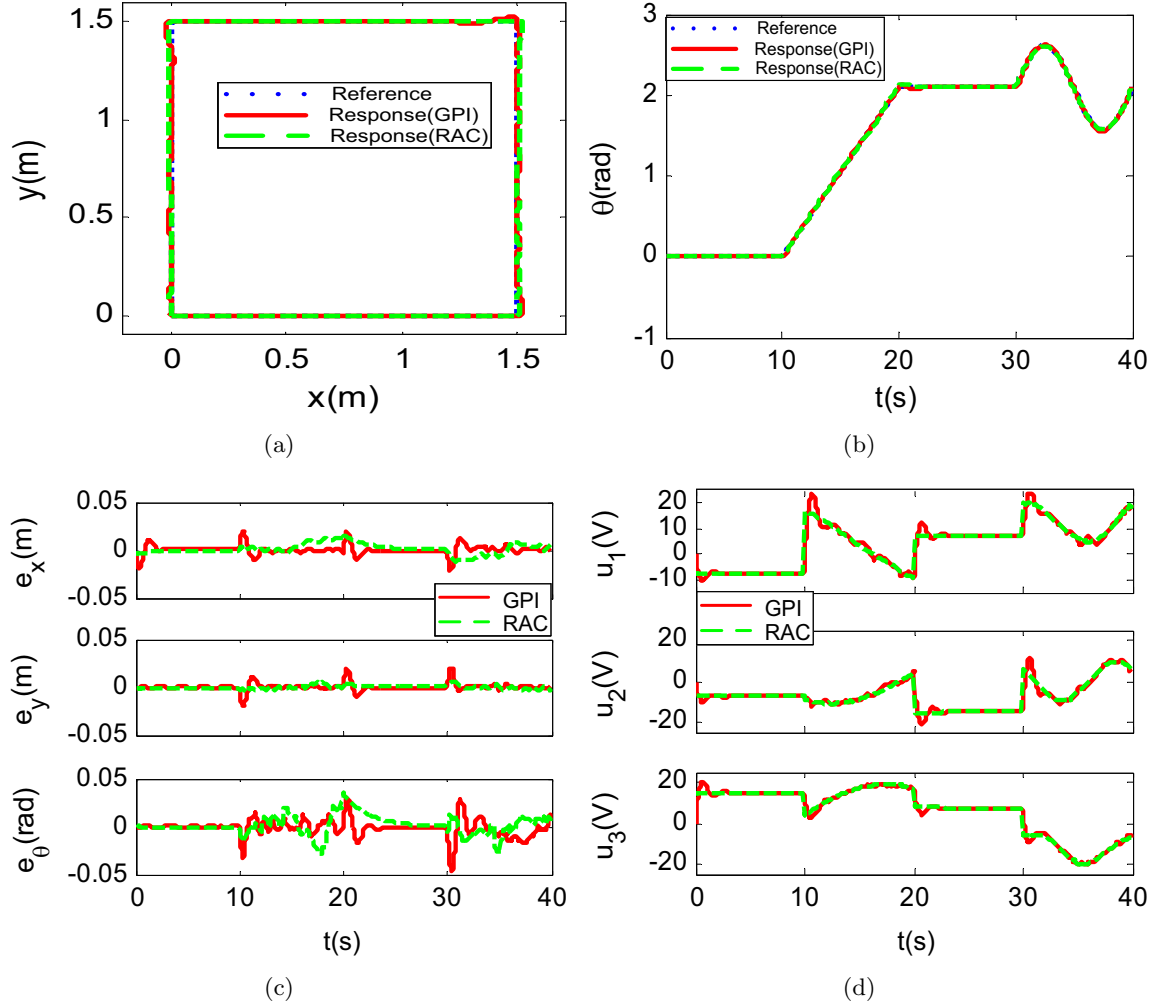


Figure 4.5: Simulation results of average dynamic model based RAC and GPI observer based control (square trajectory): (a) Robot trajectory in the xy-plane: reference trajectory and responses. (b) Robot trajectory in the orientation direction: reference trajectory and responses. (c) Tracking errors. (d) Control input $\mathbf{u}(t)$.

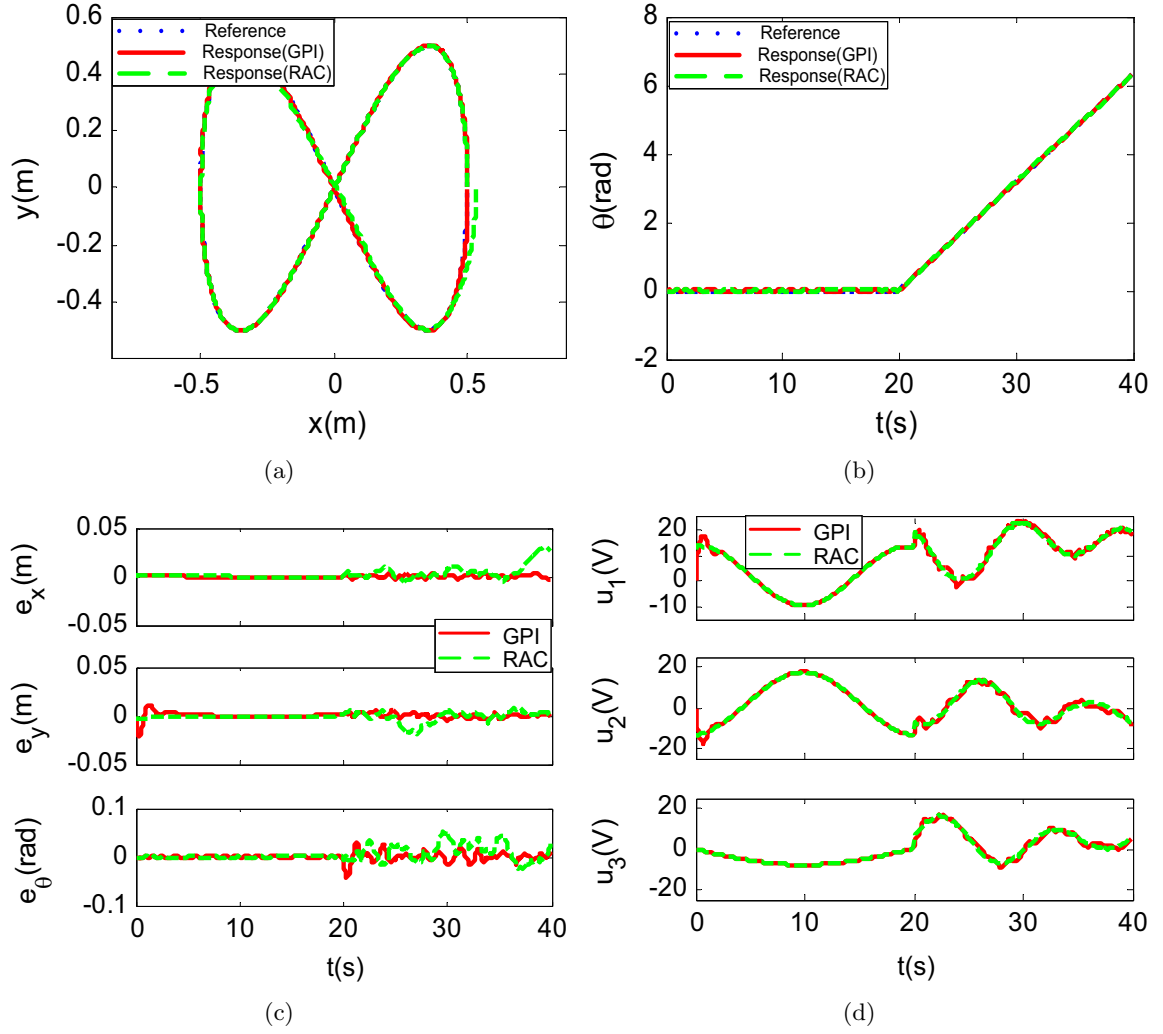


Figure 4.6: Simulation results of average dynamic model based RAC and GPI observer based control (lemniscate trajectory): (a) Robot trajectory in the xy-plane: reference trajectory and responses. (b) Robot trajectory in the orientation direction: reference trajectory and responses. (c) Tracking errors. (d) Control input $\mathbf{u}(t)$.

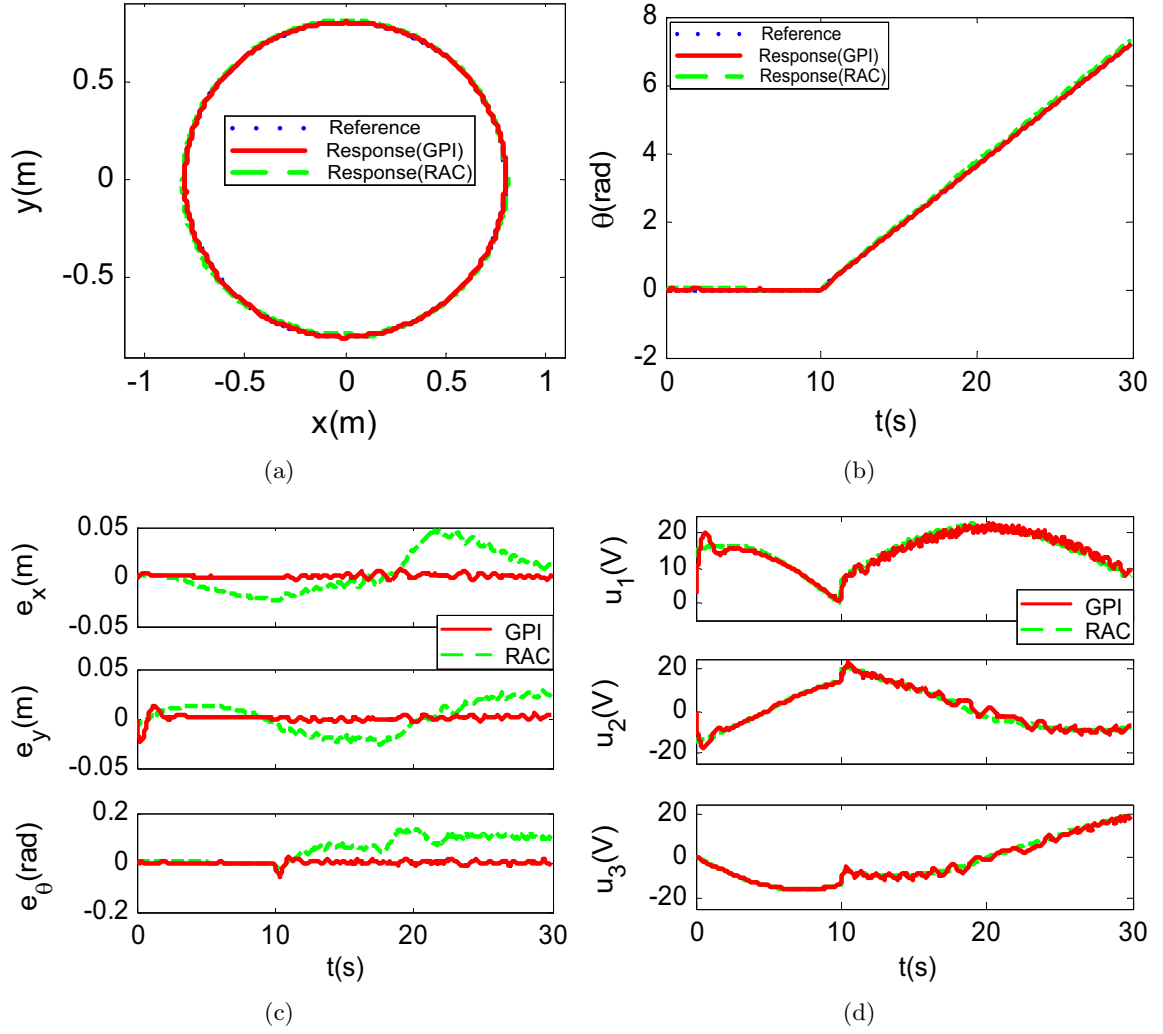


Figure 4.7: Experimental results of average dynamic model based RAC and GPI observer based control (circle trajectory): (a) Circle trajectory in the xy-plane: reference trajectory and responses. (b) Circle trajectory in the orientation direction: reference trajectory and responses. (c) Tracking errors. (d) Control input $\mathbf{u}(t)$.

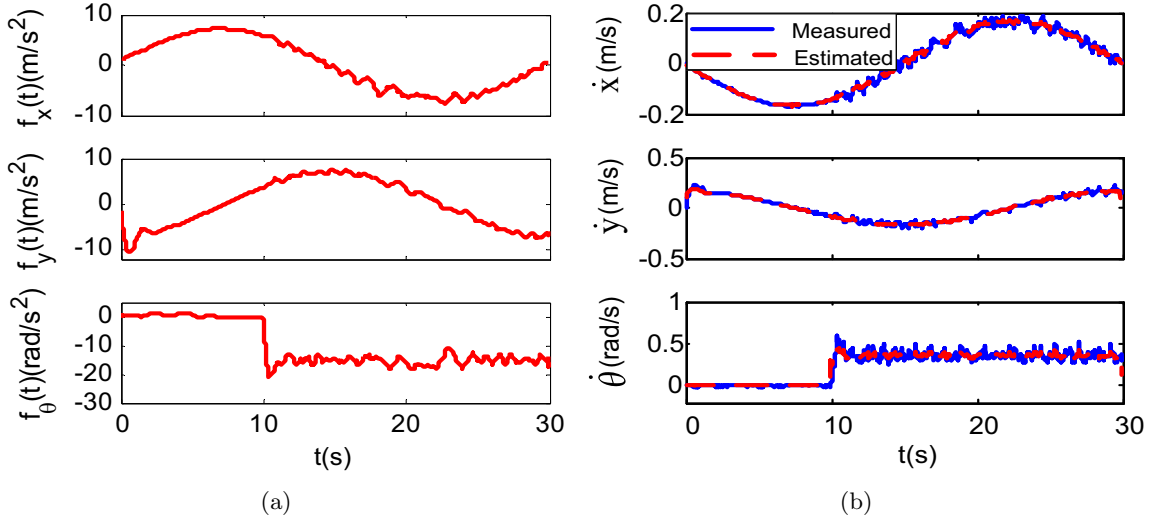


Figure 4.8: Experimental results of GPI observer based control (circle trajectory): (a) Estimation of perturbation input vector by the GPI observer $\hat{\mathbf{f}}(t)$. (b) Measured robot velocity and its estimation by the GPI observer.

Figure 4.10 (c)). Note the controller and observer parameters are set as the same for the three trajectories, and thus no retuning is conducted. In the experiments, since GPI observer based control is designed based on the average dynamic model, the GPI observer thus estimates the modeling errors of the average dynamic model. In other words, the modeling errors of average dynamic model, i.e., 1). unmodeled switching dynamics; 2). unmodeled forces; 3). parameter uncertainties, are estimated by GPI observer and compensated in the control signal. Therefore, the control performances of GPI observer based control are much better than average dynamic model based control. The estimated perturbation input $\hat{\mathbf{f}}(t)$ is shown in Figure 4.8 (a). The above modeling errors as well as the input-output cross coupling effects are contained in $\hat{\mathbf{f}}(t)$. It should be reminded that the GPI observer can only estimate part of the switching dynamics.

In our experiments, the robot velocity is estimated by GPI observer. Therefore, the designed control system is output feedback control and thus only robot position information is needed. This is one advantage of GPI observer based control compared with average dynamic model based RAC, which is state feedback and thus both the robot position and

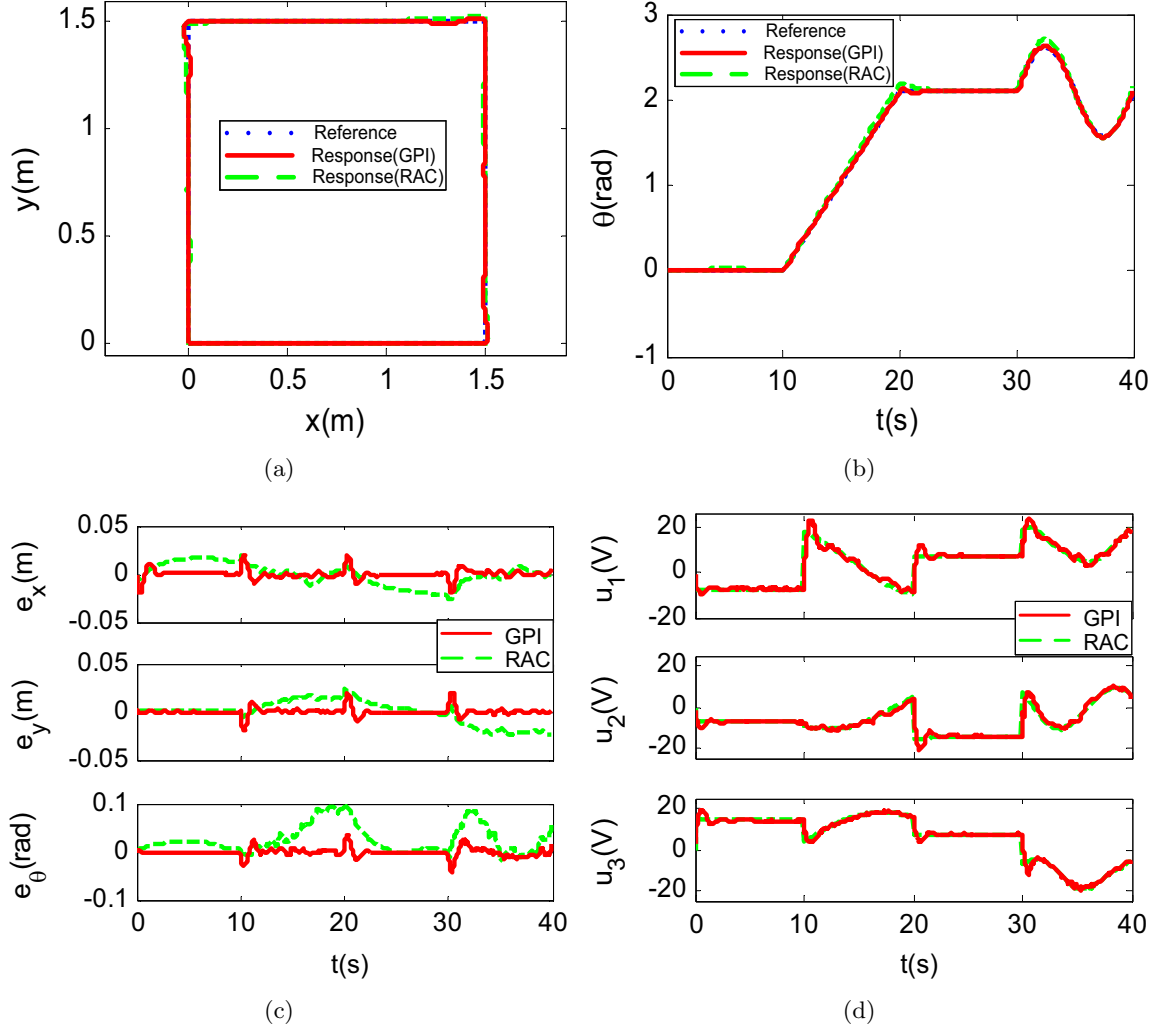


Figure 4.9: Experimental results of average dynamic model based RAC and GPI observer based control (square trajectory): (a) Robot trajectory in the xy-plane: reference trajectory and responses. (b) Robot trajectory in the orientation direction: reference trajectory and responses. (c) Tracking errors. (d) Control input $\mathbf{u}(t)$.

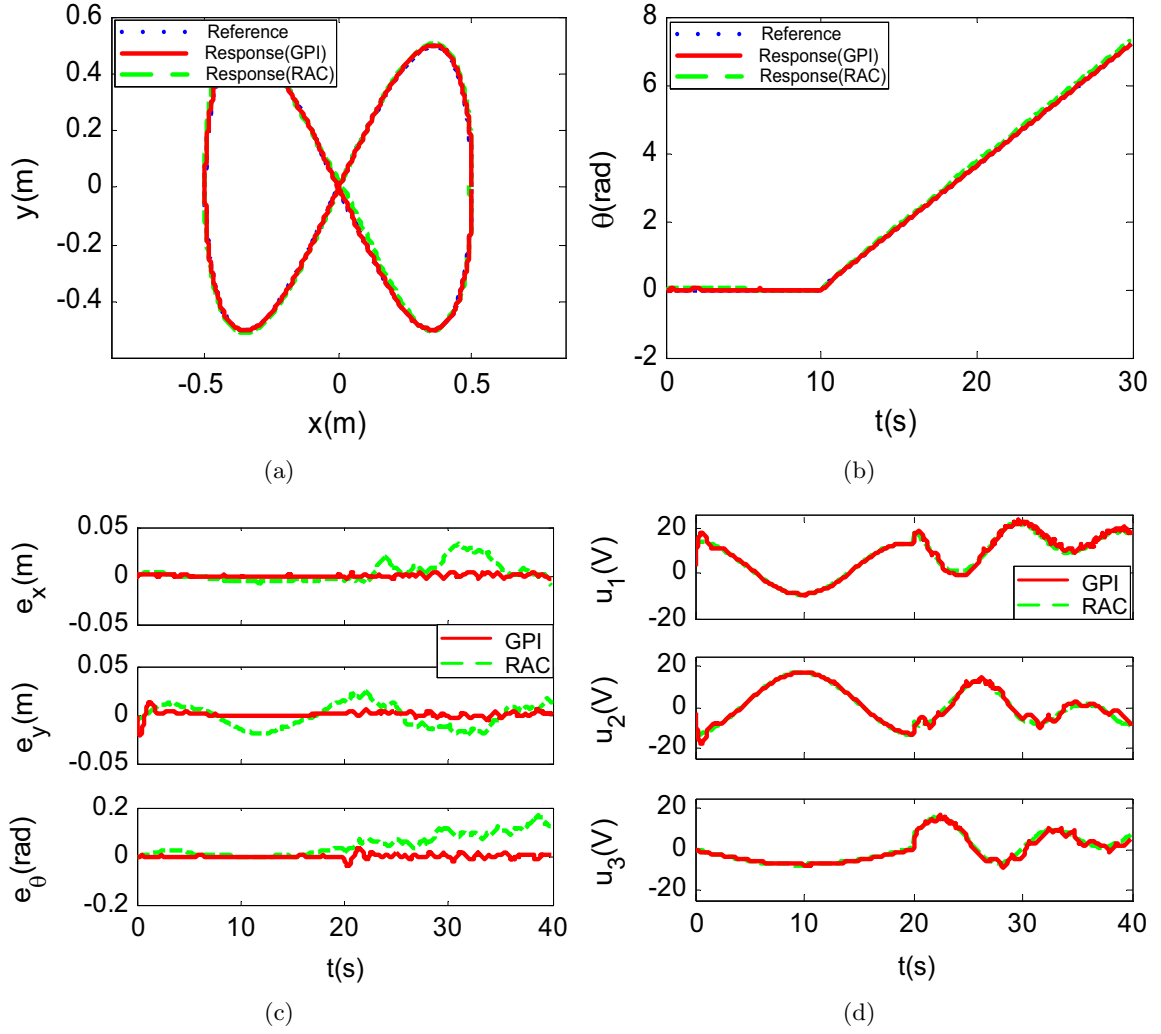


Figure 4.10: Experimental results of average dynamic model based RAC and GPI observer based control (lemniscate trajectory): (a) Robot trajectory in the xy-plane: reference trajectory and responses. (b) Robot trajectory in the orientation direction: reference trajectory and responses. (c) Tracking errors. (d) Control input $\mathbf{u}(t)$.

velocity information is required. The estimation performance of the robot velocity is shown in Figure 4.8 (b).

It is shown in Figure 4.7 (c), Figure 4.9 (c), and Figure 4.10 (c), that, when sudden changes in the robot states occur, larger transient errors are introduced in GPI observer based control compared with average dynamic model based RAC. This is caused by the transient response of GPI observer.

In addition, robustness is an important index for the control system design. The comparisons of the robustness between average dynamic model based RAC and GPI observer based control are shown in Chapter 5.

4.3 Summary

In this chapter, based on the average dynamic model derived in Chapter 3, a trajectory tracking control system based on GPI observer has been designed. The GPI observer is employed to estimate the modeling errors in the average dynamic model, i.e., 1). unmodeled switching dynamics; 2). unmodeled forces; and 3). parameter uncertainties. In the GPI observer based control, all of the above modeling errors, as well as the input-output cross coupling effects are considered as an unknown time-varying perturbation input vector. This perturbation input vector is then online estimated by the GPI observer, and compensated in the control signal. BIBO stability is guaranteed in the designed control system. Both simulations and experimental results show that the GPI observer based control achieves better performances than average dynamic model based RAC. It should also be noted that only part of the model information is needed in the GPI observer based control.

Chapter 5

Passivity based Model Free Control (MFC)

In literature, the control of OMRs based on dynamic model has been studied in many papers [25, 26, 27, 30, 31], to name a few. In Chapter 4, we have proposed a GPI observer based control design for our robot prototype. Only part of the model information is used. The coriolis matrix \mathbf{C}_{av} in the average dynamic model (3.1) is not used in the designed control system. However, in the above dynamic model based control approaches, all or at least part of the dynamic model information is needed to implement the controller. In particular, some of these control approaches are somewhat complex in the structure and require heavy computation or have several parameters to tune. In practical applications, it is usually expected that the least model information is needed in the control system design and the tuning parameters are as few as possible, while the control performance can be satisfied.

On the other hand, passivity is one of the most fundamental properties of robotic systems [65, 66]. It has been a very powerful concept in many control problems of robotics: stability analysis [67, 68, 69], teleoperation control [70, 71, 72, 73], flexible robot control [74, 75, 76, 77], to name a few. However, so far, it has been overlooked for the control problem of OMRs.

In [78], a passivity-based complete model free control (MFC) approach is proposed for robot manipulators by employing a modified GPI observer. In this chapter, inspired by ideas from [78], a passivity-based trajectory tracking control system is designed for our robot prototype. Firstly, the passivity property of our robot prototype is analyzed based on the average dynamic model (3.1). Then a trajectory tracking control system is designed based on a modified GPI observer. The design objective is to preserve the passivity property of the robot in the closed-loop system, which is different from the RAC or GPI observer based control. The resulting control system is almost model free, since both the robot inertia matrix and coriolis matrix are unnecessary. The required information is the robot geometrical information only. More specifically, only the average contact radius (L_a) is required. As a result, the arduous identification process of dynamic parameters can be avoided. Stability property is analyzed. Finally, the performances of the proposed control design are compared and discussed with the previous control designs in Chapter 3 and Chapter 4, i.e., average dynamic model based RAC and GPI observer based control, through experiments.

5.1 Passivity Analysis

In this chapter, the average dynamic model is used to analyze the passivity properties. To facilitate the analysis of passivity property, by premultiplying (3.1) by ${}^w_M \mathbf{R}$, we have,

$$\mathbf{M}\ddot{\mathbf{q}} + \mathbf{C}\dot{\mathbf{q}} + \mathbf{D}\dot{\mathbf{q}} = \boldsymbol{\tau}, \quad (5.1)$$

where $\boldsymbol{\tau} = \mathbf{B}\mathbf{u}$, which is considered as the virtual control input in this thesis, and

$$\mathbf{M} = \frac{1}{\beta_2} \begin{bmatrix} \frac{3}{2}\beta_0 + m & 0 & 0 \\ 0 & \frac{3}{2}\beta_0 + m & 0 \\ 0 & 0 & 3\beta_0 L_0^2 + I_v \end{bmatrix}, \mathbf{C} = \frac{1}{\beta_2} \begin{bmatrix} 0 & \frac{3}{2}\beta_0 \dot{\theta} & 0 \\ -\frac{3}{2}\beta_0 \dot{\theta} & 0 & 0 \\ 0 & 0 & 0 \end{bmatrix},$$

$$\mathbf{D} = \frac{1}{\beta_2} \begin{bmatrix} \frac{3}{2}\beta_1 & 0 & 0 \\ 0 & \frac{3}{2}\beta_1 & 0 \\ 0 & 0 & 3\beta_1 L_0^2 \end{bmatrix},$$

$$\mathbf{B} = \frac{1}{2} \begin{bmatrix} -\cos \theta - \sqrt{3} \sin \theta & -\cos \theta + \sqrt{3} \sin \theta & 2 \cos \theta \\ -\sin \theta + \sqrt{3} \cos \theta & -\sin \theta - \sqrt{3} \cos \theta & 2 \sin \theta \\ 2L_0 & 2L_0 & 2L_0 \end{bmatrix},$$

and $\mathbf{D}\dot{\mathbf{q}}$ is the dissipative force, due to the combined Viscous friction of the motor, gear and wheel shaft, as well as the motor armature resistance. This relates to the loss or dissipation of energy.

It can be seen that the inertia matrix \mathbf{M} is symmetric, positive definite, and both \mathbf{M} and \mathbf{M}^{-1} are uniformly bounded. In addition, the total energy of the open-loop dynamic system (5.1) is

$$V(\mathbf{q}, \dot{\mathbf{q}}) = \frac{1}{2} \dot{\mathbf{q}}^T \mathbf{M} \dot{\mathbf{q}}. \quad (5.2)$$

The time derivative of the energy function (5.2) along (5.1) is:

$$\begin{aligned} \dot{V}(\mathbf{q}, \dot{\mathbf{q}}) &= \dot{\mathbf{q}}^T \mathbf{M} \ddot{\mathbf{q}} \\ &= \dot{\mathbf{q}}^T (\boldsymbol{\tau} - \mathbf{C}\dot{\mathbf{q}} - \mathbf{D}\dot{\mathbf{q}}) \\ &= \dot{\mathbf{q}}^T \boldsymbol{\tau} - \dot{\mathbf{q}}^T \mathbf{C}\dot{\mathbf{q}} - \dot{\mathbf{q}}^T \mathbf{D}\dot{\mathbf{q}} \\ &= \dot{\mathbf{q}}^T \boldsymbol{\tau} - \dot{\mathbf{q}}^T \mathbf{D}\dot{\mathbf{q}}. \end{aligned}$$

Note that \mathbf{D} is symmetric and positive definite and thus $\dot{\mathbf{q}}^T \mathbf{D}\dot{\mathbf{q}} > 0$. Therefore, according to the standard passivity definition [79], (5.1) defines an output strictly passive mapping from the virtual control input $\boldsymbol{\tau}$ to $\dot{\mathbf{q}}$. Note that, the passive mapping from the real control input \mathbf{u} to $\dot{\mathbf{q}}$ cannot be guaranteed.

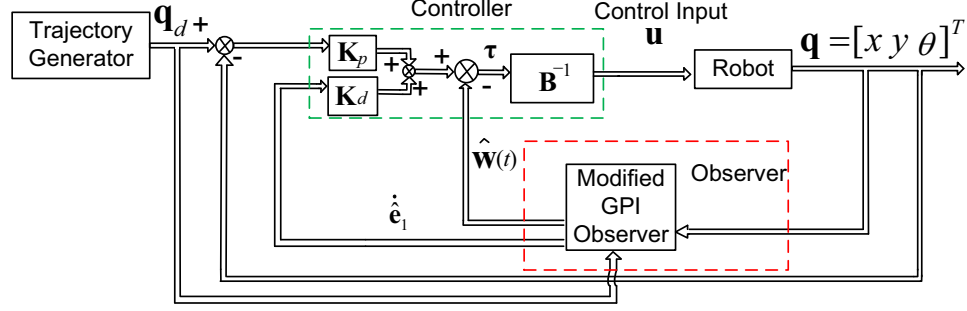


Figure 5.1: Block diagram of passivity based MFC for the mobile robot.

Remark 1. The matrix \mathbf{D} can be rewritten as follows:

$$\mathbf{D} = \frac{nR_a}{rk_t} \left(b_0 + \frac{k_t k_b}{R_a} \right) \begin{bmatrix} \frac{3}{2} & 0 & 0 \\ 0 & \frac{3}{2} & 0 \\ 0 & 0 & 3L_0^2 \end{bmatrix}.$$

It can be seen that, the dissipative force $\mathbf{D}\dot{\mathbf{q}}$ is related with the gear reduction ratio and wheel radius. More specifically, the dissipative force has a positive correlation with the gear reduction ratio n and a inverse correlation with the wheel radius r .

5.2 Passivity based MFC

5.2.1 Control System Design

The block diagram of passivity based MFC is shown in Figure 5.1.

Assuming that the robot dynamic equation (5.1) is known, the well-known passivity-based trajectory tracking controller can be obtained as follows [80]:

$$\tau = \mathbf{M}\ddot{\mathbf{q}}_r + (\mathbf{C} + \mathbf{D})\dot{\mathbf{q}}_r - \mathbf{K}_d \mathbf{s}, \quad (5.3)$$

where $\mathbf{e} = \mathbf{q} - \mathbf{q}_d$, $\dot{\mathbf{q}}_r = \dot{\mathbf{q}}_d - \mathbf{\Lambda}\mathbf{e}$, $\mathbf{s} = \dot{\mathbf{e}} + \mathbf{\Lambda}\mathbf{e}$, \mathbf{K}_d and $\mathbf{\Lambda} \in \mathbb{R}^{3 \times 3}$ are diagonal positive definite matrices.

Then the closed-loop error dynamics can be obtained as follows:

$$\mathbf{M}\dot{\mathbf{s}} + \mathbf{C}\mathbf{s} + \mathbf{D}\mathbf{s} + \mathbf{K}_d\mathbf{s} = 0, \quad (5.4)$$

Based on Lyapunov analysis, it is straightforward to obtain that $\mathbf{s} \rightarrow 0$ as $t \rightarrow \infty$, and thus $\mathbf{e} \rightarrow 0$, $\dot{\mathbf{e}} \rightarrow 0$ as $t \rightarrow \infty$ [80].

By using the controller (5.3), it is intuitively clear that the energy minimum of open-loop system (5.1), i.e., $(\mathbf{q}, \dot{\mathbf{q}}) = (0, 0)$, has been shifted to $(\mathbf{e}, \dot{\mathbf{e}}) = (0, 0)$. Note that the total energy of the open-loop system (5.1) is

$$\mathbf{H}_0(\mathbf{q}, \dot{\mathbf{q}}) = \frac{1}{2} \dot{\mathbf{q}}^T \mathbf{M} \dot{\mathbf{q}}. \quad (5.5)$$

The controller (5.3) actually reshapes the original open-loop energy function of (5.5) into

$$\mathbf{H}_1(\mathbf{e}, \dot{\mathbf{e}}) = \frac{1}{2} \mathbf{s}^T \mathbf{M} \mathbf{s}, \quad (5.6)$$

which is the total energy of (5.4). This is the well-known energy shaping plus damping injection ideas of the passivity-based control approach [81]. The first step is an energy shaping stage where the potential energy of the system is modified in such a way that the new potential energy function has a global and unique minimum in the desired equilibriums. Second, a damping injection stage where the dissipation function is modified to ensure global asymptotic stability.

Now we consider the case that the matrix \mathbf{M} , \mathbf{C} and \mathbf{D} in (5.1) are completely unknown and only the input matrix \mathbf{B} is known. In other words, only the robot geometrical information is known. Our objective is to design a controller which results in a closed-loop system maintaining the same structure of (5.4), which is to maintain the passivity property.

The nominal system can be obtained on the basis of the desired trajectory as follows:

$$\mathbf{M}\ddot{\mathbf{q}}_d + \mathbf{C}(\dot{\mathbf{q}}_d)\dot{\mathbf{q}}_d + \mathbf{D}\dot{\mathbf{q}}_d = \boldsymbol{\tau}_d. \quad (5.7)$$

Then the open-loop tracking error dynamics can be obtained by (5.1) and (5.7) as

$$\ddot{\mathbf{e}} = \ddot{\mathbf{q}} - \ddot{\mathbf{q}}_d = \mathbf{M}^{-1}\boldsymbol{\tau} + \mathbf{M}^{-1}(\mathbf{C}(\dot{\mathbf{q}}_d)\dot{\mathbf{q}}_d + \mathbf{D}\dot{\mathbf{q}}_d - \mathbf{C}(\dot{\mathbf{q}})\dot{\mathbf{q}} - \mathbf{D}\dot{\mathbf{q}} - \boldsymbol{\tau}_d) + \boldsymbol{\xi}(t), \quad (5.8)$$

where $\boldsymbol{\xi}(t) \in \mathbb{R}^{3 \times 1}$ representing the modeling errors of the average dynamic model, including switching dynamics, unmodeled forces, and parameter uncertainties.

Equation (5.8) can be rewritten as

$$\begin{aligned} \ddot{\mathbf{e}} = & -\boldsymbol{\Lambda}\mathbf{e} + \mathbf{M}^{-1}(\boldsymbol{\tau} - \mathbf{C}(\dot{\mathbf{q}})\mathbf{s} - \mathbf{D}\mathbf{s}) + \mathbf{M}^{-1}(\mathbf{C}(\dot{\mathbf{q}}_d)\dot{\mathbf{q}}_d + \mathbf{D}\dot{\mathbf{q}}_d - \mathbf{C}(\dot{\mathbf{q}})\dot{\mathbf{q}} - \mathbf{D}\dot{\mathbf{q}} - \boldsymbol{\tau}_d) \\ & + \boldsymbol{\Lambda}\mathbf{e} + \mathbf{M}^{-1}(\mathbf{C}(\dot{\mathbf{q}}) + \mathbf{D})\mathbf{s} + \boldsymbol{\xi}(t) \end{aligned} \quad (5.9)$$

Define

$$\mathbf{f} = \mathbf{M}^{-1}(\mathbf{C}(\dot{\mathbf{q}}_d)\dot{\mathbf{q}}_d + \mathbf{D}\dot{\mathbf{q}}_d - \mathbf{C}(\dot{\mathbf{q}})\dot{\mathbf{q}} - \mathbf{D}\dot{\mathbf{q}} - \boldsymbol{\tau}_d) + \boldsymbol{\Lambda}\mathbf{e} + \mathbf{M}^{-1}(\mathbf{C}(\dot{\mathbf{q}}) + \mathbf{D})\mathbf{s} + \boldsymbol{\xi}(t),$$

where \mathbf{f} is the time-varying perturbation input vector.

Finally, the open-loop tracking error dynamics can be expressed as

$$\ddot{\mathbf{e}} = -\boldsymbol{\Lambda}\mathbf{e} + \mathbf{M}^{-1}(\boldsymbol{\tau} - \mathbf{C}(\dot{\mathbf{q}})\mathbf{s}) + \mathbf{f}. \quad (5.10)$$

Defining $\mathbf{w} = \mathbf{M}\mathbf{f}$, we have the following assumption:

Assumption: The time-varying perturbation input vector \mathbf{w} can be approximated by a $(p - 1)$ -degree family of Taylor time-polynomial inputs and a residual term; that is,

$$\mathbf{w}(t) \approx \sum_{i=0}^{p-1} \alpha_i t^i + \boldsymbol{\delta}(t), \quad (5.11)$$

with $\alpha_i \in \mathbb{R}^{3 \times 1}$ being constant coefficients, and the j th time derivatives of the residual term $\boldsymbol{\delta}(t)$, i.e., $\boldsymbol{\delta}^{(j)}(t) (j \geq p)$, being uniformly absolutely bounded. Thus we have $\mathbf{w}^{(p)}(t) = \boldsymbol{\delta}^{(p)}(t)$.

Define $\mathbf{e}_1 = \mathbf{e}$, $\mathbf{e}_2 = \dot{\mathbf{e}}$ and $\mathbf{w}_1 = \mathbf{w}$. Then the open-loop tracking error dynamics (5.10) can be rewritten in state space as

$$\begin{aligned} \dot{\mathbf{e}}_1 &= \mathbf{e}_2, \\ \dot{\mathbf{e}}_2 &= -\boldsymbol{\Lambda}\mathbf{e} + \mathbf{M}^{-1}(\boldsymbol{\tau} - \mathbf{C}(\dot{\mathbf{q}})\mathbf{s} - \mathbf{D}\mathbf{s}) + \mathbf{M}^{-1}\mathbf{w}_1, \\ \dot{\mathbf{w}}_1 &= \mathbf{w}_2, \\ &\vdots \\ \dot{\mathbf{w}}_{p-1} &= \mathbf{w}_p, \\ \dot{\mathbf{w}}_p &= \boldsymbol{\delta}^{(p)}(t), \end{aligned} \quad (5.12)$$

Define $\hat{\mathbf{e}}_1$ and $\hat{\mathbf{e}}_2$ as the estimation of \mathbf{e}_1 and \mathbf{e}_2 , respectively. Then a modified GPI observer can be derived for the error dynamics (5.12) as follows [78]:

$$\begin{aligned}
\dot{\hat{\mathbf{e}}}_1 &= \hat{\mathbf{e}}_2 - \Lambda \hat{\mathbf{e}}_1 + (\lambda_{p+1} - \Lambda) \tilde{\mathbf{e}}, \\
\dot{\hat{\mathbf{e}}}_2 &= \lambda_p \tilde{\mathbf{e}}, \\
\dot{\hat{\mathbf{w}}}_1 &= \hat{\mathbf{w}}_2 + \lambda_{p-1} \tilde{\mathbf{e}}, \\
&\vdots \\
\dot{\hat{\mathbf{w}}}_{p-1} &= \hat{\mathbf{w}}_p + \lambda_1 \tilde{\mathbf{e}}, \\
\dot{\hat{\mathbf{w}}}_p &= \lambda_0 \tilde{\mathbf{e}},
\end{aligned} \tag{5.13}$$

where $\tilde{\mathbf{e}} = \mathbf{e} - \hat{\mathbf{e}}_1$, the observer gains λ_i , $i = 0, 1, \dots, p+1 \in \mathbb{R}^{3 \times 3}$ are diagonal positive definite. $\hat{\mathbf{w}}_i$ is the estimation of \mathbf{w}_i , $i = 1, 2, \dots, p$. p is the order of GPI observer.

The selection of λ_i is to make sure that the poles of the observer error dynamics in three channels are placed at the desired locations. The characteristic polynomial of the observer error dynamics is as follows:

$$\eta(s) = s^{p+2} \mathbf{I} + \lambda_{p+1} s^{p+1} + \dots + \lambda_1 s + \lambda_0, \tag{5.14}$$

where $\eta(t) \in \mathbb{R}^{3 \times 1}$. With proper selection of λ_i , we have $\dot{\mathbf{e}} \approx \dot{\hat{\mathbf{e}}}$, and $\mathbf{w} \approx \hat{\mathbf{w}}_1$.

For the sake of simplicity, all of the poles in the three channels are placed in the same location; that is,

$$\eta(s) = (s + \omega_o)^{p+2} \mathbf{I}, \tag{5.15}$$

where ω_o ($\omega_o > 0$) is a parameter to specify the desired poles.

In this thesis, the observer order p is set as 2, and then the observer gains can be easily obtained by comparing (5.14) and (5.15) as follows:

$$\lambda_0 = \begin{bmatrix} \omega_o^4 & & \\ & \omega_o^4 & \\ & & \omega_o^4 \end{bmatrix}, \quad \lambda_1 = \begin{bmatrix} 4\omega_o^3 & & \\ & 4\omega_o^3 & \\ & & 4\omega_o^3 \end{bmatrix},$$

$$\lambda_2 = \begin{bmatrix} 6\omega_o^2 & & \\ & 6\omega_o^2 & \\ & & 6\omega_o^2 \end{bmatrix}, \lambda_3 = \begin{bmatrix} 4\omega_o & & \\ & 4\omega_o & \\ & & 4\omega_o \end{bmatrix}.$$

Then the passivity-based controller for the tracking error dynamics (5.10) is obtained as [78]:

$$\tau = -\mathbf{K}_d(\dot{\hat{\mathbf{e}}}_1 + \Lambda \mathbf{e}) - \hat{\mathbf{w}}_1 = -\mathbf{K}_d \mathbf{s} + \mathbf{K}_d \dot{\hat{\mathbf{e}}} - \hat{\mathbf{w}}_1, \quad (5.16)$$

where $\dot{\hat{\mathbf{e}}} = \dot{\mathbf{e}} - \dot{\hat{\mathbf{e}}}_1$.

Combining (5.10) and (5.16), the closed-loop tracking error dynamic equation is as

$$\mathbf{M}\dot{\mathbf{s}} + \mathbf{C}\mathbf{s} + \mathbf{D}\mathbf{s} + \mathbf{K}_d \mathbf{s} = \mathbf{K}_d \dot{\hat{\mathbf{e}}} + \tilde{\mathbf{w}}, \quad (5.17)$$

where $\tilde{\mathbf{w}} = \mathbf{w} - \hat{\mathbf{w}}_1$. By following the proof in [78], it can be obtained that $\dot{\hat{\mathbf{e}}}$ and $\tilde{\mathbf{w}}$ are bounded.

Finally, since τ is virtual control input, the real control input of the proposed trajectory tracking controller is given as follows:

$$\mathbf{u} = \mathbf{B}^{-1}(-\mathbf{K}_d(\dot{\hat{\mathbf{e}}}_1 + \Lambda \mathbf{e}) - \hat{\mathbf{w}}_1). \quad (5.18)$$

In the proposed controller (5.18), it is seen that, the only required information of the robot dynamic model is the matrix \mathbf{B} . In other words, only the average contact radius L_a should be obtained to implement (5.18). Moreover, since the robot model information is also not used in the implementation of observer (5.13), the designed whole control system only requires the average contact radius L_a . As a result, compared with the RAC in Chapter 3 and GPI observer based control in Chapter 4, the tedious dynamic parameter identification process can be avoided. In addition, only the position feedback signal is needed without measurements of the velocity signal.

As already mentioned before, since the robot prototype is a fully-damped dynamic system, the damping injection may be avoided. This is because the motor gear reduction ratio of our robot prototype is large ($n = 186$) and the damping force of the robot itself $\mathbf{D}\dot{\mathbf{q}}$

is enough. The calculated results of \mathbf{D} of our robot prototype is:

$$\mathbf{D} = \begin{bmatrix} 144.4 & & \\ & 144.4 & \\ & & 10.6 \end{bmatrix}.$$

In other words, \mathbf{K}_d may be set quite small or even zero in practice, and thus the velocity measurement or estimation ($\dot{\mathbf{e}}_1$) may become unnecessary.

Remark 1. It can be observed that the virtual control input $\boldsymbol{\tau}$ and inertia matrix \mathbf{M} are not involved in the modified GPI observer (5.13). This is different with GPI observer in Chapter 4, wherein both the control input and inertia matrix are indispensable.

5.2.2 Stability Analysis

Defining $\boldsymbol{\psi} = \mathbf{K}_d \dot{\mathbf{e}} + \tilde{\mathbf{w}}$, the closed-loop tracking error dynamic equation can be rewritten as

$$\mathbf{M}\dot{\mathbf{s}} + \mathbf{C}\mathbf{s} + \mathbf{D}\mathbf{s} + \mathbf{K}_d\mathbf{s} = \boldsymbol{\psi}, \quad (5.19)$$

The closed-loop stability of (5.19) can be guaranteed by the following theorem.

Theorem 1 [65] : Let \mathbf{q}_d be a given twice differentiable function. Consider the closed-loop tracking error dynamic equation (5.19), \mathbf{s} is given by

$$\mathbf{s} = \mathbf{F}(s)^{-1}\mathbf{e},$$

where $\mathbf{F}(s)$ is strictly proper, stable and the mapping from $-\mathbf{s}$ to $\boldsymbol{\psi}$ is passive, i.e.,

$$\int_0^T -\mathbf{s}^T \boldsymbol{\psi} dt \geq -\mu,$$

for all T and for some $\mu \geq 0$. Then $\mathbf{e} \in L_2^3 \cap L_\infty^3$, \mathbf{e} is continuous and $\mathbf{e} \rightarrow 0$ as $t \rightarrow \infty$. In addition, if $\boldsymbol{\psi}$ is bounded, then $\mathbf{s} \rightarrow 0$ as $t \rightarrow \infty$, and consequently, $\dot{\mathbf{e}} \rightarrow 0$.

It can be verified that the mapping from $-\mathbf{s}$ to $\boldsymbol{\psi}$ is output strictly passive. As a result, it can be obtained from Theorem 1 that both \mathbf{e} and $\dot{\mathbf{e}}$ converge to 0 as $t \rightarrow \infty$, since $\boldsymbol{\psi} = \mathbf{K}_d \dot{\mathbf{e}} + \tilde{\mathbf{w}}$ is bounded.

For the detailed proof of the above theorem, the readers are referred to [65].

Table 5.1: Experimental results: IAE of average dynamic model based RAC, GPI observer based control, and passivity based MFC

Trajectory	Circle		Square		Lemniscate	
IAE	$IAE_{xy}(\text{m})$	$IAE_{\theta}(\text{rad})$	$IAE_{xy}(\text{m})$	$IAE_{\theta}(\text{rad})$	$IAE_{xy}(\text{m})$	$IAE_{\theta}(\text{rad})$
RAC	0.979	1.972	0.800	1.074	0.646	1.360
GPI	0.103	0.153	0.182	0.192	0.115	0.158
MFC	0.360	0.202	0.551	0.407	0.432	0.177

5.3 Experiments and Discussions

5.3.1 Tracking Performance

In this section, experimental results are shown to compare the tracking performances of the proposed three control methods in this thesis, i.e., average dynamic model based RAC, GPI observer based control and passivity based MFC in this chapter. The three typical trajectories used in the previous chapters are employed as the reference trajectories.

The controller parameters for the average dynamic model based RAC are set as:

$$\mathbf{K}_p = \begin{bmatrix} 16 & & \\ & 16 & \\ & & 16 \end{bmatrix}, \quad \mathbf{K}_d = \begin{bmatrix} 40 & & \\ & 40 & \\ & & 40 \end{bmatrix}. \quad (5.20)$$

The controller and observer parameters for the GPI observer based control are set as: $\omega_c = 4 \text{ rad/s}$, $\xi = 5$, $\omega_o = 16 \text{ rad/s}$. In other words, the \mathbf{K}_p and \mathbf{K}_d are set as:

$$\mathbf{K}_p = \begin{bmatrix} 16 & & \\ & 16 & \\ & & 16 \end{bmatrix}, \quad \mathbf{K}_d = \begin{bmatrix} 40 & & \\ & 40 & \\ & & 40 \end{bmatrix}. \quad (5.21)$$

The controller and observer parameters of passivity based MFC are set as:

$$\mathbf{K}_d = \begin{bmatrix} 1 & & \\ & 1 & \\ & & 1 \end{bmatrix}, \quad \mathbf{\Lambda} = \begin{bmatrix} 16 & & \\ & 16 & \\ & & 4 \end{bmatrix}. \quad (5.22)$$

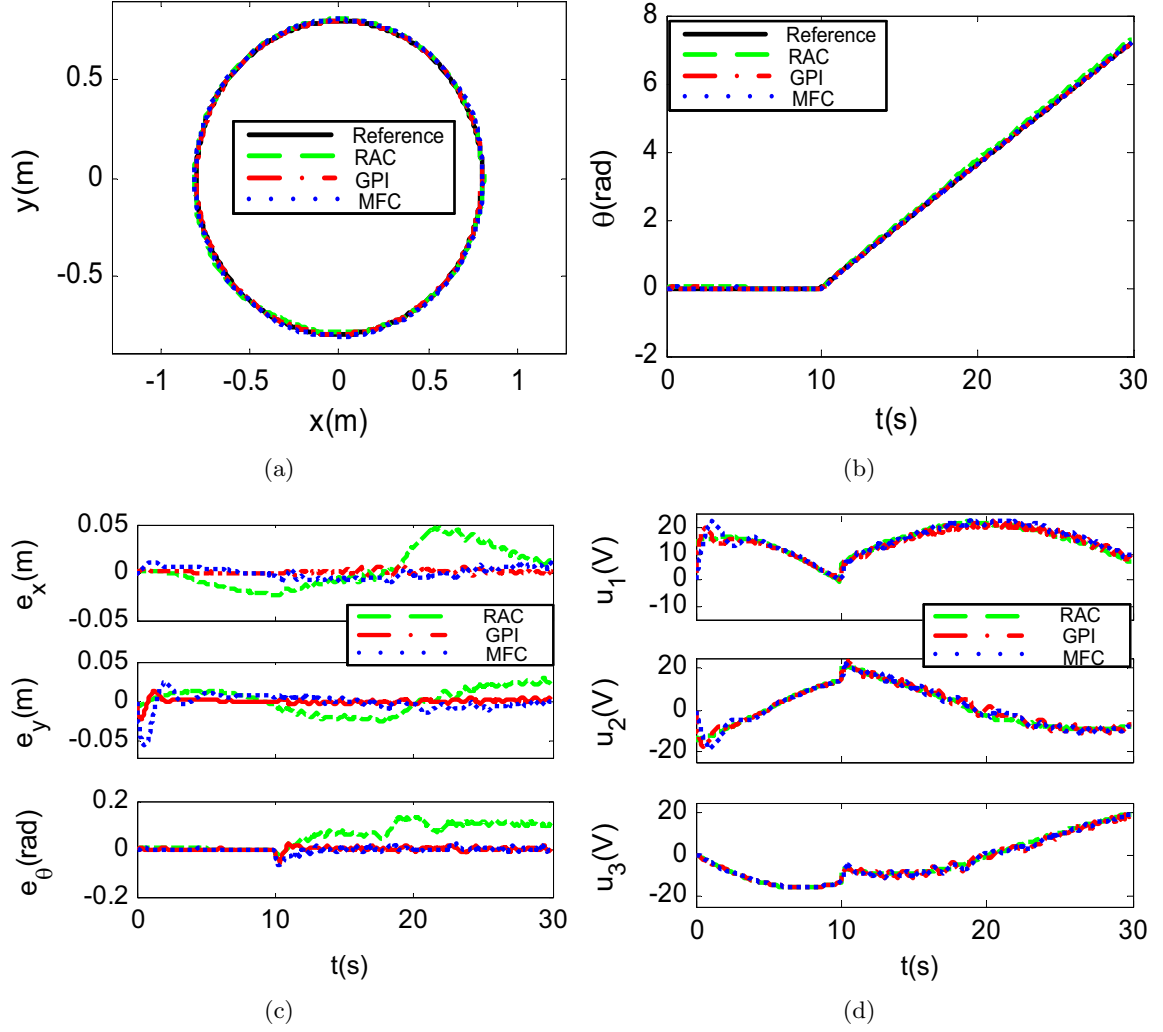


Figure 5.2: Experimental results of average dynamic model based RAC, GPI observer based control and passivity based MFC (circle trajectory): (a) Circle trajectory in the xy-plane: reference trajectory and responses. (b) Circle trajectory in the orientation direction: reference trajectory and responses. (c) Tracking errors. (d) Control input $\mathbf{u}(t)$.

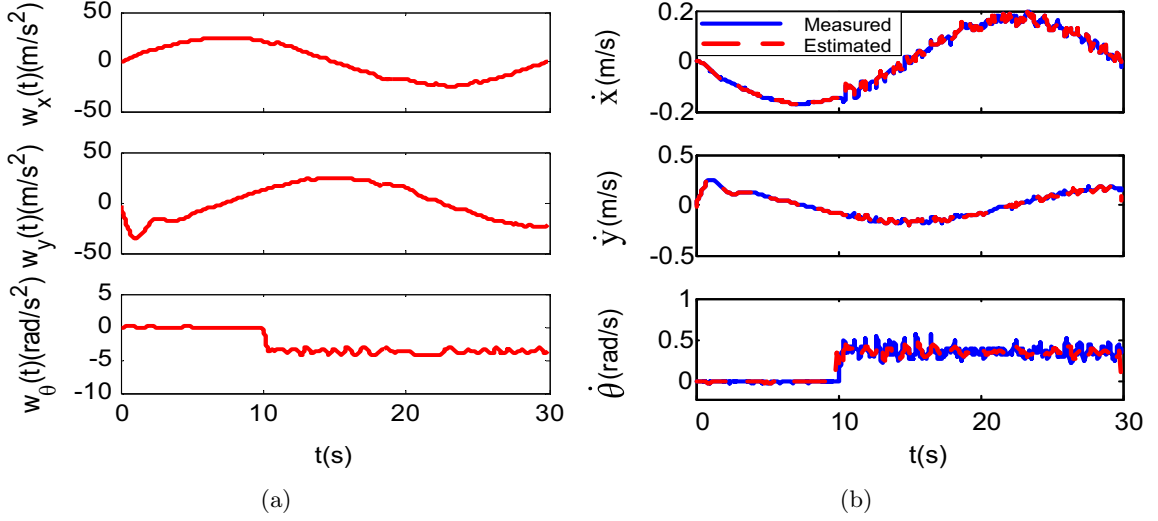


Figure 5.3: Experimental results of passivity based MFC (circle trajectory): (a) Estimation of perturbation input vector by the GPI observer $\hat{\mathbf{w}}$. (b) Measured robot velocity and its estimation by the modified GPI observer.

Note that $\mathbf{K}_p = \mathbf{K}_d \mathbf{\Lambda}$. The observer gains for the x and y channel are set as $\omega_o = 16$ rad/s, and the observer gain for the rotational channel is set as $\omega_o = 4$ rad/s. We reduce the observer gain for the rotational channel to avoid noises in the control signal. It is found in our experiments that if the observer gain for the rotational channel is set as $\omega_o = 16$ rad/s, severe noises will be introduced into the control signal.

It is seen that the selection of \mathbf{K}_d in the passivity based MFC (5.22) is very small compared with the other two control methods. In fact, the selection of \mathbf{K}_d can be further smaller. It is known that the effect of \mathbf{K}_d is to add damping forces to the control system. However, the robot prototype itself already has enough damping forces, which is reflected by $\mathbf{D}\mathbf{s}$ in (5.19). Therefore, it works for our robot prototype even though the parameter \mathbf{K}_d is selected very small. In fact, it is shown in our experiments that \mathbf{K}_d in (5.22) can be set as zero. For the average dynamic model based RAC and GPI observer based control, the parameter \mathbf{K}_d should be selected large enough, since the damping forces of the robot itself $\mathbf{D}\dot{\mathbf{q}}$ are canceled in both controllers. If these two control systems use the same \mathbf{K}_d as that

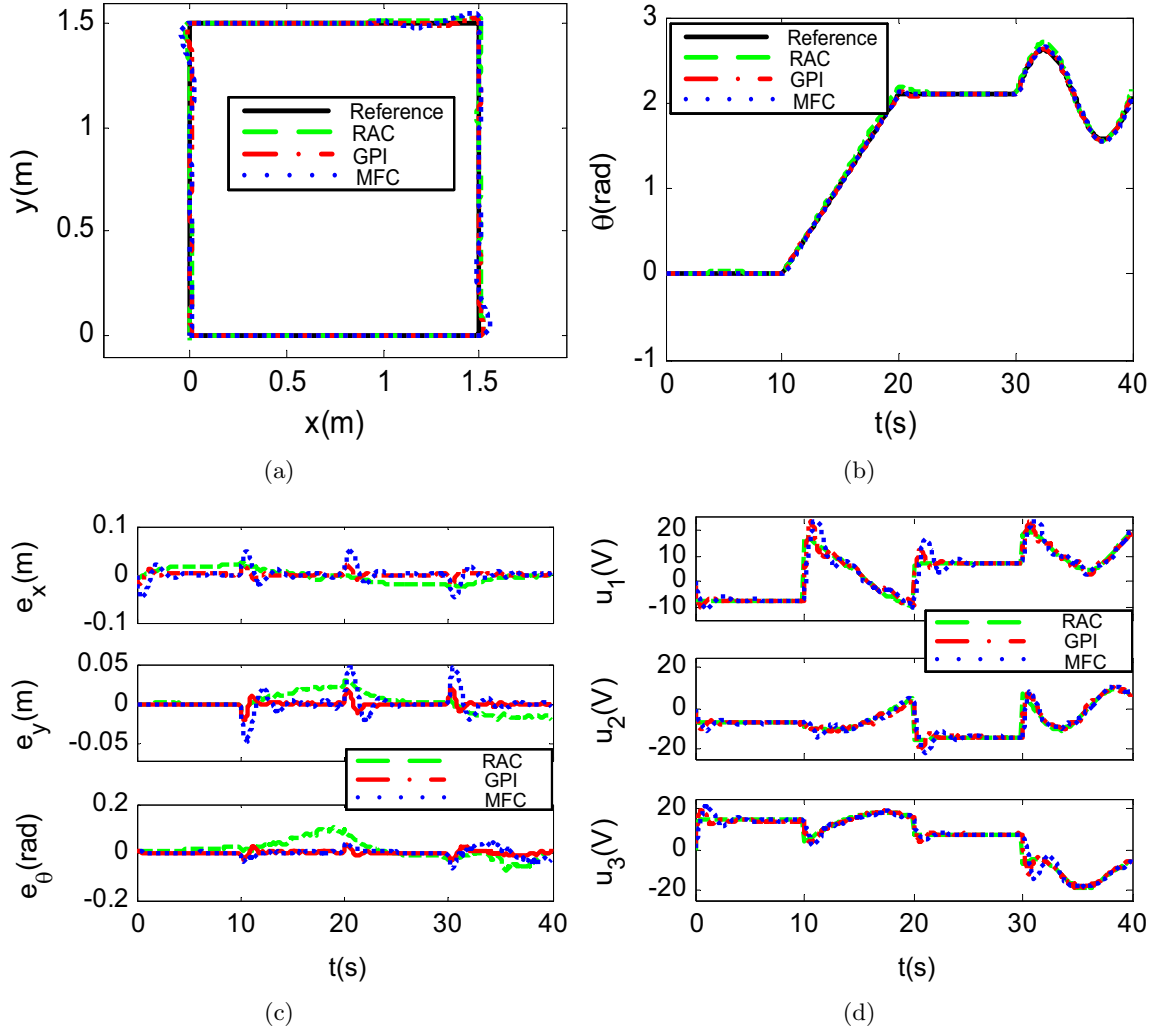


Figure 5.4: Experimental results of average dynamic model based RAC, GPI observer based control and passivity based MFC (square trajectory): (a) Square trajectory in the xy -plane: reference trajectory and responses. (b) Square trajectory in the orientation direction: reference trajectory and responses. (c) Tracking errors. (d) Control input $\mathbf{u}(t)$.

of passivity based MFC, it is found in our experiments that both control systems cannot work and will have severe oscillations.

Experimental results are shown in Figure 5.2 - Figure 5.5. The IAE of average dynamic model based RAC, GPI observer based control and passivity based MFC is shown in Table 5.1. Note that for each experiment, we conducted three times and Table 5.1 shows the

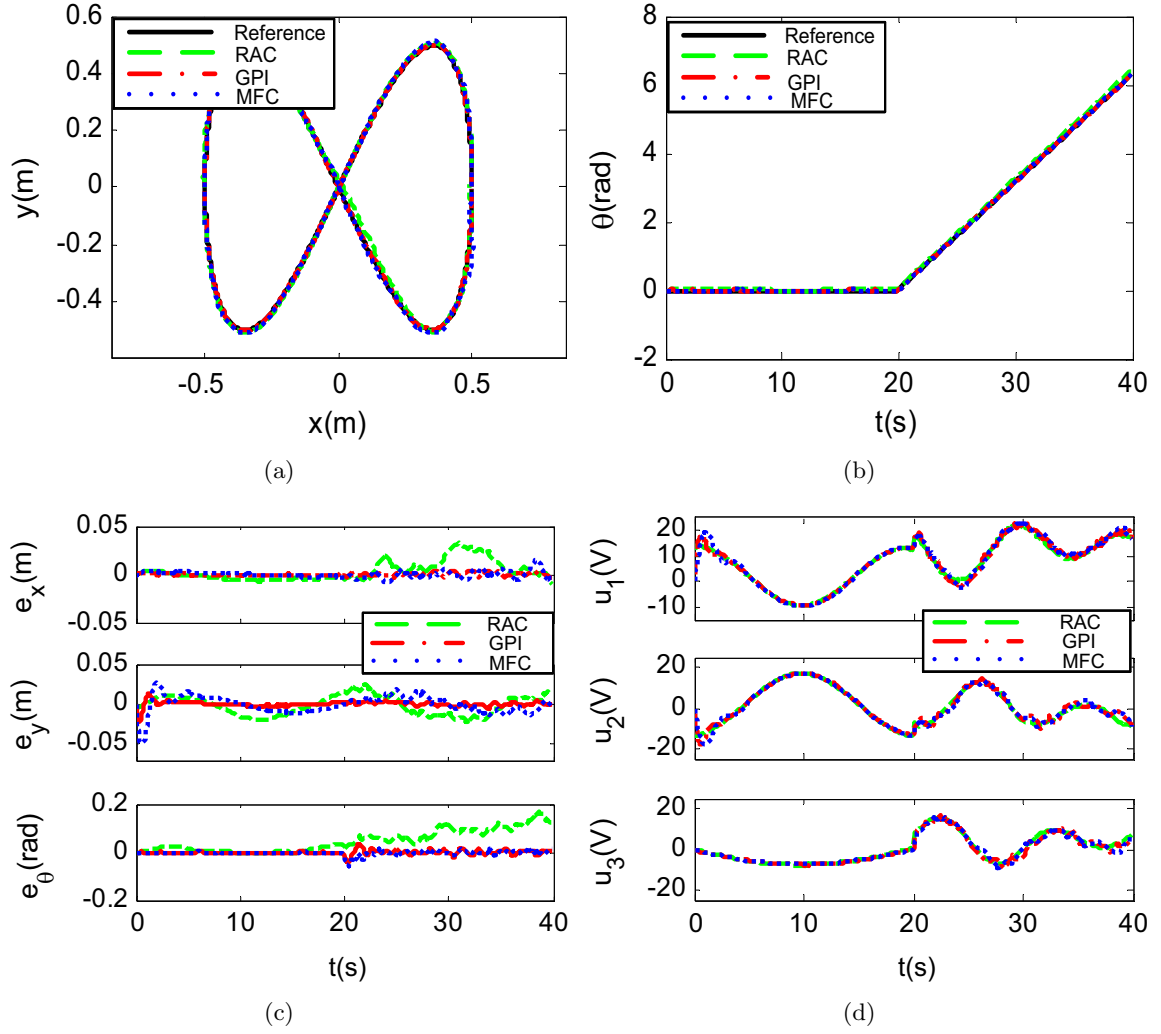


Figure 5.5: Experimental results of average dynamic model based RAC, GPI observer based control and passivity based MFC (lemniscate trajectory): (a) Lemniscate trajectory in the xy-plane: reference trajectory and responses. (b) Lemniscate trajectory in the orientation direction: reference trajectory and responses. (c) Tracking errors. (d) Control input $\mathbf{u}(t)$.

average results. The original experimental data of the experiments is shown in Appendix D.

It is shown in the three experimental tests that the IAE of GPI observer based control is smaller than the other two control methods in both translational and rotational motion. Therefore, GPI observer based control achieves the best tracking performances. The performances of passivity based MFC are a bit lower than GPI observer based control, but much

better than average dynamic model based RAC. It should be noted that passivity based RAC does not require any dynamic model information of the robot. The performances of average dynamic model based RAC can be further improved by improving the accuracy of the model, such as considering the Coulomb and Viscous friction forces.

However, since GPI observer based control and passivity based MFC are observer based control, one problem of both control designs is that the transient tracking errors are larger than average dynamic model based RAC, when sudden changes exist in the position and velocity of the robot. Especially, passivity based MFC has the largest transient tracking errors, as shown in Figure 5.4. This is due to the transient responses of the observer, and is one disadvantage of observer based control approaches compared with average model based RAC. As a result, the transient tracking errors of GPI observer based control or passivity based MFC may be reduced by switching observer based control and average dynamic model based RAC.

Moreover, the estimated disturbance $\hat{\mathbf{w}}$ by the modified GPI observer is shown in Figure 5.3 (a). It is shown in Figure 5.3 (b) that the robot velocity can be well estimated by the modified GPI observer.

5.3.2 Robustness

Finally, both simulations and experiments are conducted to compare the robustness of the three control methods above. Since the gear reduction ratio of the motors in our robot prototype is large ($n = 186$), a lemniscate trajectory with low speed is selected to show the robustness in both simulations and experiments. The reference lemniscate trajectory is set as: $x_d = 0.4 \cos(\frac{\pi}{40}t)$ m; $y_d = 0.4 \sin(\frac{\pi}{20}t)$ m. The robot initial posture is set as $\begin{bmatrix} 0.4 \text{ (m)} & 0 \text{ (m)} & 0 \text{ (rad)} \end{bmatrix}^T$. In the first 40 s, the robot orientation is fixed, i.e., $\theta_d = 0$ rad. After 40 s, the desired orientation angle is $\theta_d = \frac{\pi}{40}(t - 40)$ rad.

Two kinds of simulations are conducted. The first kind of simulation is conducted without introducing disturbances. The other kind is with disturbances, in which the disturbance is added into the control system after 60 s. The mass and moment of inertia of the robot

Table 5.2: Simulation results: comparisons of robustness of the three control methods.

IAE	$IAE_{xy}^{WT}(\text{m})$	$IAE_{xy}^W(\text{m})$	$P_{xy}(\%)$	$IAE_{\theta}^{WT}(\text{rad})$	$IAE_{\theta}^W(\text{rad})$	$P_{\theta}(\%)$
RAC	0.183	0.289	58.21	0.307	0.411	33.87
GPI	0.054	0.057	5.21	0.083	0.087	4.8
MFC	0.208	0.214	3.23	0.197	0.205	3.81

are changed as 20 times of the original ones, i.e., $m = 700 \text{ kg}$, $I_v = 27 \text{ kg} \cdot \text{m}^2$. In addition, the parameter b_0 is changed as $b_0 = 2.5 \times 10^{-4} \text{ Nms/rad}$. Simulation results are shown in Figure 5.6 - Figure 5.8. It is seen that the performances of average dynamic model based RAC are severely decreased due to the disturbance after 60 s, while the performances of GPI observer based control and passivity based MFC are maintained almost the same even after 60 s. This is because the disturbances can be estimated by the observer and compensated in the control signal. Table 5.2 shows the comparisons of robustness of the three control methods. IAE_{xy}^{WT} and IAE_{θ}^{WT} are the IAE of the tracking performance without disturbances. IAE_{xy}^W and IAE_{θ}^W are the IAE of the tracking performance with disturbances. We use P_{xy} and P_{θ} to evaluate the robustness of three control methods, which are defined as: $P_{xy} = \frac{IAE_{xy}^W - IAE_{xy}^{WT}}{IAE_{xy}^{WT}}$ and $P_{\theta} = \frac{IAE_{\theta}^W - IAE_{\theta}^{WT}}{IAE_{\theta}^{WT}}$, respectively.

It can be seen from Table 5.2 that, the performances of the average dynamic model based RAC have a large decrease compared with the other two control methods. Therefore, the robustness of GPI observer based control and passivity based MFC is much better than that of average dynamic model based RAC. It is also observed that the robustness of passivity based MFC is a bit better than that of GPI observer based control. This may be due to the fact that the equivalent gains of passivity based MFC of the closed-loop system are much higher than those of GPI observer based control. More specifically, although the proportional gain \mathbf{K}_p is set as the same for both control methods (see (5.21) and (5.22)), it can be calculated that the equivalent gains of passivity based MFC of the closed-loop system is much higher than those of GPI observer based control.

In addition, experimental tests are conducted to compare the robustness of the three control methods. The same reference trajectory used in the simulations is employed in

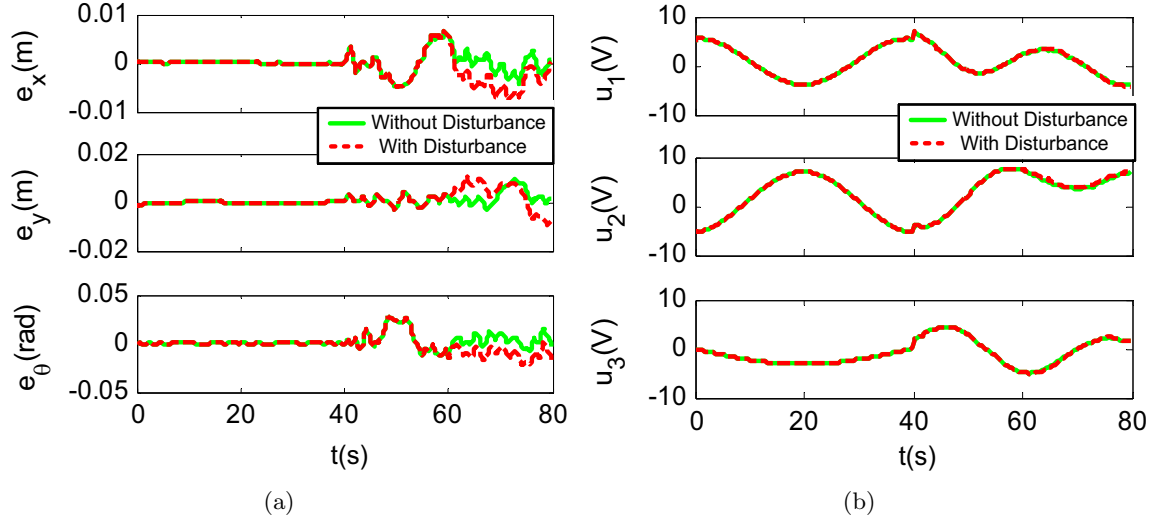


Figure 5.6: Simulation results of robustness of average dynamic model based RAC: (a) Tracking errors with and without disturbance, respectively. (b) Control input $\mathbf{u}(t)$ with and without disturbance, respectively.

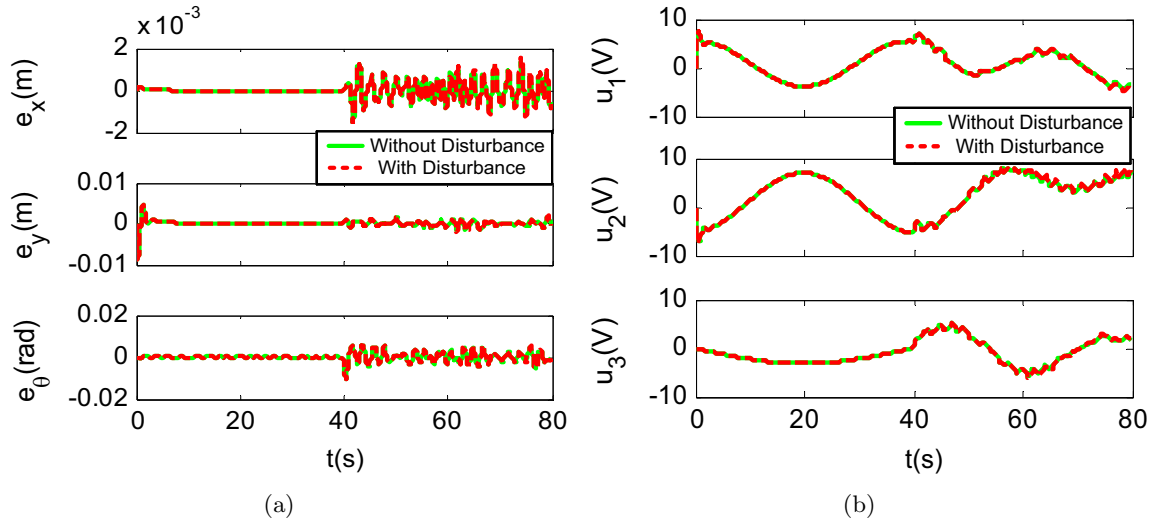


Figure 5.7: Simulation results of robustness of GPI observer based control: (a) Tracking errors with and without disturbance, respectively. (b) Control input $\mathbf{u}(t)$ with and without disturbance, respectively.

experiments. We installed a chair on the robot prototype (see Figure 5.9). After 60s, the disturbance is introduced into the system by adding a people (weight: 67 Kg) on the chair. Therefore, the robot mass, moment of inertia, and friction forces are changed. In addition,

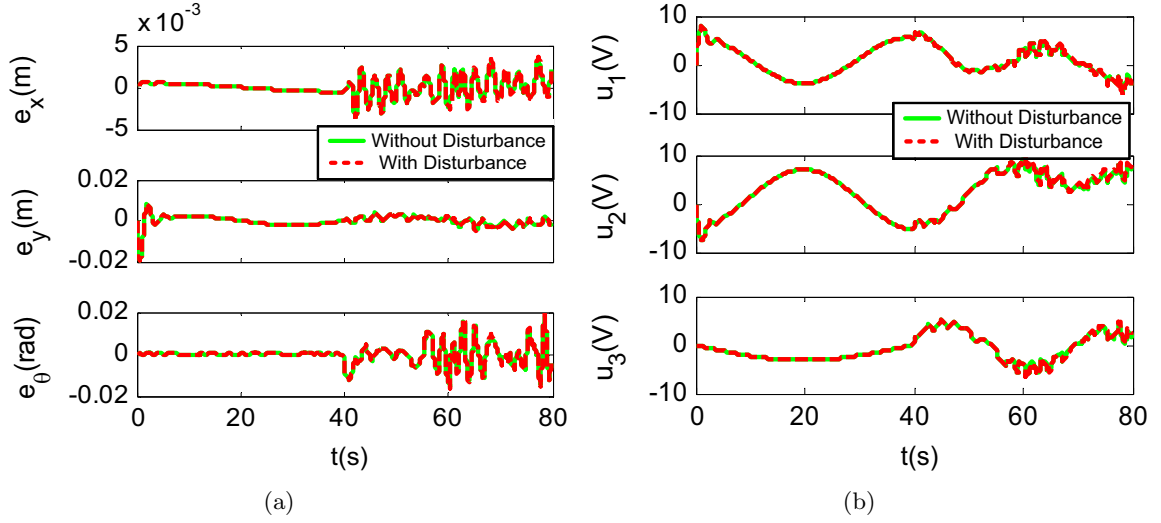


Figure 5.8: Simulation results of robustness of passivity based MFC: (a) Tracking errors with and without disturbance, respectively. (b) Control input $\mathbf{u}(t)$ with and without disturbance, respectively.

Table 5.3: Experimental results: comparisons of robustness of the three control methods.

IAE	IAE_{xy}^{WT} (m)	IAE_{xy}^W (m)	P_{xy} (%)	IAE_θ^{WT} (rad)	IAE_θ^W (rad)	P_θ (%)
RAC	0.786	1.174	49.29	0.989	1.340	35.40
GPI	0.070	0.077	9.81	0.091	0.114	26.49
MFC	0.230	0.243	5.50	0.101	0.125	24.25

the experiments are conducted on a rubber floor, to increase the friction forces which are also disturbances to the control system (see Figure 5.9). Experimental results are shown in Figure 5.10 - Figure 5.12. The comparisons of the experimental results are shown in Table 5.3, which is the average of the experimental results. We conducted each experiment for three times, and the original data is shown in Appendix D.

From Figure 5.10 - Figure 5.12, it can be seen that the control performances of average dynamic model based RAC have large deviations after disturbance is introduced, compared with the performances without disturbance. However, for GPI observer based control and passivity based MFC, the performances have a little bit change after the introduction of disturbance. It is seen from Table 5.3 that, the robustness of passivity based MFC is the

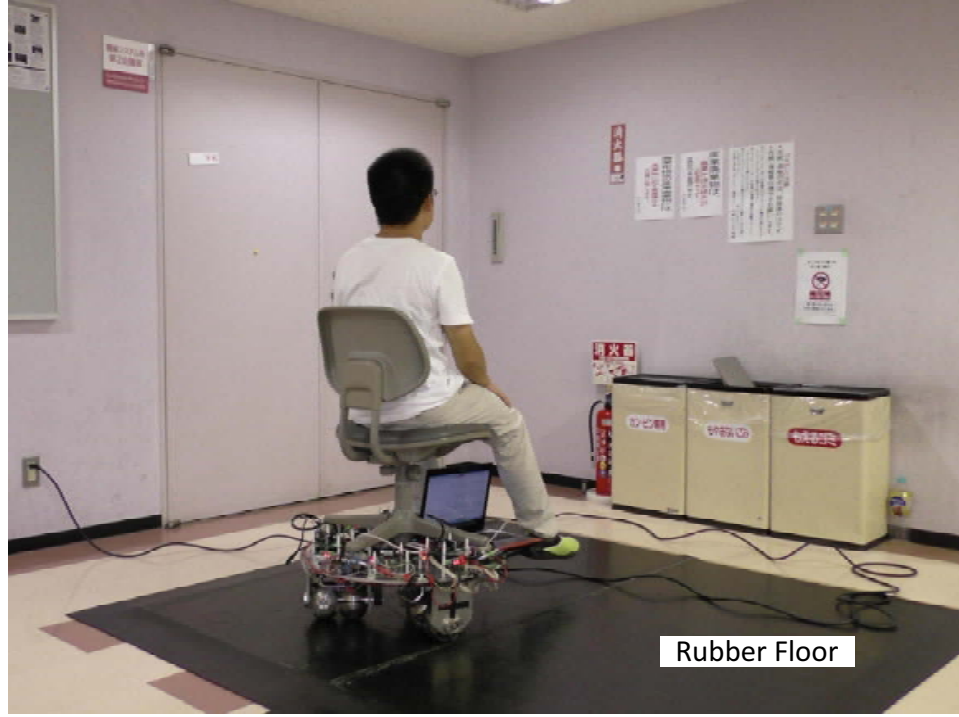


Figure 5.9: Experimental setup of the robust tests.

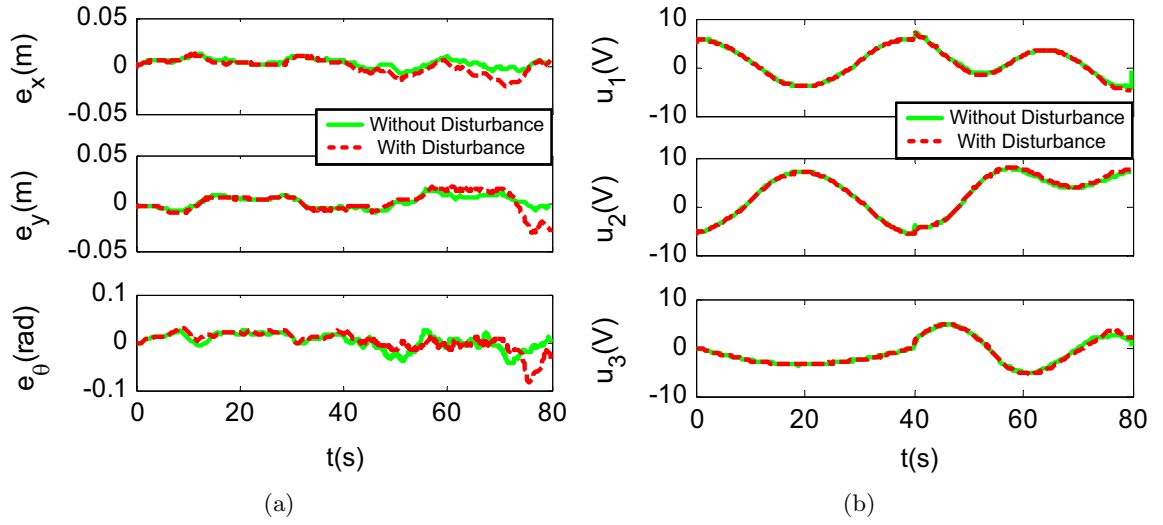


Figure 5.10: Experimental results of robustness of average dynamic model based RAC: (a) Tracking errors with and without disturbance, respectively. (b) Control input $\mathbf{u}(t)$ with and without disturbance, respectively.

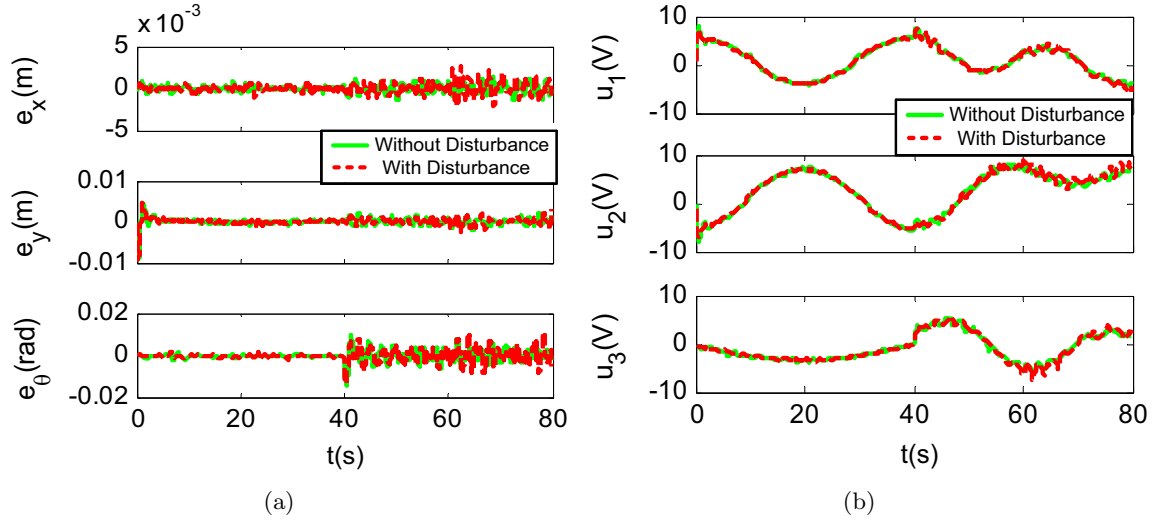


Figure 5.11: Experimental results of robustness of GPI observer based control: (a) Tracking errors with and without disturbance, respectively. (b) Control input $\mathbf{u}(t)$ with and without disturbance, respectively.

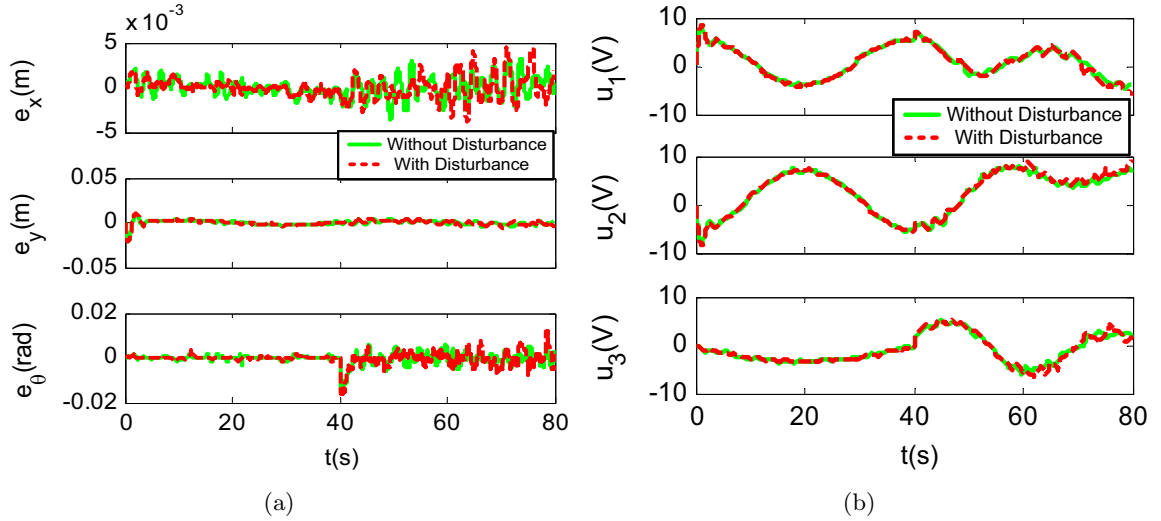


Figure 5.12: Experimental results of robustness of passivity based MFC: (a) Tracking errors with and without disturbance, respectively. (b) Control input $\mathbf{u}(t)$ with and without disturbance, respectively.

best and the robustness of average dynamic model based RAC is the worst. GPI observer based control achieves a bit lower robust performances compared with passivity based MFC. Therefore, the experimental results have a good agreement with simulation results.

5.3.3 Discussions

In this part, comparisons of the three control methods are briefly summarized and discussed from the following five aspects:

(1) Control performances. The GPI observer based control in Chapter 4 achieves the best control performances among the three control approaches. The performances of passivity based MFC are a bit lower than GPI observer based control. This may be due to the fact that the estimation performance of modified GPI observer in Chapter 5 is lower than the GPI observer in Chapter 4. Average dynamic model based RAC achieves the worst performances. However, the control performances of average dynamic model based RAC can be improved by using a more accurate dynamic model.

One problem of both GPI observer based control and passivity based MFC is that, the transient tracking errors are larger than average dynamic model based RAC, when sudden changes exist in the position and velocity of the robot. This is due to the transient response of the observer. Note that the transient tracking errors of passivity based MFC are more severe than GPI observer based control. Moreover, the transient tracking errors of GPI observer based control or passivity based MFC may be reduced by switching observer based control and average dynamic model based RAC.

(2) Robustness. Passivity based MFC achieves the best robust performances. The robust performances of GPI observer based control are a bit lower than passivity based MFC. Average dynamic model based RAC achieves the lowest robust performances, since the disturbances cannot be estimated and compensated in real time.

(3) Model information. The passivity based MFC only needs one parameter, i.e., average contact radius of the robot. It does not need the robot dynamic information, and thus the dynamic model is not required. For the GPI observer based control, part of the dynamic model information is needed, i.e., \mathbf{M}_{av} and \mathbf{B}_{av} (see (3.1)). It also does not require the exact value of \mathbf{M}_{av} and \mathbf{B}_{av} , since the errors can be also considered as disturbances and can

be estimated in the GPI observer. However, average dynamic model based RAC requires complete model information to guarantee its control performances.

(4) Feedback signal. Both the GPI observer based control and passivity based MFC only require the robot position in the feedback, since the robot velocity can be estimated by both observers. Therefore, these two control methods are output feedback control systems. On the other hand, average dynamic model based RAC requires both robot position and velocity measurements, which is a state feedback control system.

(5) Parameter tuning. In our experimental tests, all of the above three control methods are easy to be tuned. For average dynamic model based RAC, it is the same as parameter tuning of a second order SISO system. For GPI observer based control, the controller gain ω_c and observer gain ω_o are usually chosen as $\omega_o = (3 \sim 5)\omega_c$. Therefore, the parameter tuning can start from a small ω_c and then increase it step by step. For the passivity based MFC, the parameter can be tuned with only PD feedback control firstly, i.e., without modified GPI observer. When the parameter is well tuned with PD feedback control, then the parameter can be tuned by adding the modified GPI observer. However, since passivity based MFC results in a coupled closed-loop system, the parameter tuning may become somewhat difficult if the coupling term has significant effects.

5.4 Summary

In this chapter, a passivity based MFC design has been proposed by employing a modified GPI observer. Firstly, the passivity property of our robot prototype has been analyzed based on the average dynamic model (3.1). It is shown in analysis that the robot prototype itself has enough damping forces. The damping forces are proportional to the gear reduction ratio of the motor. Different from the feedback linearization control approaches, the passivity-based MFC design is to preserve the passivity property of the robot in the closed-loop system. In the proposed control design, the required information is only the average contact radius (L_a). Stability property has been analyzed based on the average dynamic

model. In the parameter tuning of passivity based MFC, it is found that the controller works well even for quite small \mathbf{K}_d , thanks to the damping forces of the robot itself.

Finally, experimental tests have been conducted to compare with the control designs in previous chapters. Discussions about the three control designs have also been presented from the following five points, i.e., (1) control performances, (2) robustness, (3) model information, (4) feedback signal and (5) parameter tuning.

Chapter 6

Conclusion and Future Work

6.1 Conclusion

In this thesis, the trajectory tracking control system design has been studied for a robot prototype with MY wheel-II. MY wheel-II is a switch wheel mechanism. Three trajectory tracking control system design methods, i.e., continuous dynamic model based RAC, GPI observer based control and passivity based MFC, have been proposed. Dynamic modeling and analysis have been conducted. It shows that our robot prototype is an autonomous switched nonlinear system, which consists of eight nonlinear smooth subsystems.

Firstly, continuous dynamic model based RAC has been studied. To facilitate the control system design, we have derived two continuous dynamic models, i.e., average dynamic model and NLPV dynamic model. The average dynamic model does not need the switching signal while the NLPV dynamic model requires the exact switching information. RAC has been employed to design controllers based on both continuous dynamic models. We only conducted average dynamic model based RAC in the experiments.

Then, GPI observer based control has been proposed based on the average dynamic model, to compensate the modeling errors of average dynamic model and to improve the control performances. In this approach, all of the modeling errors (such as switching dynamics, unmodeled forces, parameter uncertainties, etc.), as well as the input-output cross

coupling effects are considered as an unknown time-varying perturbation input vector. It is then online estimated by the GPI observer and compensated in the control signal. BIBO stability is guaranteed for the closed-loop system.

To further reduce the model information used in the GPI observer based control, a passivity based MFC has proposed based on a modified GPI observer. The objective is to design a controller such that the passivity property of the robot is preserved in the closed-loop system by using the modified GPI observer. The robot geometrical information is the only required model information. Moreover, stability analysis has been conducted based on the average dynamic model. Finally, experiments of the above three control designs have been conducted to compare their control performances and robustness, which can be briefly summarized as follows:

(1) Control performances. The GPI observer based control in Chapter 4 achieves the best control performances among the three control approaches. The performances of passivity based MFC are a bit lower than GPI observer based control. Average dynamic model based RAC achieves the worst performances.

One problem of both GPI observer based control and passivity based MFC is that, the transient tracking errors are larger than average dynamic model based RAC, when sudden changes exist in the position and velocity of the robot. The transient tracking errors of GPI observer based control or passivity based MFC may be reduced by switching observer based control and average dynamic model based RAC.

(2) Robustness. Passivity based MFC achieves the best robust performances. The robust performances of GPI observer based control are a bit lower than passivity based MFC. Average dynamic model based RAC achieves the lowest robust performances, since the disturbances cannot be estimated and compensated in real time.

(3) Model information. The passivity based MFC only needs the average contact radius of the robot. For the GPI observer based control, part of the dynamic model information is needed. Average dynamic model based RAC requires complete model information.

(4) Feedback signal. Both the GPI observer based control and passivity based MFC only require the robot position in the feedback while average dynamic model based RAC requires both robot position and velocity measurements.

(5) Parameter tuning. In our experimental tests, all of the above three control methods are easy to be tuned. There are three parameters to be tuned in both GPI observer based control and passivity based MFC, respectively. Only two control parameters are in the average dynamic model based RAC. However, since passivity based MFC results in a coupled closed-loop system, the parameter tuning may become somewhat difficult if the coupling term has significant effects.

6.2 Future Work

To further improve the control performances, many works are necessary to be conducted. For example:

- A more accurate dynamic model should be derived including the Viscous and Coulomb frictions, to improve the performances of continuous dynamic model based RAC.
- Even though the GPI observer based control achieves the best performances, the transient tracking errors are large when the robot suffers from sudden changes in the robot state. However, the transient tracking errors of average dynamic model based RAC are small. Therefore, switching control may be studied by combining the two control approaches.

Bibliography

- [1] P. F. Muir and C. P. Neuman, “Kinematic modeling of wheeled mobile robots,” *J. Robot. Syst.*, vol. 4, no. 2, pp. 281–340, 1987.
- [2] B. Ilou, “Wheels for a course stable self-propelling vehicle movable in any desired direction on the ground or some other base,” Patent U.S. Patent 3 876 255, Apr 8, 1975.
- [3] K.-S. Byun and J.-B. Song, “Design and construction of continuous alternate wheels for an omnidirectional mobile robot,” *J. Robot. Syst.*, vol. 20, no. 9, pp. 569–579, 2003.
- [4] J.-B. Song and K.-S. Byun, “Design and control of a four-wheeled omnidirectional mobile robot with steerable omnidirectional wheels,” *J. Robot. Syst.*, vol. 21, no. 4, pp. 193–208, 2004.
- [5] K. Tadakuma and R. Tadakuma, “Mechanical design of “omni-ball”: spherical wheel for holonomic omnidirectional motion,” in *Proc. of the 2007 IEEE Int. Conf. on Automation Science and Engineering (CASE)*, Arizona, USA, Sept. 2007, pp. 788 –794.
- [6] F. Pin and S. Killough, “A new family of omnidirectional and holonomic wheeled platforms for mobile robots,” *IEEE Trans. Robot. Autom.*, vol. 10, no. 4, pp. 480 –489, 1994.
- [7] C. Ye and S. Ma, “Development of an omnidirectional mobile platform,” in *Proc. of the 2009 IEEE Int. Conf. Mechatronics and Automation*, Changchun, China, Aug. 2009, pp. 1111 –1115.

- [8] S. Ma, C. Ren, and C. Ye, “An omnidirectional mobile robot: concept and analysis,” in *Proc. of the 2012 IEEE Int. Conf. Robotics and Biomimetics(ROBIO)* , Guangzhou, China, Dec. 2012, pp. 920–925.
- [9] G. Indiveri, “Swedish wheeled omnidirectional mobile robots: Kinematics analysis and control,” *IEEE Trans. Robot.*, vol. 25, no. 1, pp. 164 –171, 2009.
- [10] [Online]. Available: http://www.kuka-robotics.com/en/products/mobility/mobile_platform_omnimove/
- [11] [Online]. Available: http://www.kuka-robotics.com/en/products/mobility/KMR_QUANTEC/
- [12] [Online]. Available: http://www.dinf.ne.jp/doc/english/Us_Eu/conf/csun_99/session0274.html
- [13] [Online]. Available: <http://furo.org/en/works/wheelchair.html>
- [14] M. West and H. Asada, “Design and control of ball wheel omnidirectional vehicles,” in *Proc. of the 2013 IEEE/RSJ Int. Conf. on Robotics and Automation (ICRA)* , vol. 2, May 1995, pp. 1931 –1938.
- [15] M. Wada and H. Asada, “Design and control of a variable footprint mechanism for holonomic omnidirectional vehicles and its application to wheelchairs,” *IEEE Trans. Robot. Autom.*, vol. 15, no. 6, pp. 978 –989, Dec. 1999.
- [16] S. Ishida and H. Miyamoto, “Ball wheel drive mechanism for holonomic omnidirectional vehicle,” in *Proc. of the 2010 World Automation Congress (WAC)*, Kobe, Japan, Sept. 2010, pp. 1–6.
- [17] C. Ren and S. Ma, “Dynamic modeling and analysis of an omnidirectional mobile robot,” in *Proc. of the 2013 IEEE/RSJ Int. Conf. on Intelligent Robots and Systems (IROS)* , Tokyo, Japan, Nov. 2013, pp. 4860–4865.

- [18] H.-C. Huang and C.-C. Tsai, “Adaptive robust control of an omnidirectional mobile platform for autonomous service robots in polar coordinates,” *J. Intell. Robot. Syst.*, vol. 51, no. 4, pp. 439–460, 2008.
- [19] G. Mouriaux, C. Novales, G. Poisson, and P. Vieyres, “Omni-directional robot with spherical orthogonal wheels: concepts and analyses,” in *Proc. of the 2006 IEEE Int. Conf. Robotics and Automation (ICRA)*, Florida, USA, May 2006, pp. 3374–3379.
- [20] H.-C. Huang and C.-C. Tsai, “Simultaneous tracking and stabilization of an omnidirectional mobile robot in polar coordinates: a unified control approach,” *Robotica*, vol. 27, pp. 447–458, 2009.
- [21] K. Kanjanawanishkul and A. Zell, “Path following for an omnidirectional mobile robot based on model predictive control,” in *Proc. of 2009 IEEE Int. Conf. Robotics and Automation (ICRA)*, Kobe, Japan, May 2009, pp. 3341–3346.
- [22] C. Ye, H. Li, and S. Ma, “Kinematic analysis of an omnidirectional mobile robot with MY wheels,” in *Proc. of the 2011 IEEE Int. Conf. on Robotics and Biomimetics (ROBIO)*, Dec. 2011, pp. 1748–1753.
- [23] C.-C. Tsai, H.-C. Huang, and S.-C. Lin, “FPGA-based parallel DNA algorithm for optimal configurations of an omnidirectional mobile service robot performing fire extinguishment,” *IEEE Trans. Ind. Electron.*, vol. 58, no. 3, pp. 1016–1026, 2011.
- [24] C. Ren and S. Ma, “Predictive kinematic control of an omnidirectional mobile robot,” in *Proc. of the 2013 IEEE Int. Conf. on Robotics and Biomimetics (ROBIO)*, Dec. 2013, pp. 262–267.
- [25] K. Watanabe, Y. Shiraishi, S. Tzafestas, J. Tang, and T. Fukuda, “Feedback control of an omnidirectional autonomous platform for mobile service robots,” *J. Intell. Robot. Syst.*, vol. 22, pp. 315–330, 1998.
- [26] K.-Y. Tu, “A linear optimal tracker designed for omnidirectional vehicle dynamics

- linearized based on kinematic equations,” *Robotica*, vol. 28, no. 07, pp. 1033–1043, 2010.
- [27] J. C. L. Barreto S., A. G. S. Conceicao, C. E. T. Dorea, L. Martinez, and E. R. de Pieri, “Design and implementation of model-predictive control with friction compensation on an omnidirectional mobile robot,” *IEEE/ASME Trans. Mechatronics*, vol. 19, no. 2, pp. 467–476, 2014.
- [28] Y. Liu, J. J. Zhu, R. L. W. II, and J. Wu, “Omni-directional mobile robot controller based on trajectory linearization,” *Robot. Auton. Syst.*, vol. 56, no. 5, pp. 461 – 479, 2007.
- [29] O. Purwin and R. D’Andrea, “Trajectory generation and control for four wheeled omnidirectional vehicles,” *Robot. Auton. Syst.*, vol. 54, no. 1, pp. 13 – 22, 2006.
- [30] H.-C. Huang, C.-C. Tsai, and S.-C. Lin, “Adaptive polar-space motion control for embedded omnidirectional mobile robots with parameter variations and uncertainties,” *J. Intell. Robot. Syst.*, vol. 62, pp. 81–102, 2011.
- [31] J.-T. Huang, T. Hung, and M.-L. Tseng, “Smooth switching robust adaptive control for omnidirectional mobile robots,” *IEEE Trans. Control Syst. Technol.*, vol. PP, no. 99, pp. 1–1, 2015.
- [32] H. Sira-Ramírez, C. López-Urbe, and M. Velasco-Villa, “Linear observer-based active disturbance rejection control of the omnidirectional mobile robot,” *Asian J. Control*, vol. 15, no. 1, pp. 51–63, 2013.
- [33] D. Liberzon and A. Morse, “Basic problems in stability and design of switched systems,” *IEEE Control Syst. Mag.*, vol. 19, no. 5, pp. 59–70, 1999.
- [34] D. Liberzon, *Switching in Systems and Control*. Berlin, Germany: Birkhauser, 2003.
- [35] W. Dayawansa and C. Martin, “A converse lyapunov theorem for a class of dynamical systems which undergo switching,” *IEEE Trans. Autom. Control*, vol. 44, no. 4, pp. 751–760, 1999.

- [36] J. P. Hespanha and A. S. Morse, “Switching between stabilizing controllers,” *Automatica*, vol. 38, no. 11, pp. 1905–1917, 2002.
- [37] Z. Sun and S. S. Ge, “Analysis and synthesis of switched linear control systems,” *Automatica*, vol. 41, no. 2, pp. 181–195, 2005.
- [38] G. Deaecto, M. Souza, and J. Geromel, “Discrete-time switched linear systems state feedback design with application to networked control,” *IEEE Trans. Autom. Control*, vol. 60, no. 3, pp. 877–881, 2015.
- [39] C. Yuan and F. Wu, “Hybrid control for switched linear systems with average dwell time,” *IEEE Trans. Autom. Control*, vol. 60, no. 1, pp. 240–245, 2015.
- [40] N. H. El-Farra, P. Mhaskar, and P. D. Christofides, “Output feedback control of switched nonlinear systems using multiple lyapunov functions,” *Syst. Control. Lett.*, vol. 54, no. 12, pp. 1163 – 1182, 2005.
- [41] P. Mhaskar, N. El-Farra, and P. Christofides, “Predictive control of switched nonlinear systems with scheduled mode transitions,” *IEEE Trans. Autom. Control*, vol. 50, no. 11, pp. 1670–1680, 2005.
- [42] P. Mhaskar, N. H. El-Farra, and P. D. Christofides, “Stabilization of nonlinear systems with state and control constraints using lyapunov-based predictive control,” *Syst. Control. Lett.*, vol. 55, no. 8, pp. 650 – 659, 2006.
- [43] Q. Su, L. Long, and J. Zhao, “Stabilization of state-constrained switched nonlinear systems in p-normal form,” *Int. J. Robust. Nonlin.*, vol. 24, no. 10, pp. 1550–1562, 2014.
- [44] T.-T. Han, S. Sam Ge, and T. Heng Lee, “Adaptive neural control for a class of switched nonlinear systems,” *Syst. Control. Lett.*, vol. 58, no. 2, pp. 109–118, 2009.
- [45] R. Ma and J. Zhao, “Backstepping design for global stabilization of switched nonlinear systems in lower triangular form under arbitrary switchings,” *Automatica*, vol. 46, no. 11, pp. 1819 – 1823, 2010.

- [46] M. A. Müller, P. Martius, and F. Allgöwer, “Model predictive control of switched nonlinear systems under average dwell-time,” *J. Process. Contr.*, vol. 22, no. 9, pp. 1702–1710, 2012.
- [47] Y. Sun and L. Wang, “On stability of a class of switched nonlinear systems,” *Automatica*, vol. 49, no. 1, pp. 305 – 307, 2013.
- [48] J. Fu, R. Ma, and T. Chai, “Global finite-time stabilization of a class of switched nonlinear systems with the powers of positive odd rational numbers,” *Automatica*, vol. 54, no. 0, pp. 360 – 373, 2015.
- [49] M. Branicky, “Multiple lyapunov functions and other analysis tools for switched and hybrid systems,” *IEEE Trans. Autom. Control*, vol. 43, no. 4, pp. 475–482, 1998.
- [50] K. Koh and H. Cho, “A path tracking control system for autonomous mobile robots: an experimental investigation,” *Mechatronics*, vol. 4, no. 8, pp. 799 – 820, 1994.
- [51] Y. Chung, C. Park, and F. Harashima, “A position control differential drive wheeled mobile robot,” *IEEE Trans. Ind. Electron.*, vol. 48, no. 4, pp. 853–863, 2001.
- [52] S. X. Yang, A. Zhu, G. Yuan, and M.-H. Meng, “A bioinspired neurodynamics-based approach to tracking control of mobile robots,” *IEEE Trans. Ind. Electron.*, vol. 59, no. 8, pp. 3211–3220, Aug. 2012.
- [53] A. Conceicao, A. Moreira, and P. Costa, “Practical approach of modeling and parameters estimation for omnidirectional mobile robots,” *IEEE/ASME Trans. Mechatronics*, vol. 14, no. 3, pp. 377–381, 2009.
- [54] I. Williams, R.L., B. Carter, P. Gallina, and G. Rosati, “Dynamic model with slip for wheeled omnidirectional robots,” *IEEE Trans. Robot. Automat.*, vol. 18, no. 3, pp. 285–293, 2002.
- [55] B. Kouvaritakis and M. Cannon, *Non-linear Predictive Control: theory and practice*. London, U.K.: IEE, 2001.

- [56] J. Martins, Z. Mohamed, M. Tokhi, J. S. da Costa, and M. Botto, “Approaches for dynamic modelling of flexible manipulator systems,” *IEE Proc. Contr. Theory Appl.*, vol. 150, no. 4, pp. 401–411, 2003.
- [57] B. Subudhi and A. S. Morris, “Dynamic modelling, simulation and control of a manipulator with flexible links and joints,” *Robot. Auton. Syst.*, vol. 41, no. 4, pp. 257–270, 2002.
- [58] H. Sira-Ramírez, C. A. Núñez, and N. Visairo, “Robust sigma–delta generalised proportional integral observer based control of a ‘buck’ converter with uncertain loads,” *Int. J. Control*, vol. 83, no. 8, pp. 1631–1640, 2010.
- [59] J. Linares-Flores, J. Barahona-Avalos, H. Sira-Ramírez, and M. Contreras-Ordaz, “Robust passivity-based control of buck-boost-converter/DC-motor system: an active disturbance rejection approach,” *IEEE Trans. Ind. Applicat.*, vol. 48, no. 6, pp. 2362–2371, 2012.
- [60] H. Sira-Ramírez and M. Oliver-Salazar, “On the robust control of buck-converter DC-motor combinations,” *IEEE Trans. Power Electron.*, vol. 28, no. 8, pp. 3912–3922, Aug. 2013.
- [61] M. Ramírez-Neria, H. Sira-Ramírez, R. Garrido-Moctezuma, and A. Luviano-Juárez, “Linear active disturbance rejection control of underactuated systems: the case of the furuta pendulum,” *ISA Trans.*, vol. 53, no. 4, pp. 920 – 928, 2014.
- [62] H. Sira-Ramírez, F. González-Montañez, J. Cortés-Romero, and A. Luviano-Juárez, “A robust linear field-oriented voltage control for the induction motor: experimental results,” *IEEE Trans. Ind. Electron.*, vol. 60, no. 8, pp. 3025–3033, 2013.
- [63] A. Rodriguez-Angeles and J. Garcia-Antonio, “Active disturbance rejection control in steering by wire haptic systems,” *ISA Transactions*, vol. 53, no. 4, pp. 939 – 946, 2014.
- [64] G. Ramos, J. Cortés-Romero, and H. C.-E. Ram, “Spatial observer-based repetitive

- controller: an active disturbance rejection approach,” *Control Eng. Pract.*, vol. 42, no. 0, pp. 1 – 11, 2015.
- [65] R. Ortega and M. W. Spong, “Adaptive motion control of rigid robots: A tutorial,” *Automatica*, vol. 25, no. 6, pp. 877 – 888, 1989.
- [66] R. Ortega, J. A. L. Perez, P. J. Nicklasson, and H. Sira-Ramirez, *Passivity-based control of Euler-Lagrange systems: mechanical, electrical and electromechanical applications*. Springer Science & Business Media, 2013.
- [67] H. Berghuis and H. Nijmeijer, “A passivity approach to controller-observer design for robots,” *IEEE Trans. Robot. Autom.*, vol. 9, no. 6, pp. 740–754, 1993.
- [68] R. Bickel and M. Tomizuka, “Passivity-based versus disturbance observer based robot control: equivalence and stability,” *J. Dyn. Syst. T. Asme.*, vol. 121, no. 1, pp. 41–47, 1999.
- [69] M. V. Kothare and M. Morari, “Multiplier theory for stability analysis of anti-windup control systems,” *Automatica*, vol. 35, no. 5, pp. 917 – 928, 1999.
- [70] D. Lee and P. Li, “Passive bilateral control and tool dynamics rendering for nonlinear mechanical teleoperators,” *IEEE Trans. Robot.*, vol. 21, no. 5, pp. 936–951, 2005.
- [71] J.-H. Ryu, D.-S. Kwon, and B. Hannaford, “Stable teleoperation with time-domain passivity control,” *IEEE Trans. Robot. Autom.*, vol. 20, no. 2, pp. 365–373, 2004.
- [72] E. Nuño, L. Basañez, and R. Ortega, “Passivity-based control for bilateral teleoperation: A tutorial,” *Automatica*, vol. 47, no. 3, pp. 485–495, 2011.
- [73] A. Franchi, P. R. Giordano, C. Secchi, H. I. Son, and H. H. Bulthoff, “A passivity-based decentralized approach for the bilateral teleoperation of a group of uavs with switching topology,” in *Proc. of the 2011 IEEE Int. Conf. on Robotics and Automation (ICRA)*, Shanghai, China, May 2011, pp. 898–905.

- [74] A. Albu-Schäffer, C. Ott, and G. Hirzinger, “A unified passivity-based control framework for position, torque and impedance control of flexible joint robots,” *Int. J. Robot. Res.*, vol. 26, no. 1, pp. 23–39, 2007.
- [75] C. Ott, A. Albu-Schaffer, A. Kugi, S. Stamigioli, and G. Hirzinger, “A passivity based cartesian impedance controller for flexible joint robots-part I: Torque feedback and gravity compensation,” in *Proc. of the 2004 IEEE Int. Conf. on Robotics and Automation (ICRA)*, vol. 3, New Orleans, LA, Apr. 2004, pp. 2659–2665.
- [76] A. Albu-Schaffer, C. Ott, and G. Hirzinger, “A passivity based cartesian impedance controller for flexible joint robots-part II: Full state feedback, impedance design and experiments,” in *Proc. of the 2004 IEEE Int. Conf. on Robotics and Automation (ICRA)*, vol. 3, New Orleans, LA, Apr. 2004, pp. 2666–2672.
- [77] C. Ott, A. Albu-Schaffer, A. Kugi, and G. Hirzinger, “On the passivity-based impedance control of flexible joint robots,” *IEEE Trans. Robot.*, vol. 24, no. 2, pp. 416–429, 2008.
- [78] M. A. Arteaga-Pérez and A. Gutiérrez-Giles, “On the GPI approach with unknown inertia matrix in robot manipulators,” *Int. J. Control*, vol. 87, no. 4, pp. 844–860, 2014.
- [79] H. K. Khalil and J. Grizzle, *Nonlinear systems*. New York: Prentice hall New Jersey, 1996.
- [80] J.-J. E. Slotine and W. Li, “On the adaptive control of robot manipulators,” *Int. J. Robot. Res.*, vol. 6, no. 3, pp. 49–59, 1987.
- [81] R. Ortega, *Passivity-based control of Euler-Lagrange systems: mechanical, electrical and electromechanical applications*. London, U.K.: Springer, 1998.

Appendix A

Conditions on the Periodic Switching of Contact Radius

Since the switching of the contact radius is alternate, the switching periodicity is worth investigating. The wheel angular speed $\dot{\phi}_i$ can be written as:

$$\dot{\phi}_i = \begin{cases} \dot{\phi}_i^{in}, & \text{if } L_i = D_{in}, \quad i = 1, 2, 3. \\ \dot{\phi}_i^{out}, & \text{if } L_i = D_{out}, \quad i = 1, 2, 3. \end{cases}$$

We define t_1 and t_2 as the holding time for the inner wheel contact and outer wheel contact, respectively (see Figure 3.1). Then we have the following theorem based on the two switching conditions:

Theorem 1: For the given constants t_1, t_2 , the switching of the contact radius is periodic with period $T = t_1 + t_2$, if the wheel angular velocity $\dot{\phi}_i$ satisfies:

(a) For the switching condition (i),

$$\int_{t_0}^{t_0+t_1} \dot{\phi}_i^{in} dt = \pm \frac{\pi}{4}, \quad \text{if } L_i = D_{in}, \quad i = 1, 2, 3.$$

$$\int_{t_0+t_1}^{t_0+T} \dot{\phi}_i^{out} dt = \pm \frac{\pi}{4}, \quad \text{if } L_i = D_{out}, \quad i = 1, 2, 3.$$

(b) For the switching condition (ii),

$$\int_{t_0}^{t_0+t_1} \dot{\phi}_i^{in} dt = 0, \quad \text{if } L_i = D_{in}, \quad i = 1, 2, 3.$$

$$\int_{t_0+t_1}^{t_0+T} \dot{\phi}_i^{out} dt = 0, \quad \text{if } L_i = D_{out}, \quad i = 1, 2, 3.$$

Appendix B

Control Board Design

In our design, the central control board and motor control board are same. The motor control board with CAN communication module shown in Figure 2.3 was developed in our lab, which is depicted in Figure B.1.

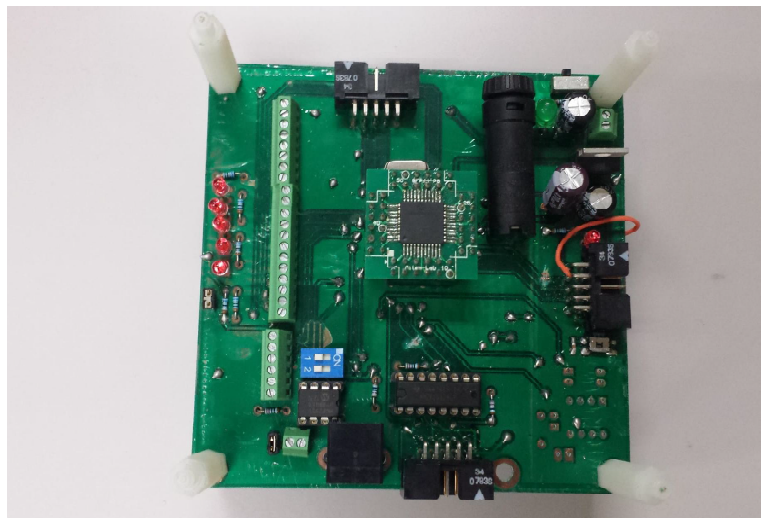


Figure B.1: Central control board developed in our lab.

Appendix C

Motor Driver Board Design

The three DC motor driver boards were designed and developed in our lab. Figure C.1 shows one developed motor driver board, which is rated for a maximum motor supply voltage of 55V with up to 3A continuous current output.

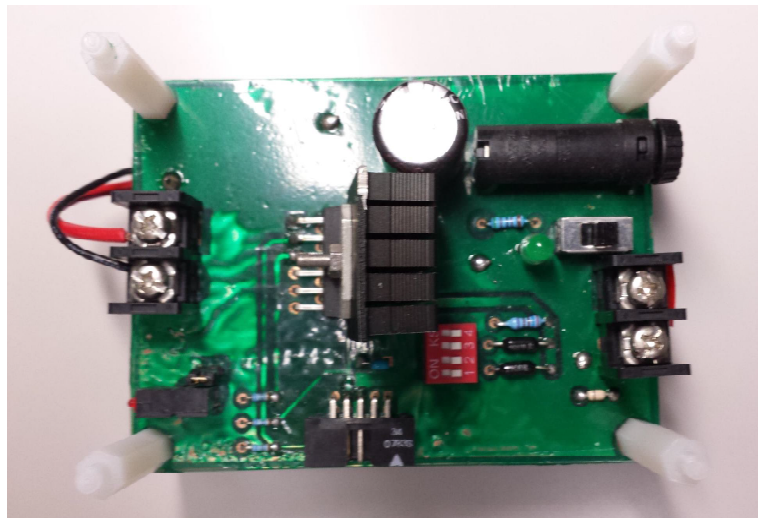


Figure C.1: Motor driver board developed in our lab.

Appendix D

Original Experimental Data

D.1 Original Data of Average Dynamic Model based RAC

D.1.1 Tracking Performance

Table D.1: Tracking performances: IAE of average dynamic model based RAC

Trajectory	Circle		Square		Lemniscate	
IAE	$IAE_{xy}(\text{m})$	$IAE_{\theta}(\text{rad})$	$IAE_{xy}(\text{m})$	$IAE_{\theta}(\text{rad})$	$IAE_{xy}(\text{m})$	$IAE_{\theta}(\text{rad})$
Experiment 1	0.9118	1.7184	0.7378	1.0814	0.7229	1.8505
Experiment 2	0.9488	2.1064	0.8420	1.1521	0.6104	1.0497
Experiment 3	1.0776	2.0922	0.8194	0.9882	0.6048	1.1804
Average	0.9794	1.9723	0.7997	1.0739	0.6460	1.3602

Table D.2: Robustness: IAE of average dynamic model based RAC

IAE	$IAE_{xy}^{WT}(\text{m})$	$IAE_{xy}^W(\text{m})$	$P_{xy}(\%)$	$IAE_{\theta}^{WT}(\text{rad})$	$IAE_{\theta}^W(\text{rad})$	$P_{\theta}(\%)$
Experiment 1	0.7137	1.1744	64.55	0.9901	1.4174	43.16
Experiment 2	0.8108	1.1543	42.37	1.0743	1.2117	12.8
Experiment 3	0.8340	1.1922	42.95	0.9036	1.3895	53.78
Average	0.7862	1.1736	49.29	0.9893	1.3395	35.40

Table D.3: Tracking performances: IAE of GPI observer based control

Trajectory	Circle		Square		Lemniscate	
IAE	$IAE_{xy}(\text{m})$	$IAE_{\theta}(\text{rad})$	$IAE_{xy}(\text{m})$	$IAE_{\theta}(\text{rad})$	$IAE_{xy}(\text{m})$	$IAE_{\theta}(\text{rad})$
Experiment 1	0.1095	0.1301	0.1796	0.2041	0.1153	0.1687
Experiment 2	0.0980	0.1540	0.1818	0.1897	0.1170	0.1467
Experiment 3	0.1028	0.1744	0.1855	0.1829	0.1123	0.1586
Average	0.1034	0.1528	0.1823	0.1922	0.1149	0.1580

Table D.4: Robustness: IAE of GPI observer based control

IAE	$IAE_{xy}^{WT}(\text{m})$	$IAE_{xy}^W(\text{m})$	$P_{xy}(\%)$	$IAE_{\theta}^{WT}(\text{rad})$	$IAE_{\theta}^W(\text{rad})$	$P_{\theta}(\%)$
Experiment 1	0.0695	0.0753	8.35	0.0909	0.1228	35.09
Experiment 2	0.0695	0.0736	5.90	0.0943	0.1096	16.22
Experiment 3	0.0699	0.0805	15.16	0.0862	0.1109	28.65
Average	0.0696	0.0765	9.81	0.0905	0.1144	26.49

D.1.2 Robustness

D.2 Original Data of GPI Observer based Control

D.2.1 Tracking Performance

D.2.2 Robustness

D.3 Original Data of Passivity based MFC

D.3.1 Tracking Performance

Table D.5: Tracking performances: IAE of passivity based MFC

Trajectory	Circle		Square		Lemniscate	
IAE	$IAE_{xy}(\text{m})$	$IAE_{\theta}(\text{rad})$	$IAE_{xy}(\text{m})$	$IAE_{\theta}(\text{rad})$	$IAE_{xy}(\text{m})$	$IAE_{\theta}(\text{rad})$
Experiment 1	0.3597	0.1979	0.5558	0.4088	0.4346	0.1716
Experiment 2	0.3722	0.2010	0.5552	0.4154	0.4242	0.1828
Experiment 3	0.3477	0.2056	0.5418	0.3955	0.4382	0.1764
Average	0.3599	0.2015	0.5509	0.4066	0.4323	0.1769

D.3.2 Robustness

Table D.6: Robustness: IAE of passivity based MFC

IAE	$IAE_{xy}^{WT}(\text{m})$	$IAE_{xy}^W(\text{m})$	$P_{xy}(\%)$	$IAE_{\theta}^{WT}(\text{rad})$	$IAE_{\theta}^W(\text{rad})$	$P_{\theta}(\%)$
Experiment 1	0.2289	0.2368	3.45	0.1027	0.1176	14.51
Experiment 2	0.2249	0.2440	8.49	0.0989	0.1250	26.39
Experiment 3	0.2371	0.2481	4.64	0.1007	0.1330	32.08
Average	0.2303	0.2430	5.50	0.1008	0.1252	24.25

Appendix E

Reference List

Figure 1.1 (a): <http://robocup.mi.fu-berlin.de/buch/shortomni.pdf>

Figure 1.1 (b):

<http://wertel.blogspot.com/2011/12/wheels-that-rotate-on-wheels.html>

Figure 1.1 (c): see Reference [3][4]

Figure 1.1 (d): see Reference [5]

Figure 1.2 (a): see Reference [6]

Figure 1.2 (b): see Reference [7]

Figure 1.2 (d): see Reference [9]

Figure 1.3 (a): http://www.kuka-robotics.com/en/products/mobility/mobile_platform_omnimize/start.htm

Figure 1.3 (b):

http://www.kuka-robotics.com/en/products/mobility/KMR_III

Figure 1.4 (a):

http://www.dinf.ne.jp/doc/english/Us_Eu/conf/csun_99/session0274.html

Figure 1.4 (b): <http://furo.org/en/works/wheelchair.html>

© 2012 IEEE. Reprinted, with permission, from Shugen Ma and Chao Ren, An Omnidirectional Mobile Robot: Concept and Analysis. Proceedings of the IEEE International Conference on Robotics and Biomimetics, 12/2012.

© 2013 IEEE. Reprinted, with permission, from Chao Ren and Shugen Ma, Dynamic Modeling and Analysis of an Omnidirectional Mobile Robot. Proceedings of the IEEE/RSJ International Conference on Intelligent Robots and Systems, 11/2013.

© 2014 IEEE. Reprinted, with permission, from Chao Ren and Shugen Ma, A New Dynamic Modeling Approach of an Omnidirectional Mobile Robot. Proceedings of the IEEE International Conference on Robotics and Automation, 06/2014.

Acknowledgment:

This thesis is derived, in part, from an article published by Taylor & Francis in Advanced Robotics on 2015 available online: *http : //dx.doi.org/10.1080/01691864.2014.978372*.

This thesis is derived, in part, from an article published by Elsevier in Mechatronics on 2015 available online: *http : //dx.doi.org/10.1016/j.mechatronics.2015.01.001*.

Published Papers During Doctoral Course

Journal Papers:

1. Chao Ren, Shugen Ma, Yi Sun and Changlong Ye, A continuous dynamic modeling approach for an omnidirectional mobile robot, *Advanced Robotics*, vol.29, no.4, pp. 253–271, 2015.
2. Chao Ren and Shugen Ma, Generalized proportional integral observer based control of an omnidirectional mobile robot, *Mechatronics*, vol.26, pp. 36–44, 2015.

International Conference Papers:

1. Shugen Ma and Chao Ren, An omnidirectional mobile robot: concept and analysis. In *Proc. of the 2012 IEEE Int. Conf. on Robotics and Biomimetics (ROBIO 2012)*, Guangzhou, China, Dec. 2012, pp. 920–925.
2. Chao Ren and Shugen Ma, Analysis and control of an omnidirectional mobile robot. In *Proc. of the 2013 44th Int. Symposium on Robotics (ISR 2013)*, Seoul, Korea, Oct. 2013, pp. 1-6. (Nominee for Best Paper)
3. Chao Ren and Shugen Ma, Dynamic modeling and analysis of an omnidirectional mobile robot. In *Proc. of the 2013 IEEE/RSJ Int. Conf. on Intelligent Robots and Systems (IROS 2013)*, Tokyo, Japan, Nov. 2013, pp. 4860-4865.

4. **Chao Ren** and Shugen Ma, Predictive kinematic control of an omnidirectional mobile robot. In *Proc. of the 2013 IEEE Int. Conf. on Robotics and Biomimetics (ROBIO 2013)*, Shenzhen, China, Dec. 2013, pp. 262-267. (**Best Paper Finalist**)
5. **Chao Ren** and Shugen Ma, A new dynamic modeling approach of an omnidirectional mobile robot. In *Proc. of the 2014 IEEE Int. Conf. on Robotics and Automation (ICRA 2014)*, Hongkong, China, Jun. 2014, pp. 2919-2924.
6. **Chao Ren** and Shugen Ma, Passivity-based model free control of an omnidirectional mobile robot. In *Proc. of the 2015 IEEE Int. Conf. on Mechatronics (ICM 2015)*, Nagoya, Japan, Mar. 2015, pp.262-267. (**Best Paper in Robotics Section**)